

STUDY OF TITAN'S METHANE CYCLE

by

Paulo Fernando Penteadó

A Dissertation Submitted to the Faculty of the
DEPARTMENT OF PLANETARY SCIENCES

In Partial Fulfillment of the Requirements
For the Degree of

DOCTOR OF PHILOSOPHY

In the Graduate College

THE UNIVERSITY OF ARIZONA

2009

UMI Number: 3356413

INFORMATION TO USERS

The quality of this reproduction is dependent upon the quality of the copy submitted. Broken or indistinct print, colored or poor quality illustrations and photographs, print bleed-through, substandard margins, and improper alignment can adversely affect reproduction.

In the unlikely event that the author did not send a complete manuscript and there are missing pages, these will be noted. Also, if unauthorized copyright material had to be removed, a note will indicate the deletion.

UMI[®]

UMI Microform 3356413
Copyright 2009 by ProQuest LLC
All rights reserved. This microform edition is protected against
unauthorized copying under Title 17, United States Code.

ProQuest LLC
789 East Eisenhower Parkway
P.O. Box 1346
Ann Arbor, MI 48106-1346

THE UNIVERSITY OF ARIZONA
GRADUATE COLLEGE

As members of the Final Examination Committee, we certify that we have read the dissertation prepared by Paulo Fernando Penteadó entitled Study of Titan's Methane Cycle and recommend that it be accepted as fulfilling the dissertation requirement for the Degree of Doctor of Philosophy.

Caitlin A. Griffith

Date: 12 September 2008

Roger Yelle

Date: 12 September 2008

Robert H. Brown

Date: 12 September 2008

Martin G. Tomasko

Date: 12 September 2008

E. Robert Kursinski

Date: 12 September 2008

Final approval and acceptance of this dissertation is contingent upon the candidate's submission of the final copies of the dissertation to the Graduate College.

I hereby certify that I have read this dissertation prepared under my direction and recommend that it be accepted as fulfilling the dissertation requirement.

Dissertation Director: Caitlin A. Griffith

Date: 12 September 2008

STATEMENT BY AUTHOR

This dissertation has been submitted in partial fulfillment of requirements for an advanced degree at The University of Arizona and is deposited in the University Library to be made available to borrowers under rules of the Library.

Brief quotations from this dissertation are allowable without special permission, provided that accurate acknowledgment of source is made. Requests for permission for extended quotation from or reproduction of this manuscript in whole or in part may be granted by the head of the major department or the Dean of the Graduate College when in his or her judgment the proposed use of the material is in the interests of scholarship. In all other instances, however, permission must be obtained from the author.

SIGNED: _____

Paulo Fernando Penteadó

ACKNOWLEDGEMENTS

Caitlin Griffith, for the advising.

Marty Tomasko, Steffi Engel, Chuck See and Lyn Doose, of the DISR team, for the collaboration, including the analysis of the VIMS data with the DISR model, which makes sections 6.4, 6.5 and 6.7, and parts of chapters 6 and 7.

The VIMS team, for the support and access to the observations, which constitutes most of the data used in this thesis.

Roger Yelle, Thomas Greathouse, Catherine de Bergh, John Rayner, Matthew Richter, Barry Lutz, Glenn Orton and Chris McKay, for the collaborations.

The Brazilian Government through CAPES and the NASA Planetary Astronomy Program, for the financial support.

TABLE OF CONTENTS

LIST OF FIGURES	7
LIST OF TABLES	9
ABSTRACT	10
CHAPTER 1 INTRODUCTION	11
1.1 General characteristics of Titan's atmosphere	11
1.2 Previous observations of atmospheric and surface methane	12
1.3 Previous observations of Titan's haze	18
1.4 Determinations of the methane abundance and spatial distribution	19
CHAPTER 2 RADIATIVE TRANSFER MODELS FOR TITAN'S SPECTRUM	22
2.1 Characteristics of Titan's spectrum	22
2.2 Discrete ordinates modeling of Titan's near infrared spectrum	23
2.3 Legendre polynomial fits to the scattering phase functions	27
CHAPTER 3 MEASUREMENTS OF GLOBAL METHANE ABUNDANCE IN TITAN FROM GROUND-BASED OBSERVATIONS	31
3.1 Observations	31
3.2 Analysis of Titan's infrared spectrum	33
3.3 Results	35
3.4 Discussion	36
CHAPTER 4 GROUND-BASED MEASUREMENTS OF THE METHANE DIS- TRIBUTION ON TITAN	39
4.1 Observations	39
4.2 Radiative transfer modeling of Titan's spectrum	41
4.3 Results	47
CHAPTER 5 CASSINI VIMS OBSERVATIONS OF TITAN	51
5.1 Instrument characteristics	51
5.2 Data visualization	52
5.3 Data selection	58

TABLE OF CONTENTS – *Continued*

CHAPTER 6	LATITUDINAL VARIATIONS IN TITAN’S METHANE AND HAZE FROM CASSINI VIMS OBSERVATIONS	63
6.1	Observations	63
6.2	Radiative transfer modeling of Titan’s spectrum	66
6.3	Approach	70
6.4	Fits with constant methane abundance	73
6.5	Methane and haze variation coupling	77
6.6	Analysis of 10,988 spectra	78
6.7	Heating rate	88
CHAPTER 7	CONCLUSIONS	92
APPENDIX A	AVAILABILITY AND USE OF TITAN_BROWSE	99
APPENDIX B	DOCUMENTATION OF TITAN_BROWSE	104
REFERENCES	113

LIST OF FIGURES

1.1	Thermal profile	12
1.2	Half flux altitudes	13
1.3	Methane mixing ratio profile	14
1.4	Midlatitude clouds	16
1.5	Cloud optical depth and altitude evolution	17
1.6	Ethane polar clouds	20
2.1	Titan's reflection spectrum	23
2.2	Phase function fits	28
3.1	8.6 μm emission spectrum	32
3.2	1.6 μm absorption spectrum	36
4.1	Geometry reference images	41
4.2	Wavelet determination of Titan's position	42
4.3	Spectra in the sample	43
4.4	CH ₃ D spectra	44
4.5	Indicator profiles	46
4.6	Indicator sensitivities	47
4.7	Contribution functions	48
4.8	Parameter profiles	50
5.1	Typical VIMS VIS and IR spectra of Titan	53
5.2	Typical VIMS Titan cube	54
5.3	VIMS image in multiple colormaps	56
5.4	Definition of colormaps	57
5.5	VIMS image mapped in HSV	58
5.6	titan_browse interface	61
6.1	Half flux altitudes	64
6.2	Location of spectra in dataset 1	65
6.3	Location of spectra in dataset 2	66
6.4	Location of spectra in dataset 3	67
6.5	Location of spectra in dataset 4	68
6.6	VIMS and model spectra of the Huygens site	69
6.7	Spectra of the 0.61 μm band	71
6.8	Variability of band ratios at 0.61 μm	72

LIST OF FIGURES – *Continued*

6.9	Latitudinal profiles of band ratios at $0.61 \mu\text{m}$	73
6.10	Single scattering albedo derived from VIMS spectra	74
6.11	Spectral variation with longitude at the Huygens latitude	76
6.12	Spectral variation with longitude at the equator	77
6.13	Selected spectra and model fits	78
6.14	Derived haze variation with no change in methane	79
6.15	VIMS spectrum fit with variable methane abundances	80
6.16	Families of haze and methane solutions	81
6.17	Latitudinal distribution of indicators	82
6.18	Indicator sensitivities to model parameters	83
6.19	$0.61 \mu\text{m}$ band depth contribution function	85
6.20	Latitudinal profiles for constant methane	86
6.21	Latitudinal profiles of haze parameters	87
6.22	Latitudinal profiles of methane parameters	88
6.23	Heating rates	90
7.1	Observed NSA profiles	94
7.2	Calculated NSA profiles	95
7.3	Minneart fits	96
7.4	NSA cause	97

LIST OF TABLES

3.1	Determinations of the $\text{CH}_3\text{D}/\text{CH}_4$ ratio	37
3.2	Determinations of the CH_4 total column abundance	38
6.1	Dataset geometries	65
6.2	Heating rates	91
A.1	Fields available for cube selection	102
A.2	Fields available for pixel selection	103

ABSTRACT

We developed radiative transfer models to reproduce Titan's visible and near infrared spectra, to determine the effects of the haze, and retrieve the methane abundances during Titan's current southern summer. With ground-based high resolution spectra of CH₃D absorption at 1.6 μm , we measured the global CH₃D abundance. Combined with observations of 8.6 μm emission of CH₃D and CH₄ that indicate their relative abundances, we thus determined the global CH₄ abundance. We expanded on these ground-based measurements, with improved radiative transfer models based on the Huygens DISR models, and spectra which resolve the spatial variation of the CH₃D lines. The profiles of CH₃D thus obtained revealed that the methane abundance on the lowest 10 km of Titan's atmosphere does not vary by more than 20% over 32°S-32°N. With the extensive coverage of Cassini VIMS observations at 0.35-1.6 μm , we determined the latitudinal variation of the methane at 20-50 km and of the haze. We find an ambiguity between the methane and haze abundances, so their gradients become coupled. At the lower limit of the methane gradient, the spectral variation observed can be reproduced with no methane change, and a haze density increase of 60% between 20°S and 10°S. The largest methane variation allowed by the data, derived assuming no haze variation with latitude, is a drop of 60% over latitudes 27°S to 19°N. Our analysis indicates that the latitudinal variations in Titan's visible to near-IR albedo, the North/South Asymmetry, result primarily from variations in the thickness of the haze above 80 km altitude. The range of methane latitudinal variations allowed between 27°S to 19°N indicates temperature variations of no more than 1.5 K at 20-30 km, altitudes where the Huygens profile is saturated.

CHAPTER 1

INTRODUCTION

1.1 General characteristics of Titan's atmosphere

Titan's dense atmosphere, which reaches 1.44 bar at the surface, consists primarily of molecular nitrogen (N_2 , $95.1^{+1.0}_{-1.5}\%$ of the bulk abundance) and methane (CH_4 , $4.9^{+1.5}_{-1.0}\%$ of the bulk abundance, Penteado et al. (2005); de Bergh et al. (1988); Coustenis et al. (1989, 2003); Orton (1992)), while the other components are at the 10^{-3} or lower abundance level (Courtin et al., 1995; Flasar, 1998; Flasar et al., 2005). The methane abundance in the atmosphere is controlled by its cycle between gaseous, liquid and ice, and between the atmosphere and surface sources. Transient methane clouds are frequently observed in the troposphere, and methane rain is possibly the source of the lakes and dry fluvial features observed at the surface. In the stratosphere, methane and nitrogen are destroyed by UV photolysis, and the byproducts recombine into larger hydrocarbons and nitriles. These grow into the haze particles, which display the scattering properties of fractal polymers comprising up to 3000 monomers of $0.05 \mu\text{m}$ or smaller (Tomasko et al., 2008c).

Titan's dense haze strongly affects the radiative heating and cooling of the atmosphere. In the stratosphere, the haze absorbs solar radiation in the ultraviolet to near infrared, which powers gaseous emission in the mid infrared, and continuum thermal emission in the far infrared (peak black body radiation for Titan's 82 K effective temperature is at $35 \mu\text{m}$). Figure 1.1 shows Titan's vertical temperature profile. The tropospheric temperature is set predominately by heating by sunlight absorption at the surface and near surface atmosphere, with convective and radiative cooling above it. In the stratosphere, the increasing haze optical depth and solar flux in the UV and visible causes higher heating from CH_4 and haze absorption towards higher altitudes, up to 300 km. At 300-600 km, the increasing efficiency of cooling by emission from ethane creates Titan's stratopause

and the mesosphere, with a temperature drop up to the mesopause, at 600 km, above which the increasing solar EUV flux causes increasing heating with altitude.

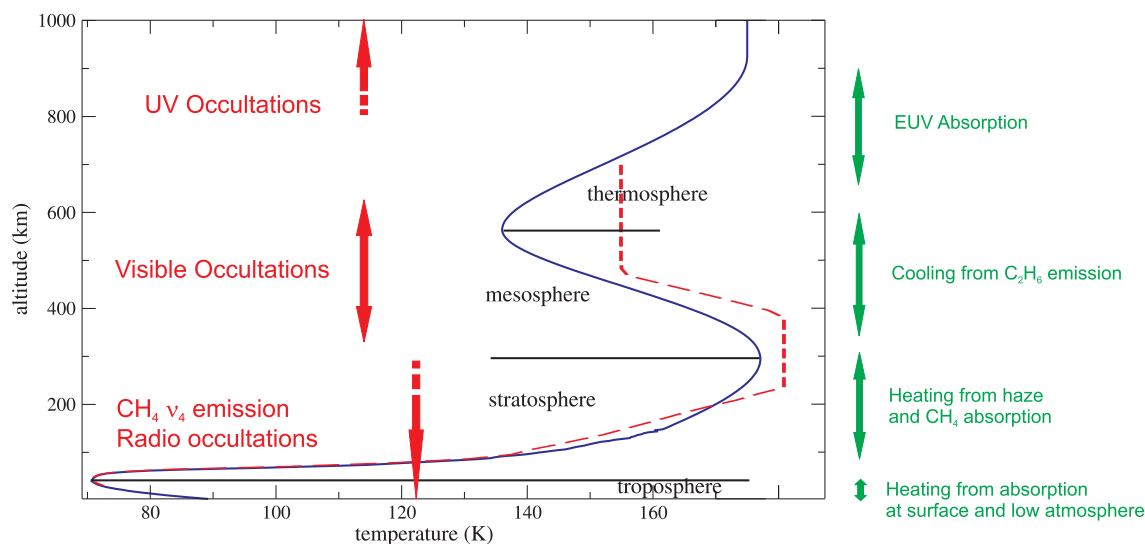


Figure 1.1 Temperature profiles over Titan's atmosphere. Blue line: model from Yelle et al. (1997). Red line: mesosphere derived from $8.6 \mu\text{m}$ CH_4 emission lines, from Griffith et al. (2005b). The black lines indicate the limits between the atmospheric regions. The red labels indicate remote observations that probe each altitude region. The green labels indicate the main processes responsible for heating and cooling of each region.

Figure 1.2 shows the altitudes where the direct solar and diffuse fluxes reach half their maximum value. It indicates that at wavelengths shorter than $0.6 \mu\text{m}$, the haze absorbs most light in the stratosphere, with decreasing haze optical depths towards longer wavelengths. The other main feature in figure 1.2 is the effect of the methane bands, which are optically thick enough (such as at $0.89 \mu\text{m}$) to prevent observations below the stratosphere, and at the IR windows (starting at $0.94 \mu\text{m}$), are thin enough to allow visibility to the surface (figure 5.2).

1.2 Previous observations of atmospheric and surface methane

Measurements of the global methane abundance and distribution of clouds and surface fluvial features, coupled with theoretical studies, partially constrain the methane cycle.

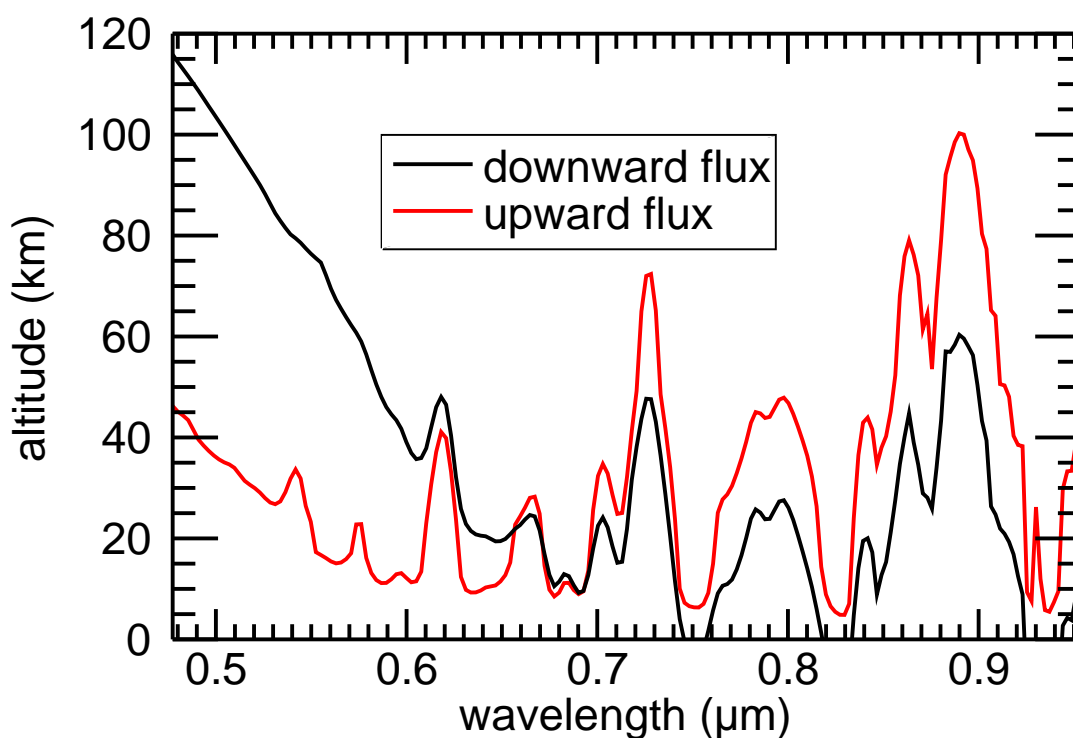


Figure 1.2 Altitudes where the model downward and upward (black and red, respectively) fluxes on Titan's atmosphere reach half their maximum value, in the region covered by the VIMS VIS channel. The downward flux is the sum of the direct solar flux and diffuse flux from scattered light. The altitudes for the upward flux are an approximation of the altitude region where the spectra are most sensitive to the methane and haze. The altitudes for the downward flux are an approximation to the altitude region where most absorption and scattering occurs.

The only measurement of the methane mixing ratio profile was taken at 10°S latitude, 192°W longitude, by the Huygens Gas Chromatograph and Mass Spectrometer (GCMS). It indicates 45% relative humidity (to liquid phase) at the surface, with a near constant mixing ratio above it, until saturation is reached (Niemann et al., 2005; Tokano et al., 2006). Previous ground-based measurements of the methane column density on Titan indicate global average values ranging from 0.4 to 5.5 km-am (de Bergh et al., 1988; Lellouch et al., 1989, 1992; Courtin et al., 1995; Lemmon et al., 2002; Penteado et al., 2005). This wide range of derived methane column abundances results partly from high

uncertainties in absorption coefficients. Titan's high methane column density saturates its strong bands, while the non-saturated lines are difficult to measure in the laboratory.

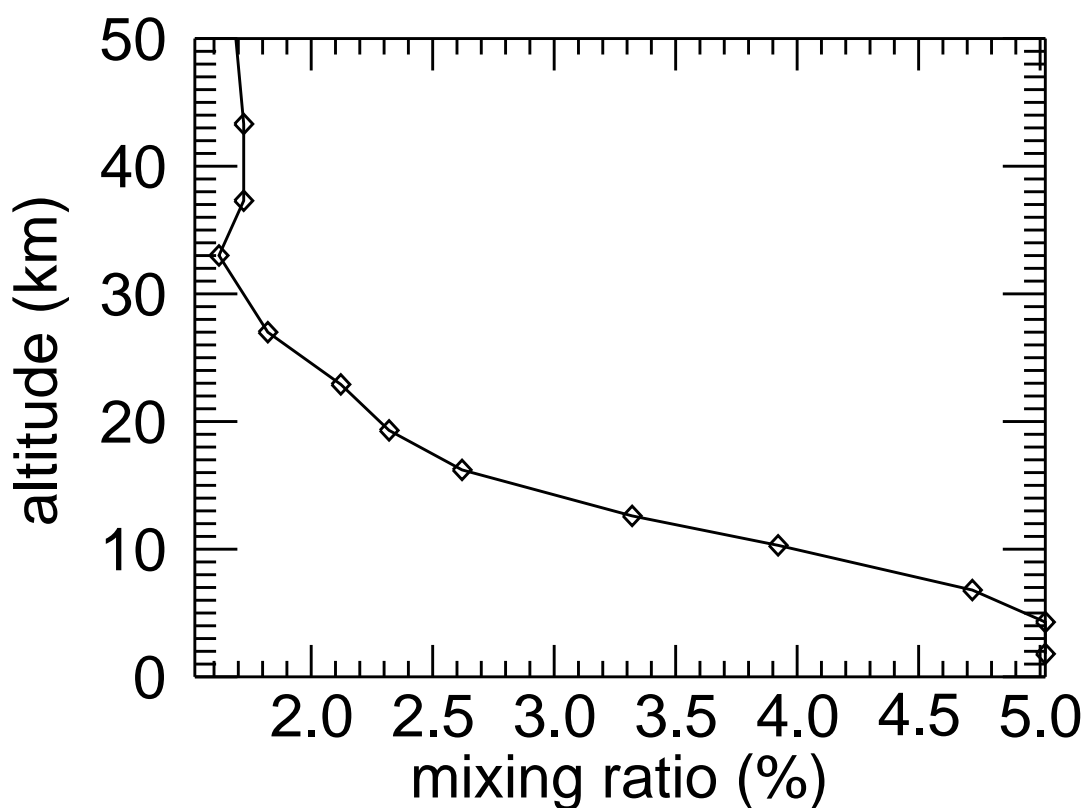


Figure 1.3 Methane mixing ratio in Titan's lower atmosphere, measured by the Huygens Gas Chromatograph and Mass Spectrometer (Niemann et al., 2005). This profile, taken at 10°S latitude, 192°W, is the standard used in the models discussed in chapters 4 and 6. The mixing ratio stays nearly constant from the surface to 8 km, which is the level where saturation is reached (Tokano et al., 2006).

Trafton (1975) estimated Titan's methane column abundance to be 1.6 km-am, using spectra of the $3\nu_3$ band of CH_4 . Fink and Larson (1979) compared spectra of Saturn, Titan, Uranus and Neptune at 0.8-2.5 μm and estimated from the 1.3 μm and 1.6 μm bands an abundance of 1 km-am. With the refractivity profiles from Voyager 1 and spectra of the 1.1 μm absorption band of CH_4 , Lellouch et al. (1992) found a column abundance of 4 km-am.

Lemmon et al. (2002) measured the CH₄ absorption bands in the region 0.6-1.1 μm , with the band curves of growth derived from laboratory data and spectra of Jupiter, Saturn, Titan, Uranus and Neptune by Karkoschka (1998). A maximum column abundance of 3.5 km-am was derived assuming no haze, while their haze model resulted in a column abundance of only 2.63 ± 0.17 km-am. Tables 3.1 and 3.2 summarize the current estimates of the isotopic ratio and total methane column density.

The methane can also be measured from the abundance of CH₃D combined with the CH₃D/CH₄ ratio. Considering Titan's near-IR spectrum, de Bergh et al. (1988) identified and analyzed two $3\nu_2$ features where the CH₃D contributions are most clearly distinct from those of CH₄. A CH₃D/CH₄ ratio of 66×10^{-5} best fit the data. Coustenis et al. (1989) analyzed Voyager 1 spectra of the 8.6 μm CH₃D band to measure an isotopic ratio of $60^{+56}_{-22} \times 10^{-5}$. Orton (1992) also recorded the 8.6 μm band with observations at the NASA Infrared Telescope Facility (IRTF) and found that the temperature uncertainties did not strongly influence the inferred isotopic ratio of CH₃D/CH₄ = $31 \pm 9 \times 10^{-5}$. The most recent observations of the ν_4 CH₃D band were made with the Infrared Space Observatory (Coustenis et al., 2003), and indicated an isotopic ratio of $35^{+13}_{-7.6} \times 10^{-5}$.

The only previous measure of methane variation was obtained from CH₄-N₂ collision-induced absorption in Voyager IRIS spectra at 17-50 μm . These spectra indicate a higher methane concentration at the equator, and more methane in the summer hemisphere (Samuelson et al., 1997). This latitudinal profile, however, has the methane supersaturated at the tropics, which was not observed by Huygens GCMS (Niemann et al., 2005). This disagreement suggests that the opacity structure of Titan's atmosphere at 17-50 μm is not fully understood.

An important part of Titan's methane cycle is the presence and distribution of methane clouds. Clouds were discovered from Titan's full disk spectra, recorded in 1995 (Griffith et al., 1998, 2000), and in 2000 first imaged over the south pole (Roe et al., 2002; Brown et al., 2002), where they have been most frequently observed in the past 12 years (Gendron et al., 2004; Gibbard et al., 2004; Hirtzig et al., 2005; Bouchez and Brown, 2005; Schaller et al., 2006a). Clouds have also appeared at 40°S latitude (Roe et al., 2005b; Porco et al., 2005; Griffith et al., 2005a; Brown et al., 2006; Schaller et al., 2006b). More recently,

cloud activity has decreased in the southern polar region, and clouds were observed at the latitudes of the northern polar lakes (Brown et al., 2009), which may represent the change from southern summer to fall (Schaller et al., 2006b).

Similar to Earth's convective clouds, Titan's methane clouds evolve in timescales of hours, (Griffith et al., 2000), and can reach the tropopause, where they are spread by zonal winds (Griffith et al., 2005a). Figure 1.4 shows near infrared images of typical midlatitude methane clouds, observed with Cassini VIMS. Figure 1.5 shows the optical depth and altitude evolution of these clouds, derived from the radiative transfer models that best reproduced the observed spectra.

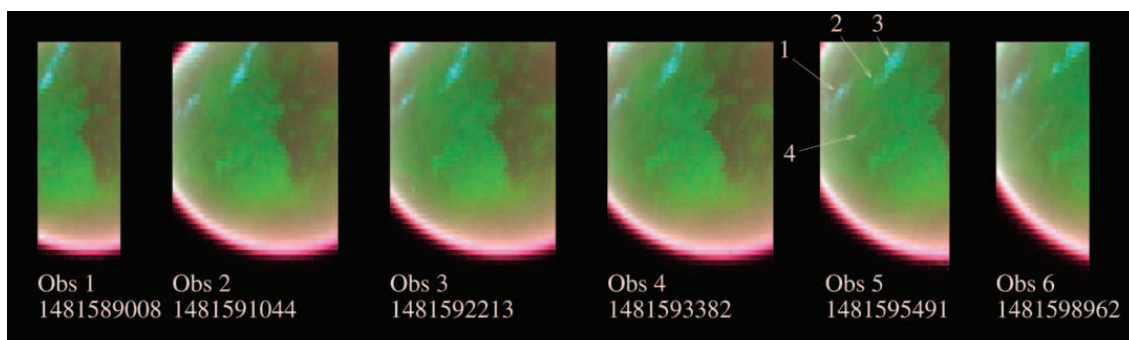


Figure 1.4 Midlatitude cloud evolution over a period of 167 min. The images are a composite of VIMS bands at $2.3 \mu\text{m}$ (red), $2.00 \mu\text{m}$ (green), and $2.13 \mu\text{m}$ (blue). The observations were taken during the TB flyby, on 13 December 2004. The clouds labeled 2-4 are near 40°S latitude, and cloud 1 is at 61°S . Figure from Griffith et al. (2005b).

Lakes and cryovolcanism have been suggested as one of the factors determining the nonuniformity of the cloud distribution. Since the atmospheric methane is destroyed by UV photolysis, a source is required within the past 20 million years to explain the current atmospheric inventory of methane (Yung et al., 1984). Models for Titan's interior structure suggest the methane may be replenished by outgassing from Titan's interior (Tobie et al., 2006). This hypothesis is consistent with the rarity of craters, though the current cryovolcanic candidates (Barnes et al., 2005; Sotin et al., 2005; Lopes et al., 2007) do not correlate with observed cloud locations.

Near infrared and radio observations from Cassini (Porco et al., 2005; Elachi et al.,

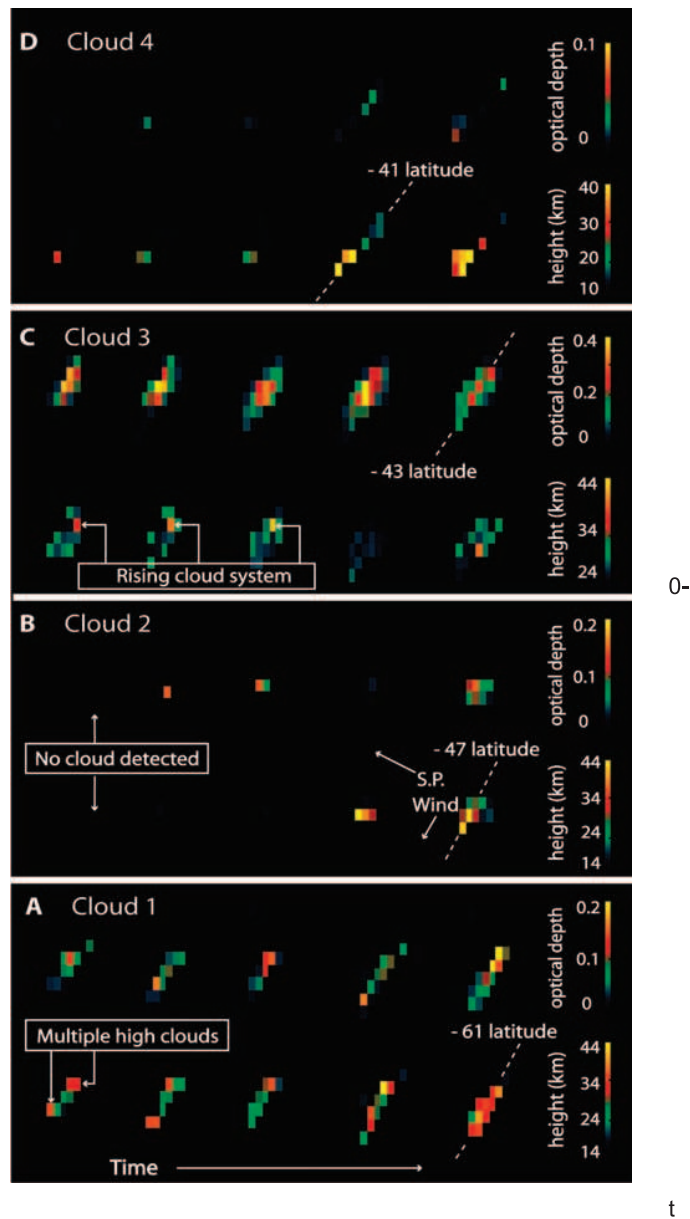


Figure 1.5 The optical depths and altitudes that resulted in the best fits to the spectra of the clouds shown in figure 1.4. Each panel shows, from left to right, the time evolution of the indicated cloud, in optical depth (top half) and altitude (bottom half). The interval between the frames is 20, 20, 35 and 58 min, for panels A, B, D (observations 2-6 figure 1.4), and 34, 20, 20 and 35 min for panel C (observations 1-5, figure 1.4). Figure from Griffith et al. (2005b).

2005; Soderblom et al., 2007) indicate lakes rather than global oceans (West et al., 2005). So far, the commonly found fluvial features, and the lakes larger than 10^4 km² identified on Cassini RADAR observations (Stofan et al., 2007) do not correlate with the preferential location of all methane clouds: The lake identified near the south pole, Ontario Lacus (Brown et al., 2008), might explain the south polar clouds, and recently small clouds have appeared at the latitudes of the northern polar lakes (Brown et al., 2009), but no surface features correlate with the prominent southern midlatitude clouds. Some observations point to a dry equatorial region, such as the rarity of clouds on Cassini observations (Griffith *et al.* 2009, submitted) the absence of liquid surfaces on the Huygens DISR (Descent Imager and Spectral Radiometer) images, and the distribution of channels observed by Cassini RADAR (Lorenz et al. (2008), though channels smaller than the RADAR resolution could be common in the tropics). However, Huygens observations also indicate abundant rainfall in the past: images show a variety of dark fluvial channels that end on dark basins (Tomasko et al., 2005; Keller et al., 2008), and signs of fluvial erosion at the landing site (Tomasko et al., 2005). Huygens GCMS (Gas Chromatograph and Mass Spectrometer) and SSP (Surface Science Package) measurements indicate the surface soil is moist with methane (Niemann et al., 2005; Zarnecki et al., 2005), though the relative humidity is only 45% (Niemann et al., 2005).

1.3 Previous observations of Titan's haze

Titan's haze acts as both a tracer and a radiative forcer of global circulation (Rannou et al., 2002): haze particles are transported from the summer to the winter hemisphere, and the haze absorbs 40% of the incident solar radiation. The haze, while uniform with longitude, displays latitudinal variations, with a pronounced north/south asymmetry, first detected from Pioneer 11 images (Tomasko and Smith, 1982), Voyager images (Sromovsky et al., 1981), and Voyager IRIS spectra at 200-1500 cm⁻¹. At 17 μ m, IRIS spectra indicate a 2.5 ± 0.3 increase in opacity between 70°N and 53°S latitudes (Coustenis and Bevard, 1995). Continuous monitoring since the Voyager observations in 1980 (after the northern spring equinox) has shown that the haze asymmetry is seasonal. The summer hemisphere

is darker at $0.9\ \mu\text{m}$ and brighter at $0.4\ \mu\text{m}$ (Lorenz et al., 2004; McKay et al., 2001; Lorenz et al., 2001, 1997), with haze optical depths at southern winter solstice increasing by 15% at $0.64\ \mu\text{m}$, from 80°S to 70°N (Lorenz et al., 1997; Tokano et al., 1999). However, prior efforts to determine latitudinal variations in haze were compromised by a lack of information on the vertical haze profile, now available at the Huygens site.

The only measurement of the vertical profile of haze optical properties at $0.4\text{-}1.6\ \mu\text{m}$ below 150 km altitude was derived at the Huygens site, with observations from the Descent Imager and Spectral Radiometer instrument (DISR, Tomasko et al. (2002)). With decreasing altitude, haze particles become brighter, and the slope of the wavelength variation in opacity decreases, suggesting increasing particle sizes due to condensation (Tomasko et al., 2008c).

The global circulation is also manifested in the ethane clouds observed most prominently at $2.8\ \mu\text{m}$ in Cassini VIMS images. These large diffuse clouds have been present constantly in the north polar region since their detection in 2004. Their altitudes, derived with radiative transfer models, are in the range 30-50 km. These clouds, shown in figure 1.6, are the result of ethane condensation from the decrease in temperature as stratospheric air subsides near the poles (Griffith et al., 2006).

1.4 Determinations of the methane abundance and spatial distribution

In order to understand how methane cycles on Titan's surface and atmosphere it is thus necessary to measure its abundance on the atmosphere, and its spatial and temporal variation. In this work, the methane abundance and its variation is measured from analysis of visible and near infrared spectra, both ground-based and from Cassini VIMS. Chapter 2 describes the radiative transfer models we developed to reproduce Titan's spectrum. With these models, we derived the global methane abundance (chapter 3) from ground-based (IRTF) observations of CH_3D absorption at $1.6\ \mu\text{m}$, with the $\text{CH}_3\text{D}/\text{CH}_4$ ratio from emission lines at $8.6\ \mu\text{m}$. As discussed in section 1.2, only the weakest CH_4 bands are not saturated on Titan's spectrum, and these bands have large uncertainties in the laboratory determinations of their absorption coefficients. Since CH_3D has a lower abundance,

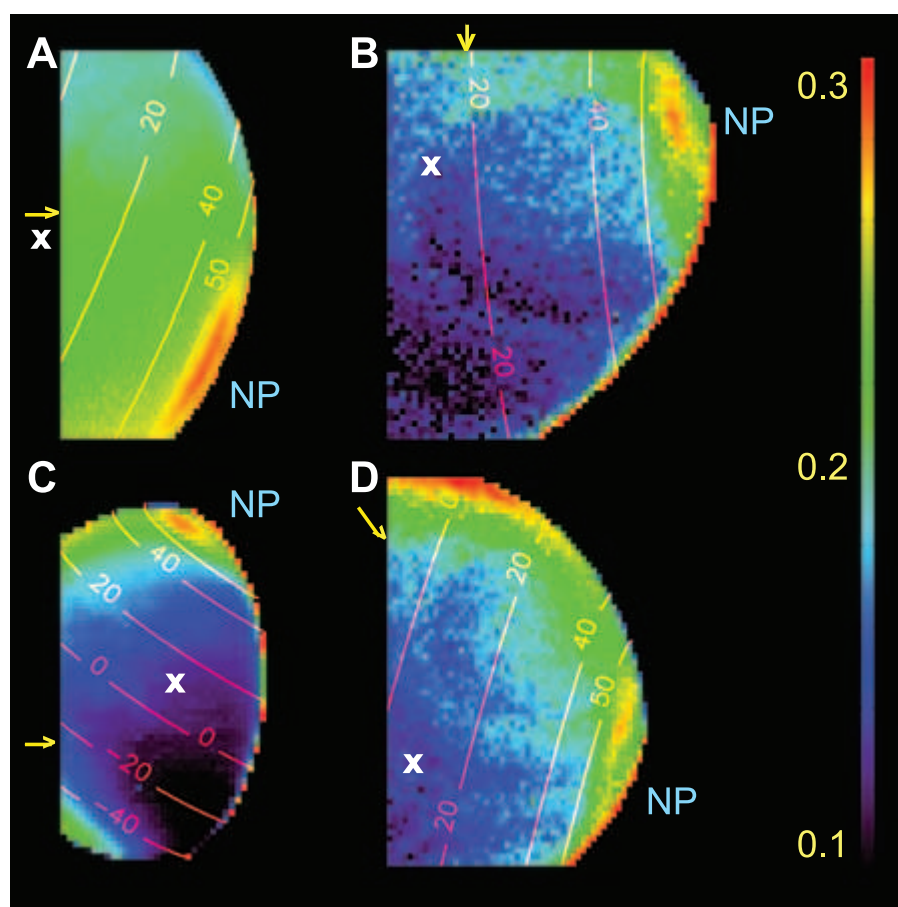


Figure 1.6 VIMS 2.8 μm image, scaled by the function $(\mu + \mu_0)/\mu_0^{0.3}$ (μ and μ_0 being the cosines of the incidence and emission angles, respectively), to decrease the effects of the strong illumination gradient. NP indicates the direction of the north pole, the contours indicate the latitudes, the yellow arrows indicate the illumination direction, and the white "x" indicate the subspacecraft location. In this colormap, the ethane clouds are the bright features near the north pole. The other bright regions at the limb pixels are an artifact caused by the high and variable emission angle. The observations were taken on passes TB (A, 13 December 2004), T6 (B and C, 22,21 August 2005), and T7 (D, 7 September 2005). Figure from Griffith et al. (2006).

the 1.6 μm CH_3D lines are not saturated on Titan's spectrum, and their available absorption coefficients have low uncertainties, thus it is possible to measure the CH_4 abundance through the CH_3D . Additionally, at 1.6 μm the haze effects on the derived methane abundances are not as strong as at visible or shorter near-IR wavelengths, and these lines

are weak enough to be sensitive to the methane down to the surface. Observations with enough spatial and spectral resolution to measure the spatial variation of the CH₃D bands are possible with the use of adaptive optics with the 10 m Keck telescope. We recorded and analyzed these observations, to derive a latitudinal profile of methane at altitudes 0-20 km (chapter 4).

Due to the strong effects of Titan's haze on the shorter wavelength methane bands, we needed to determine the spatial variation of the haze, and how it affects the derivations of methane abundance. We derived the latitudinal variation of Titan's haze and the methane at 20-50 km, as described in chapter 6, with Cassini VIMS observations, and comparing them to the Huygens DISR constraints for the methane and haze at 0.35-1.6 μm . The VIMS observations, described in chapter 5, record Titan's 0.35-5.12 μm spectrum, with extensive coverage at varied geometries and high spatial resolution.

CHAPTER 2

RADIATIVE TRANSFER MODELS FOR TITAN'S SPECTRUM

Titan's dense atmosphere strongly affects its visible to near infrared spectrum, mostly from scattering and absorption by haze particles, and absorption by methane. This chapter describes the radiative transfer models we developed to reproduce Titan's spectrum from 0.3 to 5 μm and near 8 μm , to derive the atmospheric properties from the observed spectral features.

2.1 Characteristics of Titan's spectrum

From 0.3 to 5 μm wavelengths, only the tropospheric and stratospheric regions (below 300 km altitude) of Titan's atmosphere significantly affect the reflection spectra. Over this region, the temperatures are low enough (less than 170 K) for continuum thermal emission to be negligible compared to scattered sunlight. Line emissions at these wavelengths are generally detectable only in night and limb observations, which were not used in this work. Therefore the most relevant information in these spectra is not the observed intensity (I), but the fraction of the incident solar flux (F) that is observed at a particular direction (I/F , also referred to as albedo, or flux reflectance). A typical spectrum of Titan at 0.4 to 5.1 μm is shown in figure 2.1. Its main features are high albedo regions at wavelengths shorter than 2 μm set by surface reflection and light scattered by the haze, and broad methane absorption bands, the strongest being optically thick enough to completely obscure Titan's lower atmosphere and surface. In addition to these main features, the spectra also show the effects of scattering by varied cloud types, and less prominent absorption by other molecules. Thus the visible and near infrared spectra provide constraints on Titan's haze, methane, clouds and surface features. In this work, Cassini VIMS and ground-based IRTF and Keck observations at those wavelengths were used to measure Titan's methane and haze, as detailed in chapters 3, 4 and 6.

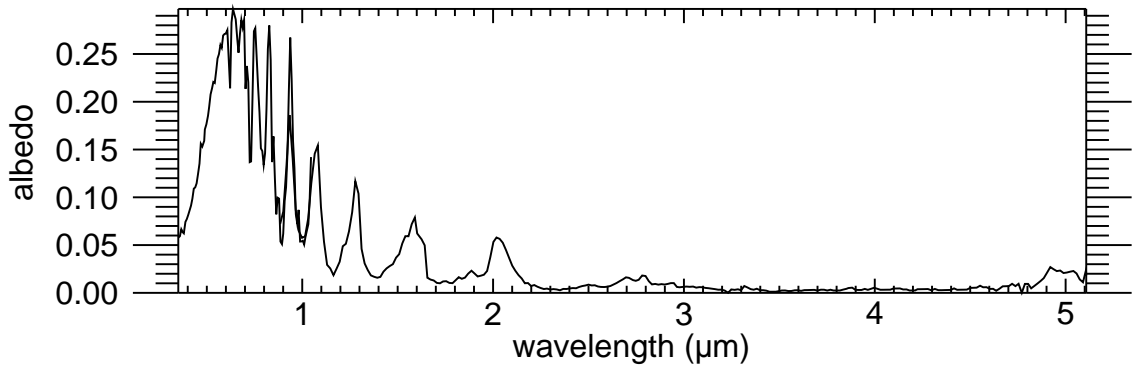


Figure 2.1 A typical reflection spectrum of Titan at low incidence and emission angles, taken by Cassini VIMS. The large absorptions bands are due to methane. This same spectrum is expanded in figure 5.1.

With ground-based observations from IRTF at $8.6 \mu\text{m}$, we determined Titan's $\text{CH}_3\text{D}/\text{CH}_4$ ratio, to measure the methane abundance, as detailed in chapters 3 and 4. Due to the difference in effective temperatures of the Sun (5800 K) and Titan (82 K), in the mid infrared, at wavelengths longer than $5 \mu\text{m}$, the main source of radiation changes from sunlight to emission from Titan's atmosphere. Thus Titan's spectrum changes from reflection to emission, and the most relevant observation is the recorded intensity, not albedo. The emissions come mostly from the stratosphere and higher altitudes (above 100 km). These altitudes are heated by haze absorption of sunlight in the ultraviolet to near infrared, and cooled by infrared emission. Thus these wavelengths become most useful to determine the temperature profile and gaseous composition of Titan's high atmosphere.

2.2 Discrete ordinates modeling of Titan's near infrared spectrum

To calculate the radiative flux leaving Titan's atmosphere, it is necessary to integrate at every wavelength the radiative transfer equation

$$\mu \frac{dI(\tau, \mu, \phi)}{d\tau} = -I(\tau, \mu, \phi) + S(\tau, \mu, \phi), \quad (2.1)$$

for the intensity I , as a function of cosine of emission angle (μ), emission azimuth (ϕ),

and optical depth (τ , used as the vertical dimension), subject to the boundary conditions of incident flux and reflection at the surface. The first term on the right is the total extinction (scattering and absorption), and the second is the source function S , which includes light scattered into the observer's direction, and emission,

$$S = Q(\tau, \mu, \phi) + \frac{\omega(\tau)}{4\pi} \int_0^{2\pi} d\phi' \int_{-1}^1 d\mu' P(\tau, \mu', \phi', \tau, \phi) I(\tau, \mu', \phi'). \quad (2.2)$$

Where Q is spontaneous emission. Stimulated emission can be accounted for more easily by changing the first term in (2.1), as a "negative absorption", since it is proportional to the incident radiation, but it is of no relevance here, since there is no significant stimulated emission in Titan's spectra used. Only at the $8.6 \mu\text{m}$ spectra there is significant emission, from CH_3D and CH_4 lines, which is well reproduced with the assumption of local thermodynamical equilibrium, and thus the source term is isotropic

$$Q(\tau) = (1 - \omega(\tau)) B(T(\tau)), \quad (2.3)$$

where ω is the single scattering albedo, B is the Planck function, and T is the temperature, as a function of τ (the vertical coordinate).

The second term on the right of (2.2) is the scattered light, where P is the scattering phase function. It is this term which makes the intensity at one point dependent on the intensity from the rest of the atmosphere, and creates the difficulties in solving the radiative transfer equation.

The most direct numerical solution is to simulate the flux of photons, either from the source or backtracing them from the observer. These methods, referred to as Monte Carlo or raytracing, compute the statistics of a large number of photons sent through the atmosphere, where the absorption and scattering optical depths determine the probability that a photon will be absorbed or scattered. When a scattering event occurs, the scattering phase function is the probability distribution function for the direction the photon is scattered to. These methods can yield accurate solutions, and account for any geometry (of particular interest to planetary atmospheres, spherical geometry), and non uniform surfaces (both in geometry and albedo), but tend to be too computationally intensive for studies where

large numbers of model spectra are necessary.

Analytical solutions for the radiative transfer equation with scattering exist only for simplified cases, such as where the medium is homogeneous, and the illumination is provided only by the unscattered light. In this case, most of the scattered radiation coming out of the medium was scattered only once, and it is thus referred as the single scattering approximation. This approximation cannot be used for Titan, since the haze and methane on Titan's atmosphere are too optically thick and variable over the visible and near infrared wavelengths up to $5 \mu\text{m}$.

For observations that intercept the surface, in geometries around normal incidence and emission, the curvature of the atmosphere can be neglected, thus allowing for plane-parallel models, in which the atmosphere is a collection of plane horizontal homogeneous layers. The conditions for validity of the single scattering approximation already suggest one algorithm for numerical solutions: divide the atmosphere in layers thin enough to be homogenous and involve only one scattering event, and use the analytical solution for each thin layer for the boundary conditions of the next. This approach, referred to as doubling and adding, allows for accurate solutions for layered media, and requires no assumptions regarding the form of the intensity field or scattering phase functions. The main limitation of this method is the potentially high number of layers in which the atmosphere has to be divided, to accommodate the assumptions of homogeneity and low scattering optical depth - from 0.9 to $0.4 \mu\text{m}$, Titan's optical depth increases from 3.5 to 15 (Tomasko et al., 2008c). These methods are considerably faster than Monte Carlo methods, but still too slow to calculate the $\sim 10^5$ model spectra necessary for our fit algorithms to reproduce Titan's spectrum (chapters 4 and 6).

Approximations regarding the form of the intensity field and the scattering phase functions further reduce the required computing power. A common choice for the spectra of planetary atmospheres is to quantize the intensity field by a small number of values. The integral of (2.1) is expanded in polynomials of I and P in μ and ϕ , truncated at a low number of elements. Two-stream models achieve this by approximating the intensity functions by two values at each optical depth, either as a constant for each hemisphere (up and down), or as a linear function of the cosine of emission angle (the latter also referred

to as Eddington approximation). The phase function in these models is usually quantized by only one value, its first moment, frequently referred to as the asymmetry factor. While two-stream models are generally the fastest algorithms, the use of only two values to characterize the intensity at each level results in low accuracies when the diffuse flux constitutes a large fraction of the illumination (which is the case at Titan's troposphere in most of the spectrum at less than $2 \mu\text{m}$), and at viewing geometries far from vertical incidence and emission. Thus in this work we use discrete ordinates algorithms, which are a generalization of the two-streams approximation, to resolve I and P in an arbitrary, larger number of terms. The order of the approximation (the number of streams) can then be chosen for each application to obtain sufficient accuracy at the lowest computational cost.

The discrete ordinates implementation used is DISORT, described in detail by Stamnes et al. (1988); Stamnes and Conklin (1984); Stamnes and Swanson (1981); Stamnes and Dale (1981); Thomas and Stamnes (1999). The phase function is approximated by a Legendre polynomial, its order given by the even number of streams N in the model, and the intensity function approximated by a Fourier series in azimuthal angle. The radiative transfer equation becomes, for each of the N Legendre orders, a system of N coupled linear differential equations in τ , one for each of the N emission angles. The atmosphere is separated into L layers where the scattering properties are constant, so that in each layer it becomes possible to integrate these equations in μ . This integration is done with a double Gaussian quadrature, chosen because it is symmetrical around $\mu=0.5$, and it concentrates the points at the two ends ($\mu=1$ and $\mu=0$), where most of the structure in typical phase functions occur (the forward and backward scattering peaks). These systems of equations have solutions that are linear combinations of exponentials, where the homogeneous part is set by scattering and absorption. The particular solutions are set by the isotropic thermal emission, which is solved by approximating it as a polynomial in τ .

At each layer, the neighboring layers provide the boundary conditions, except at the top and bottom of the whole atmosphere, where the boundary conditions are set by the incident illumination and surface reflection, respectively. The illumination used in our models is a simple, parallel flux, as the models are used for daytime observations. The

surface reflection is Lambertian, since there were no detailed constraints to the surface reflection properties, and the surface has a small effect at the wavelengths we used to measure the methane and haze.

DISORT solves for the solution coefficients by inverting a system of $N^2 \times L^2$ linear equations. Thus the order of the approximation (number of streams) that provides the best compromise between precision and running time can be chosen independently of the model implementation, according to the constraints of a particular dataset, as described in chapters 3, 4 and 6. Another advantage is that since the solution is analytic for the sets of coefficients of the intensity polynomials, the models can provide intensities at any observer direction. The number of streams used determines only the precision of the result, not the directions where the intensities are calculated.

2.3 Legendre polynomial fits to the scattering phase functions

An important limitation of the discrete ordinates approximation became evident with the use of detailed constraints on the haze scattering provided by the Huygens DISR team (chapters 4 and 6). The observed phase functions are strongly concentrated on forward scattering ($0-15^\circ$), with a peak that is hundreds of times higher than the structure at higher angles, as shown in figure 2.2. These functions are challenging to reproduce with Legendre polynomials, as required by DISORT. To properly reproduce the scattering properties of these phase functions:

- The polynomial must be smooth.
- The polynomial must be positive.
- The area in the forward scattering peaks of the original function and the polynomial must match. The detailed shape of the peak is not important, only the area contained within the first 15° .
- The polynomial must reproduce the structure of the original functions at high phase angles.

- The first coefficient of the fit (order 0) must be the largest in absolute value.

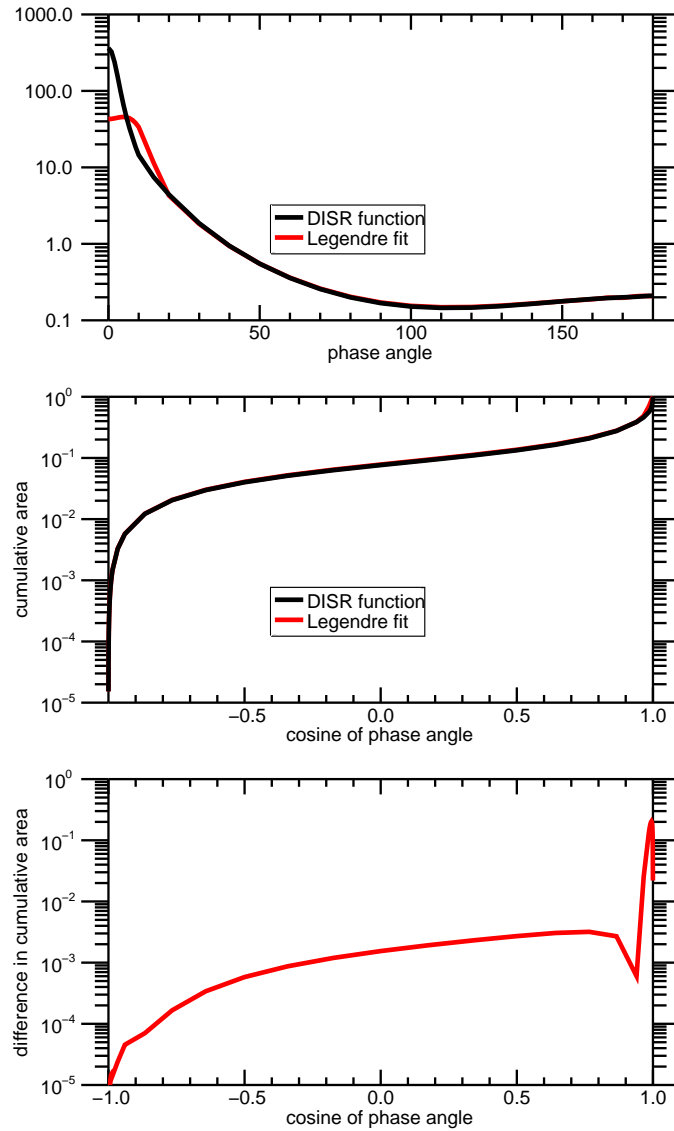


Figure 2.2 Top: Scattering phase function derived from DISR observations (black), and Legendre fit to it (red). Middle: cumulative areas of both functions in the top plots, showing that despite their different shapes at the forward peak, they both have similar areas. Bottom: difference between the two curves in the middle plot.

Direct least squares fits based on the differences between the polynomial and the phase function are not suitable, as these are biased toward low errors on the forward peak,

with strong and unphysical oscillations at angles larger than 20° . Without additional constraints, fits are easily found that have low errors, but are unacceptable because if sampled at higher resolution they show strong oscillations between the data points, or because they do not have the property of the first coefficient as the largest in absolute value.

Replacing the forward peak with a lower, broader peak of the same area, plus under-sampling the phase function at low angles and oversampling it at high angles also inhibits oscillations in the fits, but alone is not enough to obtain acceptable fits. Incorporating all the constraints directly into the fit makes the problem non linear. A linearized singular value decomposition inversion was developed to obtain solutions with all constraints, and produced phase functions with all the necessary properties at low orders (16-22), but since it is a linearized model to a non linear problem, it occasionally fails to converge into an acceptable solution, due to the large number of local minima in the parameter space. Thus we had to revert to another, linear fit. We first replace the forward peak with a Gaussian function such that its area is conserved, and its peak is lower, then use a singular value decomposition fit. The constraint of the absolute value is enforced iteratively, by taking each solution and changing the coefficients larger than the first, and setting those as constants, before doing the next fit for the remaining coefficients. This algorithm was able to produce acceptable solutions for all phase functions, though at the cost of higher orders. One measure of the distribution of scattering between the forward peak and the rest of the angles is the first moment of the phase function, the asymmetry factor, which indicates how anisotropic the scattering is. It can be used to parametrize scaling transformations, which treat the photons in the forward peak as unscattered, and with changes in the optical depths and single scattering albedos, provide easier (less anisotropic) phase functions for numerical solutions. We find that to reproduce the DISR phase functions the order of the fits has to be at least 32. At this order, the complements of the asymmetry factors (1-asymmetry factor) and the fits matched to within 1%, and the angular dependence of the spectra becomes similar to that produced by the DISR doubling and adding model (which does not use approximations on the form of the phase function). Thus we used 32 streams in the discrete ordinates models for the analyses of chapters 4 and 6. One representative

Legendre fit is shown in figure 2.2.

CHAPTER 3

MEASUREMENTS OF GLOBAL METHANE ABUNDANCE IN TITAN FROM
GROUND-BASED OBSERVATIONS

We measured the CH₄ column abundance in Titan's atmosphere through an analysis of Titan's monodeuterated methane (CH₃D) spectral features. CH₃D is several orders of magnitude less abundant in Titan's atmosphere than CH₄. Thus, unlike CH₄, the strong and well studied CH₃D 3ν₂ lines are not saturated and provide a sensitive measure of its column abundance.

3.1 Observations

Near infrared observations were recorded on 2001 November 13 at the NASA Infrared Telescope Facility (IRTF), using the Cryogenic Near-IR Facility Spectrograph - CSHELL (Greene et al., 1993). Spectra were obtained in five adjacent intervals and later combined in a spectrum covering the entire 1.542-1.560 μm region with a nominal resolving power of 20,000. For each interval, 12 5-minute exposures were taken of Titan and 12 30-second exposures of the solar analog G4V star HR1656 (HD32923), which was used to obtain a reflection spectrum. The flux was calibrated to match a reference spectrum recorded on 1999 September 23 at the United Kingdom Infrared Telescope (UKIRT) with the Cooled Grating Spectrometer (Griffith et al., 2000), which closely matches our observing geometry. This reference spectrum covers 1.45-2.1 μm, with a resolving power of ~ 330. Our final calibrated spectrum has an estimated maximum noise level of 0.5%.

On 2001 November 16 we recorded emission spectra of CH₄ and CH₃D with the Texas Echelon Cross-dispersed Echelle Spectrograph, TEXES, (Lacy et al., 2002) at the IRTF. The spectra have a resolving power of R=70,000, and extend from 1151.8 cm⁻¹ (8.6819 μm) to 1159.8 cm⁻¹ (8.6222 μm). The asteroid 4 Vesta was also observed, and after the pipeline reduction, the final spectrum of Titan was divided by that of Vesta to

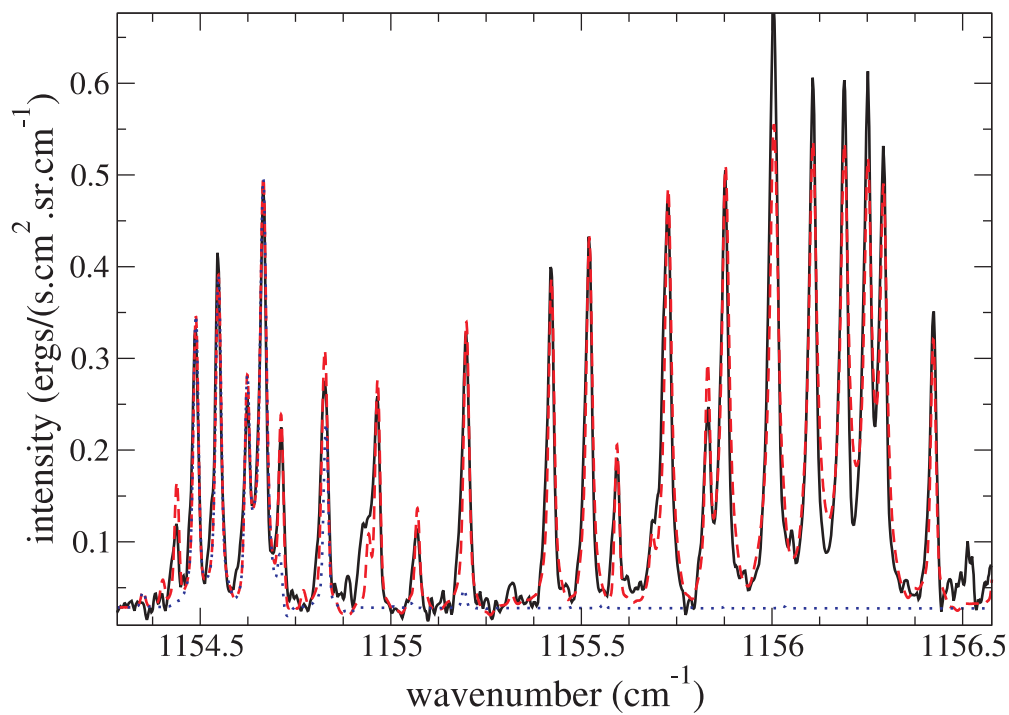


Figure 3.1 Titan's emission spectrum at the main CH_3D and CH_4 bands. Black full line: observed spectrum; Red dashed line: the best model fit; Blue dotted line: the best fit without the CH_3D lines.

eliminate the effects of telluric absorption and flux calibrated to match the spectrum of Orton (1992). The main lines in the resulting spectrum are shown in figure 3.1.

We recorded the observations shortly before Titan's northern winter solstice (on October 2002). The sub-Earth point was at latitude -25.6° . The sub-Earth longitude was $336\text{-}340^\circ$ for the $1.56\ \mu\text{m}$ observations and $44\text{-}45^\circ$ for the $8.6\ \mu\text{m}$ observations. All spectra sample Titan's entire disk.

3.2 Analysis of Titan's infrared spectrum

Titan's 1.6 μm spectrum contains both CH_4 and CH_3D lines. However, as a result of the uncertainties of the CH_4 absorption coefficients, a reliable CH_4 abundance cannot be directly derived. Therefore we analyzed the data to constrain only the CH_3D column abundance. Titan's 1.6 μm spectrum also depends on the surface reflection and haze scattering. These properties were determined by analyzing the UKIRT spectrum at 1.58 μm where the atmosphere is most transparent, to obtain the surface albedo, and at 1.63-1.73 μm , where haze most strongly affects the observed spectrum. The CH_4 lines in the 1.55 μm region were then fit by varying the CH_4 vertical profile. These absorption features provide a continuum for the CH_3D lines, which were then fit to determine the CH_3D abundance.

Spectra at 1.6 μm were calculated by approximating the radiative transfer equation with a discrete ordinates algorithm (Stamnes et al., 1988). We resolve the atmosphere into parallel layers of constant temperature, pressure and composition, and calculate the scattering and absorption of sunlight at each layer. The spectrum is determined at 21 different airmasses, from the center of the disk to the limb, and integrated to obtain a spectrum of the entire disk.

The model assumes the equatorial temperature-pressure profile determined from Voyager radio occultation and IRIS spectra (Lellouch et al., 1989). Titan's 1.58 μm spectrum indicates a surface albedo of 0.15 (Griffith et al., 2000). We approximated the scattering properties of the haze by assuming brightly scattering spherical particles with radii 0.3 μm . We first assumed that the haze density follows the pressure scale height (consistent with Titan's infrared spectrum of Samuelson 1983). Then the haze profile was further adjusted to match Titan's 1.63-1.73 μm albedo to the UKIRT spectrum, as discussed in Griffith et al. (2000). The fit for the 1.55 μm continuum for the CH_3D lines was obtained by varying only the CH_4 , by changing the saturation level between 100% and 200% saturation, and the surface humidity between 30% and the saturation level. The CH_3D was then varied to fit the CH_3D lines.

For CH_3D , at 1.55 μm , we calculated the line intensities and energy levels using the

coefficients from Boussin et al. (1998, 1999), and Lutz et al. (1983). To model the CH₄ lines in Titan and Uranus at 1.55 μm, de Bergh et al. (1986, 1988) used spectra of Saturn as the reference cold spectrum. Saturn's spectra were analyzed with a radiative transfer model, and once a best fit was found the remaining differences were attributed to errors in the populations of the energy levels. The values for the J quantum numbers were then changed to match the required populations. We modeled the 1.55 μm spectrum using both the unaltered laboratory line data and the corrected parameters of de Bergh et al. (1988), and found that without the corrected parameters, a good fit for the whole spectrum was not possible. We also verified that the lines of ¹²CH₄ and ¹³CH₄ are almost always overlapping, a result of their preserved symmetry. These two isotopes were treated as a single component, with a fixed ¹³CH₄/¹²CH₄ ratio of 1.116×10^{-2} . To avoid the uncertainties from errors in the identifications and strengths of CH₄ we disregarded spectral regions where CH₃D clearly overlaps with strong CH₄ features.

The ratio of CH₄ to CH₃D was determined from the analysis of stratospheric emission lines of CH₃D and CH₄ at 8.6 μm. We modeled the emission spectrum at 8.6 μm with a non-scattering LTE model of Titan's atmosphere, which calculates the radiative intensity of the atmosphere from the surface to 450 km altitude, divided into 152 parallel layers. These calculations occur at 8 different airmasses, added to obtain the radiance from the whole disk. The line optical depths are calculated assuming Voigt profiles and using the CH₄ and CH₃D line parameters of the HITRAN database (Rothman et al., 2003). For this region we also treated ¹³CH₄ and ¹²CH₄ as a single species with a constant ratio of 1.116×10^{-2} . We assume the nominal temperature profile of Yelle et al. (1997), and consider variations thereof to evaluate our uncertainties. Haze scattering was not included due to its low efficiency at these wavelengths, which are much larger than the typical particle size. To account for the continuum observed in the data we included a haze layer of constant optical depth in the lower stratosphere. The optical depth required depends on the assumed temperature profile, and thus was adjusted for each temperature profile considered. The uncertainties resulting from this haze layer are incorporated into the temperature induced uncertainties. We also ran tests using non-LTE source functions (R.V. Yelle 2005, private communication) in atmospheric models extended up to 1300

km altitude, and found that the maximum difference between intensities in the standard model and the non-LTE model is 2.6%, much smaller than the differences between the fits and the data.

3.3 Results

In figure 3.2, we show the separate effects of CH₄ and CH₃D for the four best defined features in Titan's spectrum, among which are the two features studied by de Bergh et al. (1988) at 1.550 and 1.556 μm . Four additional spectral regions at 1.5457 μm , 1.5468 μm , 1.5471 μm , and 1.5586 μm also display the effects of CH₃D, yet these are strongly contaminated by the CH₄ bands, and thus are considered unreliable. Two other features, at 1.5517 μm and 1.5591 μm , also show CH₄ contributions, though not as strong. The best defined four spectral regions (1.5487 μm , 1.5500 μm , 1.5512 μm and 1.5555 μm , shown in figure 3.2) result in an abundance of $2.0 - 2.2 \times 10^{-3}$ km-am. The uncertainties are caused mainly by the CH₄ absorption, dominating those from the haze scattering and surface albedo.

Emission lines at 8.6 μm are highly sensitive to the atmospheric temperature, therefore we chose lines that are formed at similar altitudes in Titan's stratosphere. We found that the observed weak and strong lines could not be well fit simultaneously with a single temperature profile, suggesting that the spectrum manifests spatial variations in Titan's thermal profile across the moon's disk. We find that variations in the temperature by ± 5 K introduce an error of 10% in the derived ratio. Figure 3.1 shows the reduced Titan spectrum at 1155 cm^{-1} (8.6 μm), along with the best fit model and a model that excludes CH₃D lines. A total of 36 strong, well-defined individual lines were identified, with 10 due to CH₄ and 26 to CH₃D.

We find the best fit for a haze altitude of 120 km and optical depth 0.05, though our observations do not strongly constrain simultaneously the haze altitude and optical depth. Our observations indicate a CH₃D/CH₄ ratio of $50 \pm 5 \times 10^{-5}$ assuming our nominal temperature profile. The errors correspond to uncertainties of ± 5 K. Additional uncertainties arising from the 1- σ noise level and considering the fits to different line strengths provide

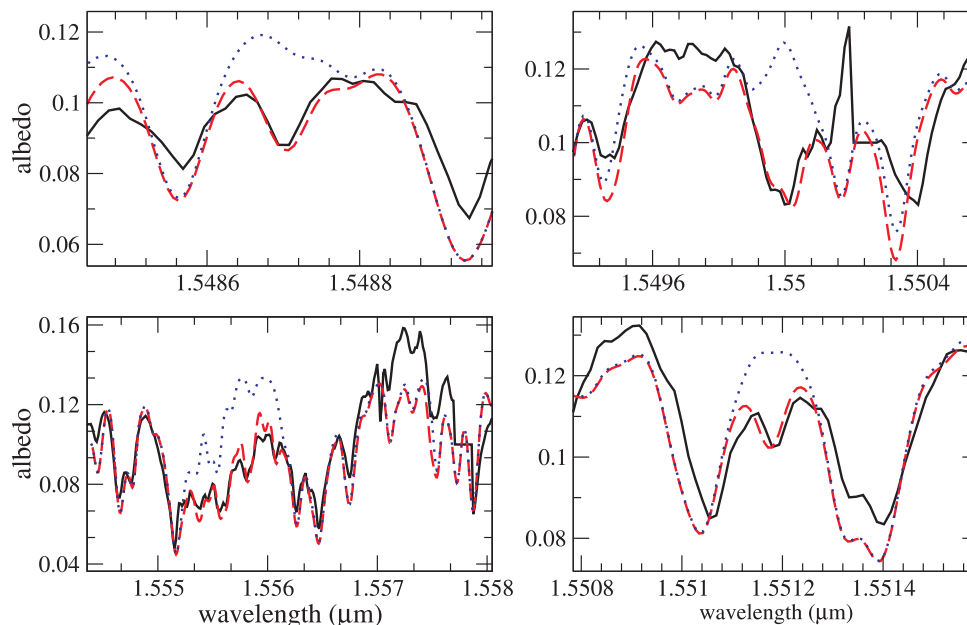


Figure 3.2 The four features that best reveal the absorption from CH_3D distinctively from CH_4 . Black full lines: observed spectrum; Red dashed lines: best fit; Blue dotted lines: fit without CH_3D absorption.

an additional uncertainty, with a resulting range of $50 \pm 10 \times 10^{-5}$.

3.4 Discussion

We derive an integrated CH_3D column abundance of $2.1 \pm 0.1 \times 10^{-3}$ km-am. This value agrees with the prior measurement of $1.4_{-0.7}^{+1.4} \times 10^{-3}$ km-am (de Bergh et al., 1988) from lower resolution spectra. Our derived $\text{CH}_3\text{D}/\text{CH}_4$ ratio of $50 \pm 10 \times 10^{-5}$ agrees with prior measurements by de Bergh et al. (1988), Coustenis et al. (1989), Coustenis et al. (2003), and Orton (1992), while differing significantly from the early near-infrared results (Gillett, 1975; Kim and Caldwell, 1982) (table 3.1).

Fouchet and Lellouch (2000) found that fractionation by methane condensation in Titan's atmosphere does not cause a detectable $\text{CH}_3\text{D}/\text{CH}_4$ variation. Thus the strato-

Table 3.1. Determinations of the CH₃D/CH₄ ratio

Wavelength	Instrument	Resolution	CH ₃ D/CH ₄	Ref.
8.6 μm	KPNO 2.1 m and 4 m	50	1.1×10^{-5}	1
8.6 μm	KPNO 2.1 and 4 m, IRTF, Voyager IRIS	50, 66, 250	170×10^{-5}	2
8.6 μm	Voyager IRIS	250	$60^{+56}_{-22} \times 10^{-5}$	3
8.6 μm	IRTF IRSHELL	10000	$31 \pm 9 \times 10^{-5}$	4
8.6 μm	ISO SWS	1900	$35^{+13}_{-7.6} \times 10^{-5}$	5
1.6 μm	4 m KPNO FTS	5400	$66^{+60}_{-30} \times 10^{-5}$	6
8.6 μm	IRTF TEXES	70000	$50 \pm 10 \times 10^{-5}$	7

References. — (1) Gillett 1975; (2) Kim and Caldwell 1982; (3) Coustenis et al. 1989; (4) Orton 1992; (5) Coustenis et al. 2003; (6) de Bergh et al. 1988; (7) this work.

spheric isotopic ratio derived here combined with the CH₃D column abundance indicates a total CH₄ column abundance of $4.2^{+1.3}_{-0.9}$ km-am, $4.9^{+1.5}_{-1.0}\%$ of the total atmospheric column abundance. An atmosphere with 100% saturation in the troposphere and constant mixing ratio above the tropopause has a column abundance of $4^{+1.4}_{-0.9}$ km-am (considering tropospheric temperature uncertainties as determined by Lellouch et al. 1989). We find a best fit with a surface CH₃D mixing ratio of $3.0 - 3.8 \times 10^{-5}$, which corresponds to a methane mixing ratio of 5.0-9.5% (47-90% relative humidity with the nominal surface temperature, or 37-109% with the surface temperature range of 92.5-95.7 K). It should be noted that the CH₃D absorption analyzed here is most indicative of the total column abundance, and does not constrain well its vertical distribution.

Our results of $4.2^{+1.3}_{-0.9}$ km-am are consistent with the maximum estimated by Lemmon et al. (2002) (3.5 km-am), but do not agree with their estimate of 2.63 ± 0.17 km-am. Perhaps this incongruity results from the greater transparency of the atmosphere in the wavelength region that we analyzed, along with the availability of line parameters for CH₃D and a more detailed model of the multiple scattering. Our results do not exclude a saturated atmosphere which never exceeds saturation by more than a few percent, as well

Table 3.2. Determinations of the CH₄ total column abundance

Data	Instrument	Col. density (km-am)	Ref.
CH ₄ abs. at 0.5-1.2 μm	2.7 m McDonald telescope	1.6	1
CH ₄ abs. at 0.8-2.5 μm	4 m KPNO	1	2
CH ₃ D abs. at 1.6 μm	4 m KPNO FTS	2.2	3
refractivity and CH ₄ abs. at 7.7 μm	Voyager RSS and IRIS	0.4-3.0, < 6.9	4
CH ₄ abs. at 1.1 μm	IRTF (CGAS) and CFH (FTS)	4 \pm 1	5
refractivity and abs. at 16-50 μm	Voyager RSS and IRIS	2.3-4.0	6
CH ₄ abs. at 0.3-1.1 μm	HST STIS	2.63 \pm 0.17, < 3.5	7
CH ₃ D abs. at 1.6 μm and CH ₃ D/CH ₄ emiss. at 8.6 μm	IRTF (CSHELL and TEXES)	4.2 ^{+1.3} _{-0.9}	8

References. — (1) Trafton 1975; (2) Fink and Larson 1979; (3) de Bergh et al. 1988; (4) Lellouch et al. 1989; (5) Lellouch et al. 1992; (6) Courtin et al. 1995; (7) Lemmon et al. 2002; (8) this work.

as an atmosphere which achieves high levels of supersaturation in the middle troposphere with subsaturation near Titan's surface, as suggested by the Voyager IRIS data (Courtin et al., 1995). It should be noted that some of the differences in the methane column abundance might be the result of seasonal variations on Titan, combined with the different latitude ranges sampled in each study.

CHAPTER 4

GROUND-BASED MEASUREMENTS OF THE METHANE DISTRIBUTION ON
TITAN

Using échelle spectra taken with NIRSPEC (Near Infrared Spectrometer) and adaptive optics on the Keck II telescope, we obtained spatially resolved spectra of the $3\nu_2$ band of monodeuterated methane (CH_3D) at $1.56 \mu\text{m}$ at a resolving power of 27000. Thus it becomes possible to use the CH_3D lines as discussed in chapter 3, to measure the methane abundance in Titan's troposphere at different latitudes. The analysis of these observations also improves on those of chapter 3 by the use of the constraints to the methane abundance and haze properties measured at the Huygens site (Niemann et al., 2005; Tomasko et al., 2008c,a), which were not previously available.

4.1 Observations

Observations were recorded on December 18 2006 over a 2.5 h period centered at 15:05 UTC, with the Near Infrared Spectrometer (NIRSPEC, McLean et al. (1995)) on the Keck II telescope. The spectra, taken in échelle mode, cover the $1.46\text{-}1.64 \mu\text{m}$ region at resolution $R \sim 27000$, sampled on 16 overlapping sections of 1024 pixels each. With the use of adaptive optics, the spatial resolution along the slit was $0.04''$, sampled with $0.013''$ pixels, which were binned in groups of 3 to attain 20 spatial resolution elements across Titan's disk. Figure 4.1 shows a typical slit camera image, recorded with the NIRSPEC-5 filter (covering $1.46\text{-}1.64 \mu\text{m}$), to indicate the location of the observations. The observing night was near Saturn's opposition, with a phase angle of 5.3° , and sub-observer point at 12.12°S , 196°E . At each grating setting, two spectra were obtained, with Titan on different positions along the slit, to subtract the sky contribution between the two nods. The initial flux calibration involved dividing Titan's spectra by those of the nearby solar analogue G5 star, HD 85258, of H magnitude 5.758. Titan's apparent full disk H magnitude

was 7.9, but that of the portion falling on each pixel was only 16.3.

We determine the position of the slit on Titan's disk from the slit camera images, as the required precision is higher than the uncertainty in the telescope's pointing information. Titan's disk is an extended source, with brightness variations smaller than the contrast between the disk and background. Thus the surface of the disk has a relatively flat profile over an extended area, such that the disk center cannot be found by simply fitting a sharply peaked function as the instrument's point spread function. The slit camera images were filtered to remove noise and decrease the variations over Titan's disk. Wavelet transforms of the images with a radially symmetric kernel of the dimension of Titan's disk result in a function that is sharply peaked on the disk center, because here Titan's disk coincides with the positive part of the kernel. A least squares fit of a Gaussian surface to the wavelet transform then provides the coordinates for the center of the disk, which were averaged among all the slit camera images taken during each spectrum. The resulting coordinates for Titan's center have an uncertainty smaller than 2 sample pixels of size 0.013", and are shown in figure 4.2.

Following Penteado et al. (2005), we analyzed lines from the $3\nu_2$ band of CH_3D that have well constrained absorption coefficients from laboratory measurements. The CH_3D lines are not saturated in Titan's atmosphere, as are the well measured CH_4 lines, and instead provide a sensitive measure of the abundance in the lowest 10 km of Titan's atmosphere. We chose a constant $\text{CH}_3\text{D}/\text{CH}_4$ ratio of $(50 \pm 10) \times 10^{-5}$, previously derived from unsaturated emission lines of CH_3D and CH_4 at $8.6 \mu\text{m}$ (Penteado et al., 2005), which is consistent with previous studies (de Bergh et al., 1988; Orton, 1992; Coustenis et al., 2003). However, as we derive relative variations in methane as a function of latitude, this choice does not affect our results. Figure 4.3 displays the measured and calculated spectra. The effects of high incidence and emission angles render the interpretation unreliable at the 4 points nearest to the limb, that is, at latitudes 59°S , 51°S , 45°S and 32°N . The methane abundance, as indicated by the weak CH_3D lines, can be inferred by comparing the observed and modeled spectra for several values of the surface relative humidity (figure 4.4); only at $1.5552\text{-}1.5562 \mu\text{m}$ is the CH_3D absorption comparable to that of CH_4 .

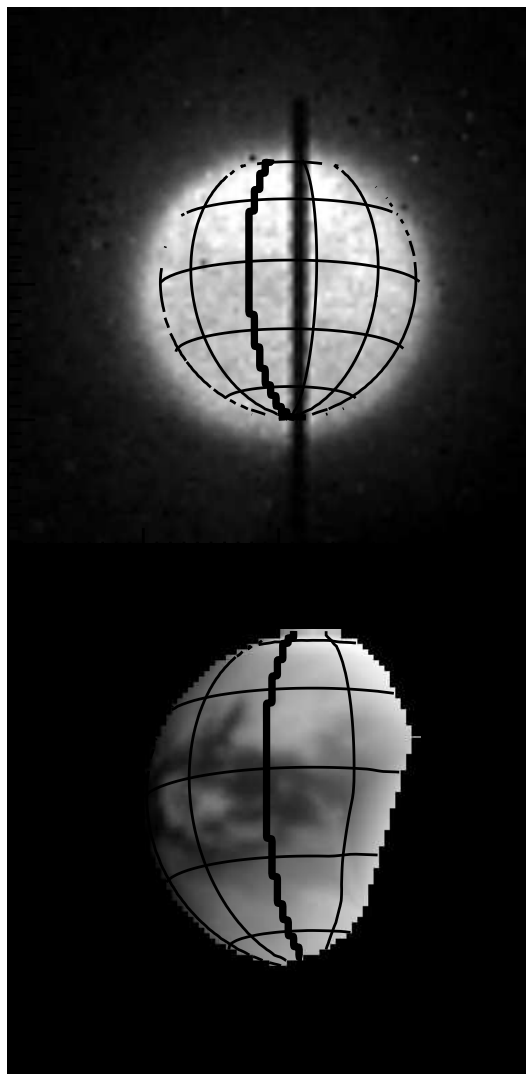


Figure 4.1 Geometry reference images. Top: Average slit camera image at 1.46-1.64 μm . The lines are latitude and longitude contours, spaced at 30° , the thicker line is 180° longitude. Bottom: A VIMS 1.56 μm image, projected to the same geometry and similar pixel scale, indicating the location of the observations. The difference in contrast is mostly due to the broader wavelength range of the NIRSPEC image, which includes wavelengths of high methane opacity around the 1.6 μm window.

4.2 Radiative transfer modeling of Titan's spectrum

To reproduce Titan's spectrum, we developed a radiative transfer model that incorporates the haze parameters and latitudinal variations derived from the Huygens DISR observa-

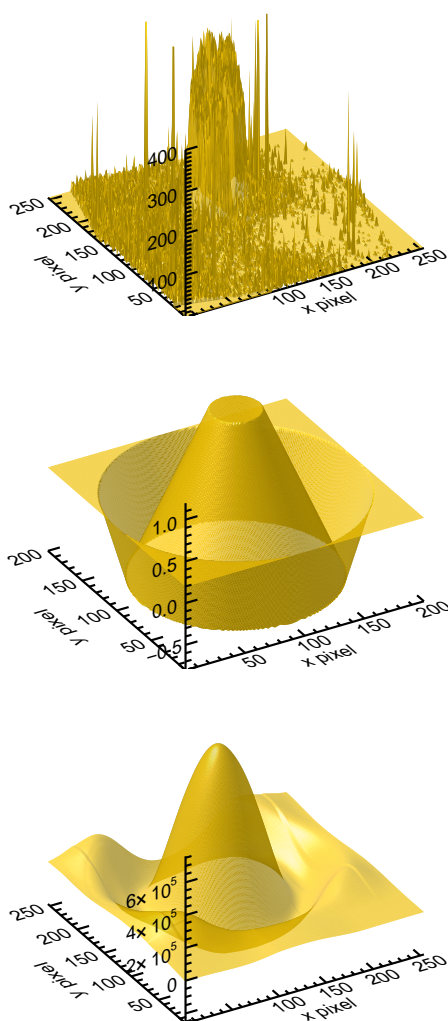


Figure 4.2 Wavelet determination of Titan's position, for one of the SCAM images taken during the spectra. Top: original SCAM image, showing Titan's disk has a broad and irregular profile. Middle: convolution kernel used, made to match Titan's size. Bottom: Convolution result, showing a sharp peak for the kernel position that best matches Titan's disk center.

tions (Tomasko et al., 2008c) and the analysis of Cassini VIMS observations at 0.4-1.6 μm (chapter 6 and Penteado *et al.* 2009, submitted). The model approximates the radiative transfer solution using a discrete ordinates algorithm (DISORT, Stamnes et al. (1988)) with 32 streams. The atmosphere was divided into 51 vertical homogeneous layers. We

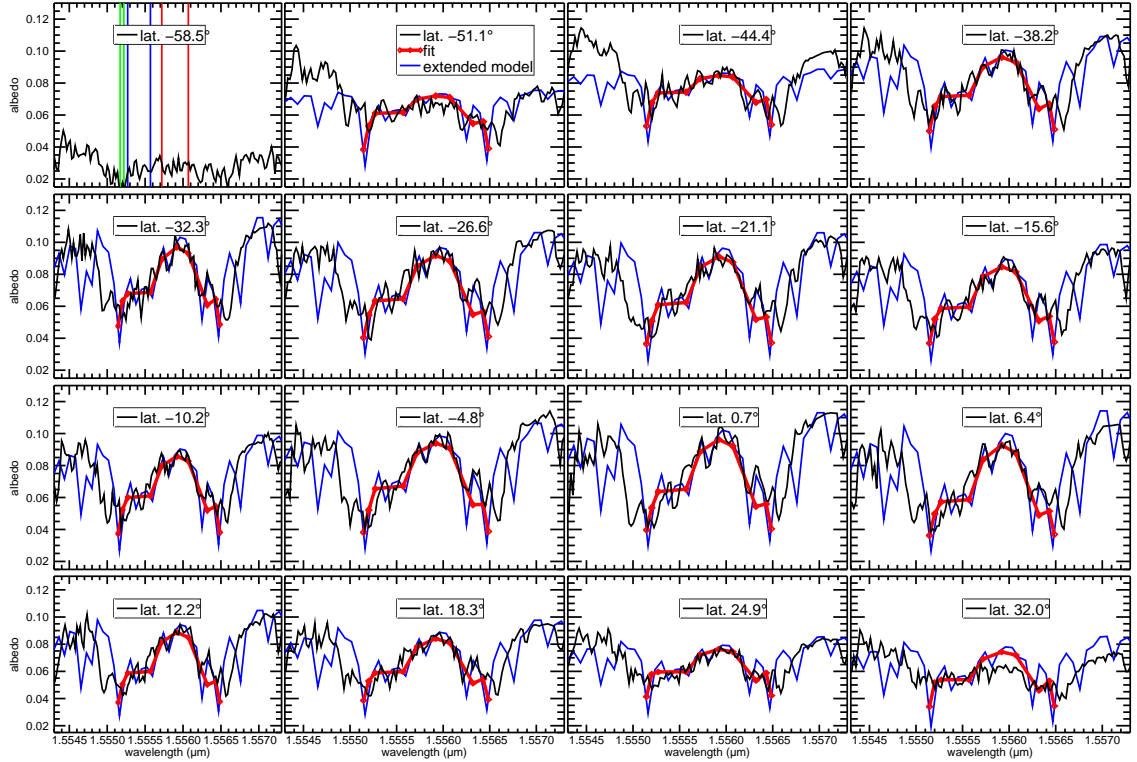


Figure 4.3 The 16 measured spectra (black lines), along with the best model fits (red lines). The 3 southernmost and the 1 northernmost spectra are flattened by the higher opacity near the limb. This loss of the methane feature, along with the high variation in the lighting geometry within each pixel, makes the determinations of the model parameters unreliable at these locations. The vertical lines in the first spectrum indicate the wavelength ranges used to measure the 3 indicators: 1.55572-1.55607 μm for i_0 (red), 1.55517-1.55522 for i_1 (green), and 1.55527-1.55557 μm for i_2 (blue). The blue lines are models calculated with the parameters that provided the best fits, at more wavelengths than used for building the grids in model space.

start with the methane vertical density profile measured by Huygens GCMS (Niemann et al., 2005). To fit the spectra, we either multiply the GCMS reference profile by a constant factor, or specify the methane vertical profile from its relative humidity at the surface. In the latter case, the mixing ratio is kept constant from the surface to the altitude where saturation is reached, from which 100% saturation is followed until the tropopause. The methane abundance thus is determined by a single parameter, the relative humidity

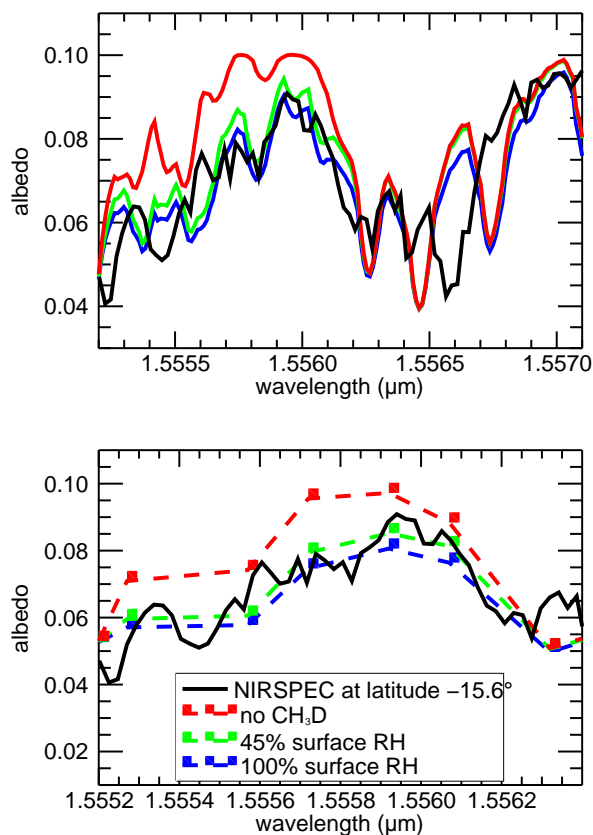


Figure 4.4 Observation at 16°S latitude (black line), compared to models constructed for 45% (green), and 100% (blue) relative humidity at the surface. A model calculated assuming 45% CH₄ humidity and no CH₃D (red line) indicates the differing effects of CH₃D absorption and the poorly constrained CH₄ absorption. In the bottom plot the models were smoothed to a lower spectral resolution, to better indicate how spectra vary over the whole CH₃D feature, without the effects of the high resolution CH₄ structure.

at the surface, which is varied to fit the different spectra.

The CH₃D absorption was calculated with the coefficients measured in the laboratory by Boussin et al. (1999, 1998), and Lutz et al. (1983). The CH₄ absorption coefficients include corrections to the laboratory measurements, derived from Saturn spectra (de Bergh et al., 1988, 1986). As described by Tomasko et al. (2008c) and Penteado *et al.* (2009, submitted), the haze phase function was determined directly from the DISR observations, then fit to fractal particles. The haze optical depth is defined in 3 different regions: it

decreases exponentially with a scaleheight of 65 km above 80 km, and increases linearly with decreasing altitude following different slopes within the regions 80-30 km and 30-0 km. Its wavelength variation is a power law, with different coefficients at each of these 3 altitude regions. The single scattering albedo also follows different functions for each of these 3 altitude regions, and is a linear interpolation in wavelength from the DISR measurements at 0.4-1.6 μm .

We interpret the data by matching it to calculated spectra at 3 wavelength regions (referred to as indicators), which are 1.55572-1.55607 μm for indicator i_0 , 1.55517-1.55522 μm for indicator i_1 , and 1.55527-1.55557 μm for indicator i_2 , as shown in the first spectrum of figure 4.3. Figure 4.5 presents the latitudinal variations of the 3 indicators, along with those of the best model fits. The indicators were chosen to maximize their different responses to changes in the methane abundance, haze scattering and surface albedo. As shown in figure 4.6, i_0 is the most sensitive to the methane abundance, while i_1 is saturated over most of the methane abundance range considered. Variations in surface albedo least affect i_1 , which therefore indicates the scattering due to clouds and haze. Intermediate between i_0 and i_1 , is i_2 , which differentiates between changes in methane absorption and surface albedo. Figure 4.7 displays the effect of methane variations on the indicators; we can see that i_0 is sensitive to the methane abundance in the lowest 10 km of Titan's atmosphere. Uncertainties in the CH_4 line parameters affect our results such that an error of 20% in CH_4 optical depths causes a change in the vertical contribution peak of 7% for i_0 , 5% for i_2 , and 0.5% for i_1 .

Our initial model adopted the DISR haze parameters and Huygens GCMS methane profile, derived for 10°S latitude, which were adjusted to interpret spectra at other latitudes. We find that only 3 parameters need to be changed to reproduce the 3 indicators within their noise levels. The parameters are the methane abundance, the haze optical depth above 80 km and the surface albedo, which affect the 3 indicators as shown in figure 4.6. Model spectra were calculated in a uniform grid in the 3D space of these model parameters, and the fits were obtained from the combination that resulted in the best match on the 3D indicator space.

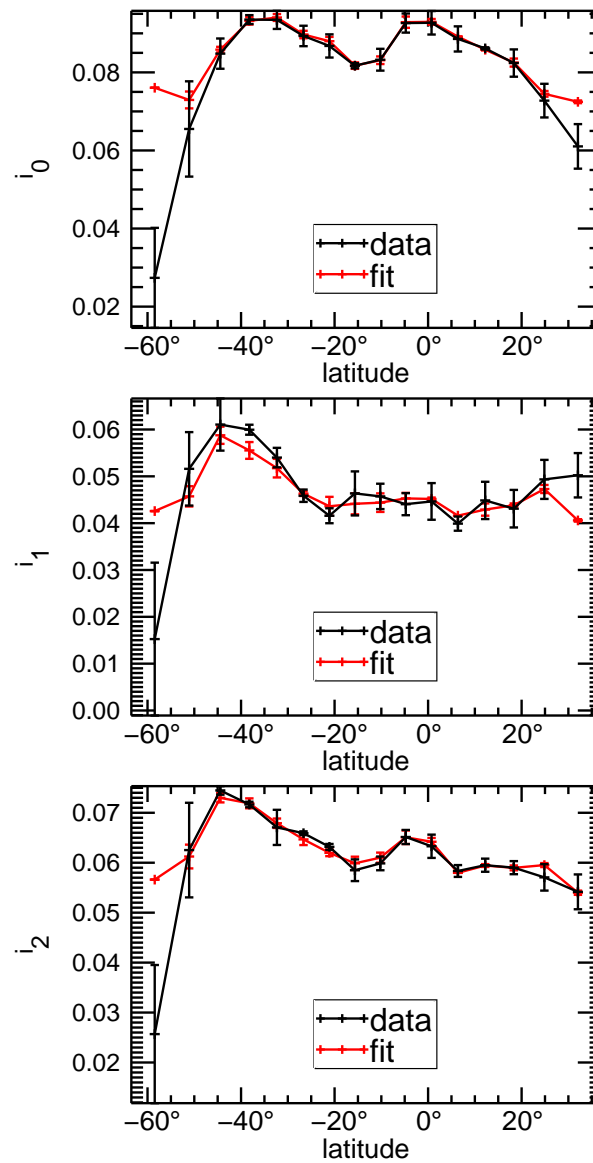


Figure 4.5 Latitudinal variations of the 3 indicators, calculated for the data (black line) and model spectra (red line). The anomalies at the 4 endpoints (3 to the south and 1 to the north) result from the proximity to the limb, which causes a large variation in geometry and optical depths within each spatial pixel. The uncertainties in the data indicators are derived from the variation within the 3 spectra that were averaged to make each one of the 16 spectra used.

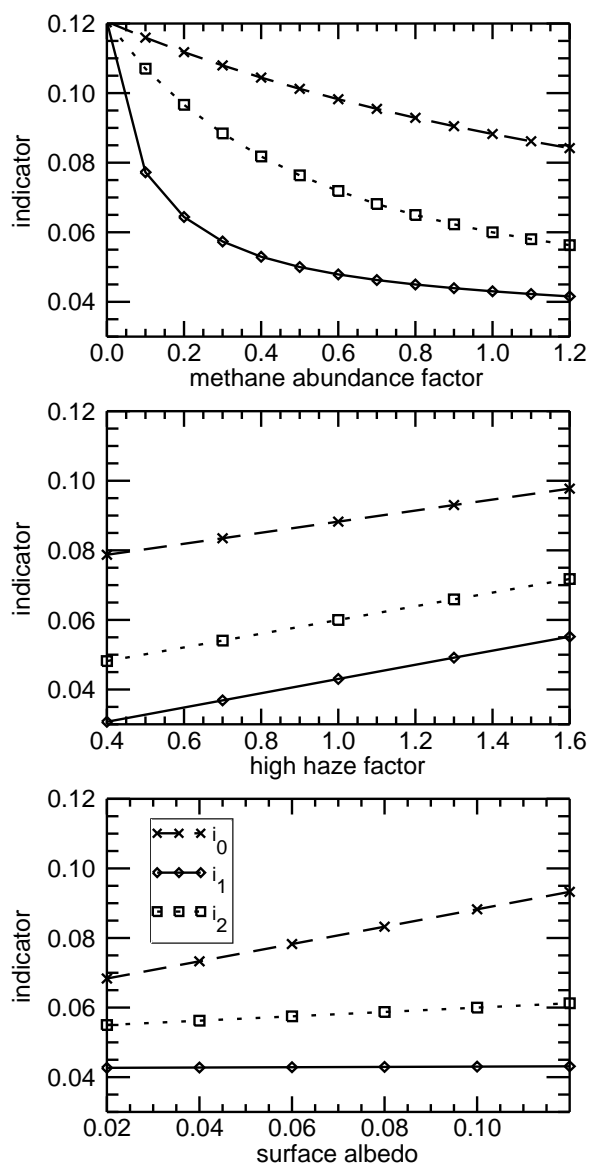


Figure 4.6 Variation in the 3 indicators as a function of changes on the 3 model parameters. For each curve, the two model parameters not being varied were kept at their reference values (1.0 for methane abundance factor and high haze factor, 0.1 for surface albedo). These curves, along with figure 4.7, indicate that i_1 (solid line) is at a region of saturated methane absorption. Thus variations in i_1 mostly indicate variations in the haze.

4.3 Results

The results are shown in Figure 4.8, along with the uncertainties that result from their derivation from the mean data indicators. The noise level and overlapping effects of the

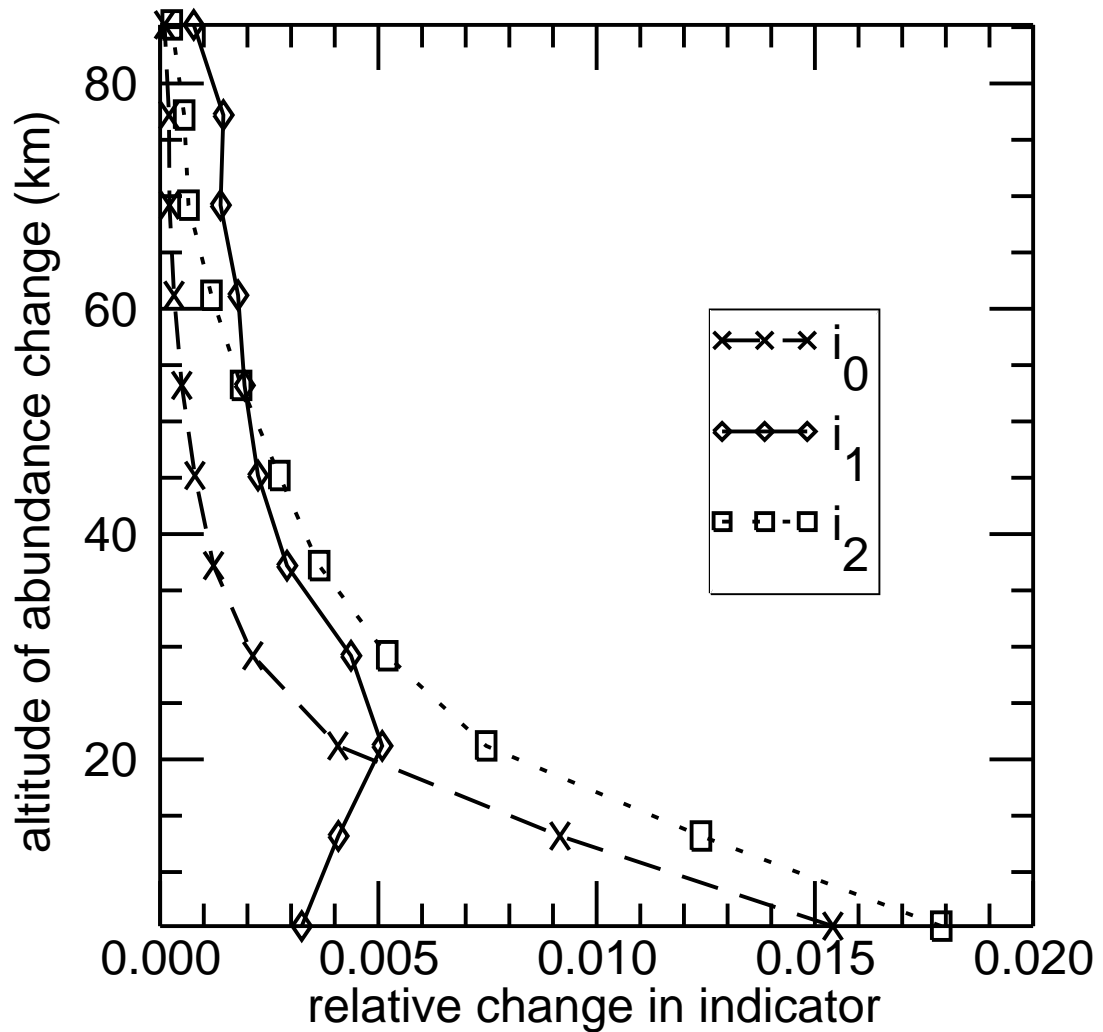


Figure 4.7 Relative variation of the 3 indicators as a function of the altitude where the methane abundance is changed. The abundance is changed in a 5 km region by a multiplicative factor that is a linear function of altitude, from 0.5 at the indicated altitude, to 1 (no change) 2.5 km away. These profiles, along with figure 4.6, show that i_0 (dashed line) is most sensitive to the methane, i_1 (full line) is most sensitive to the haze, and i_2 (dotted line) is intermediary.

methane, haze and surface albedo prevent us from measuring relative methane variations smaller than 20%. Above this level, we find no change in methane abundance over the

range 32°S-32°N. These uncertainties equivalently permit variations smaller than 10% for the humidity above the surface. We derive a $25^{+40}_{-15}\%$ increase in haze optical depth above 80 km from 10°S to the equator, in agreement with that determined from analysis of VIMS data (chapter 6 and Penteadó *et al.* 2009, submitted). The derived surface albedos agree with the values derived for the same terrain using VIMS observations at 1.5567 μm . The ratio between highest and lowest surface albedos, $2.2^{+0.5}_{-0.3}$, is larger than the range found from the DISR observations at $\sim 1.6 \mu\text{m}$, of a different surface terrain (Keller *et al.*, 2008).

Between 32°S and 51°S, the derived increase in haze optical depth, indicated by the sharp increase in Titan's albedo at 1.5552 μm (i_1 , figure 4.5), suggests the presence of methane clouds on that region. Methane clouds typically observed south of 40°S (Roe *et al.*, 2005a; Griffith *et al.*, 2005a; Roe *et al.*, 2005b; Porco *et al.*, 2005; Griffith *et al.*, 2005a; Brown *et al.*, 2006; Roe *et al.*, 2005b; Schaller *et al.*, 2006a; Gendron *et al.*, 2004; Gibbard *et al.*, 2004; Bouchez and Brown, 2005; Schaller *et al.*, 2006b) obscure the troposphere and are brighter than the surface. Thus clouds decrease the depths of methane absorption features. There is no independent constraint on the presence of clouds at the time of the observation, because there were no coinciding VIMS observations. Also the limited time available prevented us from recording lower resolution spectra, which would have revealed the cloud effects (as discussed in Griffith *et al.* (1998)).

Our analysis demonstrates that high resolution ground-based data can measure methane abundance in the lower troposphere across Titan's disk. The $3\nu_2$ CH₃D lines probe the methane down to the surface, and thus complement lower resolution spectra (e.g. by Cassini VIMS, chapter 6) that measure the methane near the tropopause.

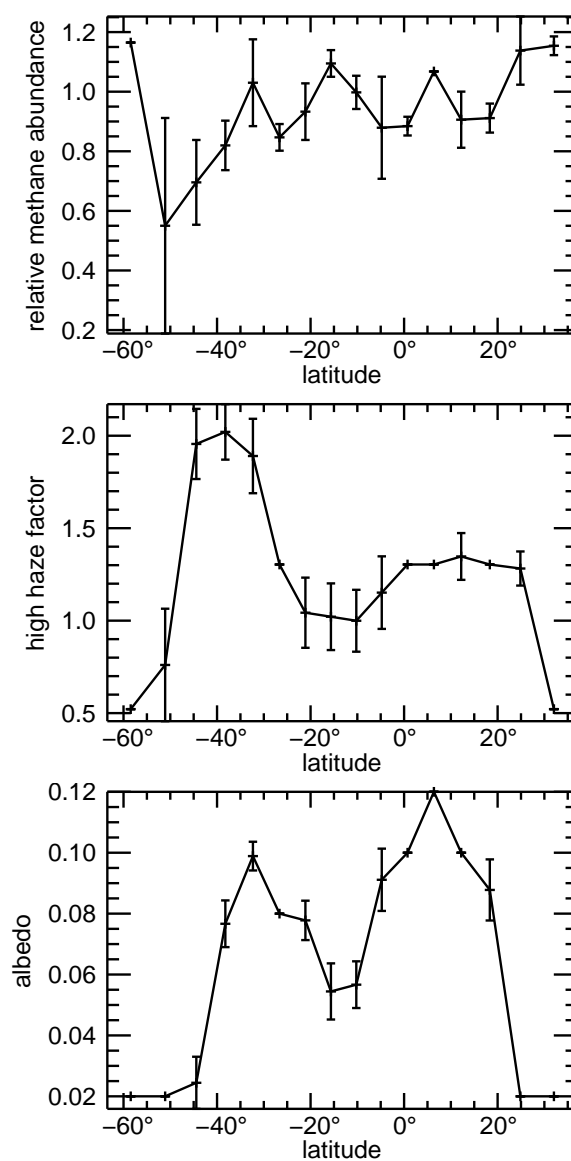


Figure 4.8 The model parameters that resulted in the best fits to the data. These parameters are: the factor multiplying the Huygens GCMS methane profile (top), the factor multiplying the haze optical depth above 80 km (middle), and the surface albedo (bottom). The errorbars are the standard deviations in the determination of the 3 model parameters: changes in the parameters within these ranges provide synthetic spectra that match the observed spectra within their uncertainties.

CHAPTER 5

CASSINI VIMS OBSERVATIONS OF TITAN

5.1 Instrument characteristics

Most of the work on this thesis is based on analysis of data from Cassini VIMS, including characterization of different clouds (chapter 1), and spatial variation of haze and methane (chapter 6). The complexity and large volume of this dataset thus required significant work on systematic calibration, visualization and selection capabilities, discussed on this chapter.

VIMS is an imaging spectrometer that produces 3 dimensional hyperspectral observations (commonly referred to as cubes) of two contiguous spatial dimensions, and one contiguous spectral dimension. VIMS covers the visible and near infrared spectrum between $0.35 \mu\text{m}$ and $5.12 \mu\text{m}$ in two channels that have independent optics and detectors, and thus different characteristics. Figure 5.1 shows a typical Titan spectrum on each channel, and figure 5.2 shows images at each band of that cube.

The VIS channel covers the region $0.35\text{-}1.05 \mu\text{m}$, in 96 bands of constant 7.3 nm width in wavelength, each formed by the sum of 5 1.46 nm pixels. It uses a telescope with 143 mm focal length at $f/3.2$, which provides a $1.83^\circ \times 1.83^\circ$ field of view. The spatial coverage is resolved in up to 64×64 square 0.5 mrad pixels, each formed by the sum of 3×3 0.167 mrad pixels. The detector is a 512×256 (for the spectral and spatial dimensions, respectively) Si CCD. The detector has a 2D instantaneous field of view (one spatial and one spectral dimension), with the other spatial dimension acquired moving the mirror which projects the image on the CCD, so that the next CCD frame will contain the adjacent spatial row.

The IR channel covers 0.85 to $5.12 \mu\text{m}$ in 256 bands of constant 16.6 nm wavelength width. Its image is provided by a 426 mm focal length telescope, at $f/18.6$, to also provide a $1.83^\circ \times 1.83^\circ$ field of view in up to 64×64 effective $0.5 \times 0.5 \text{ mrad}$ pixels, in normal

resolution mode. In this mode, each spatial pixel is formed by combining 2 0.25x0.50 mrad pixels. In high resolution mode, the pixel summing is disabled, thus providing up to 64x64 0.25x0.50 mrad pixels. The IR channel InSb detector, contrary to the VIS channel CCD, is 1D (256 pixels, for the spectral dimension). Thus the instantaneous field of view in IR is 1 spectrum (1 spatial pixel). The IR cube is formed simultaneously to the VIS cube, with the IR mirror moving across the direction of one row (taking successive CCD reads, one for each spatial pixel), during the time that that row is exposed on the VIS channel. The two channels have closely matching fields of view, shifted in their centers by 1.29 and 1.94 pixels, so that cubes taken in normal resolution mode have very similar spatial coverage between the channels. Despite the similar spatial coverage, due to the different directions and possibly different shapes (depending on the IR channel resolution used) of their fields of view, matching the same spatial pixel on both channels is not always possible. Even when the area of interest is contained in both fields of view, matching the spectra of the same region in both channels is not a simple shift in pixel coordinates, since the field of view shift is not an integral number of pixels, and pixels may be of different sizes on each channel.

5.2 Data visualization

As a VIMS cubes contains images in up to 352 spectral bands, visualization and identification of the structures with different spectral characteristics presents another challenge. Simultaneous visualization of all bands is thus only possible by placing the image of each band next to each other. Though subtle combined spectral and spatial variations are difficult to detect this way, these multiple images provide a convenient way to quickly review the contents of all the cubes as they are received, and thus images as figure 5.2 were produced systematically for all cubes received, after their radiometric and geometrical calibration.

A monochromatic color mapping for each individual band, as in the grayscale mapping in figure 5.2, or direct RGB or other standard mappings, is usually limited to 8 bits (256 levels) of dynamical range per band, which is narrower than the range of VIMS,

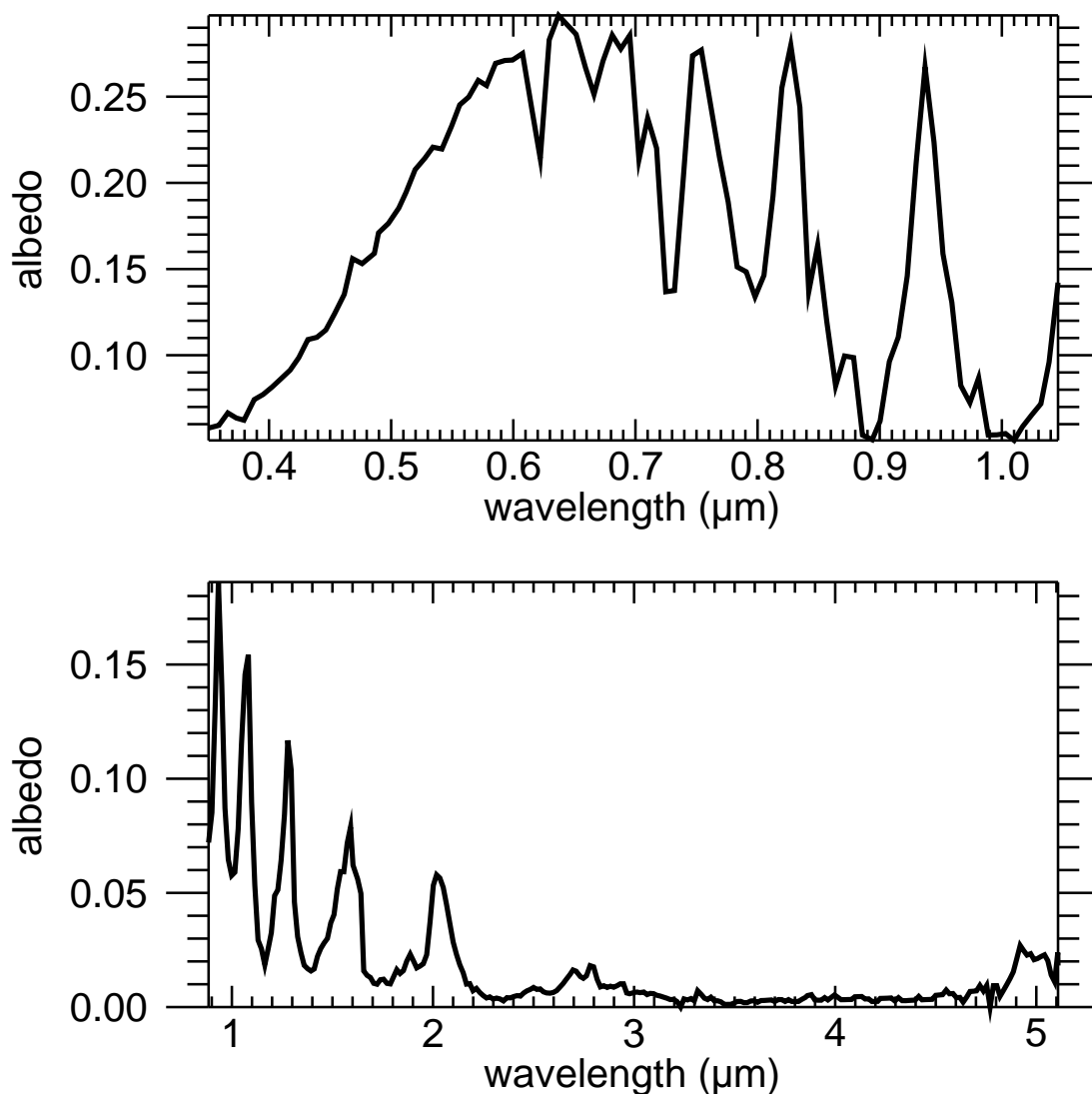


Figure 5.1 A typical VIMS reflection spectrum of Titan, of the VIS (top) and IR (bottom) channels. Both channels have uniform wavelength sampling, with 96 pixels in the VIS channel, and 256 pixels in the IR channel.

which records each band at 12 bits (4096 levels). To decrease the low and high level saturation when making monochromatic images, we developed different functions to map the colors from a larger than 8 bit monochromatic range to a subset of the 24 bit RGB space typically available for computer displays. The challenge for making useful colormaps is

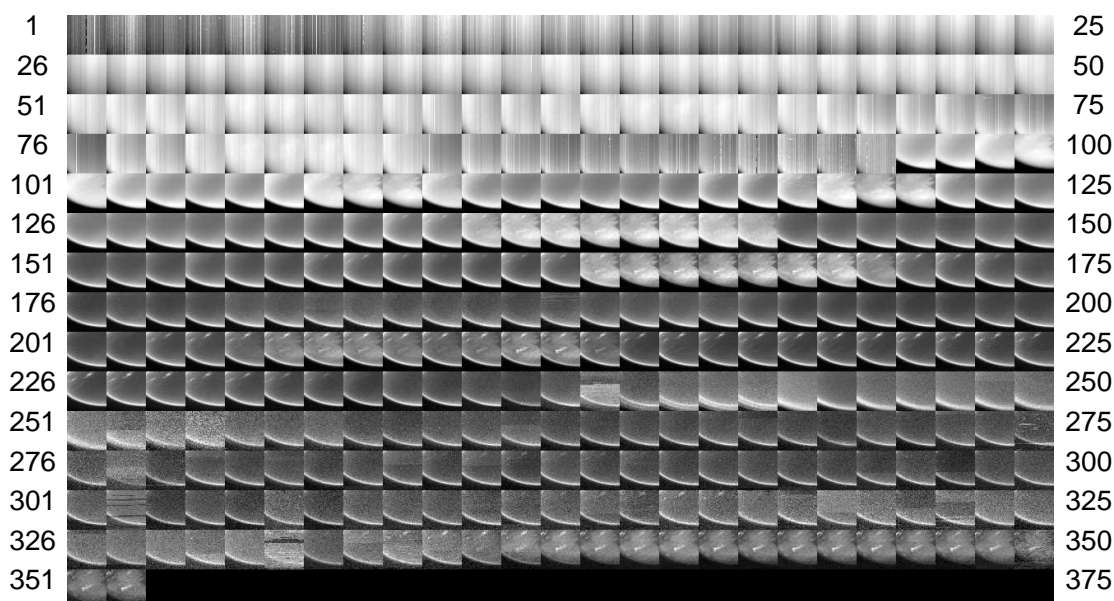


Figure 5.2 Images of each of the 352 VIMS bands from a single cube of Titan in the daytime. The image of each band was renormalized, so that black is the band's minimum, and white is the band's maximum, with linear variation in albedo in between. Figure 5.1 indicates how much the actual albedos vary over the bands. This cube was taken in high resolution mode, which doubles the vertical spatial resolution in the IR channel, which is shown by the difference in Titan's shape between the first 96 (VIS) and the last 256 (IR) images.

to find mappings that run over the 24 bit RGB space with a smooth color variation, while avoiding perceptually similar colors for distant regions in the domain. This problem is further complicated by the variable gamuts and color calibrations of different devices used, in particular the difference between the RGB in computer monitors and the CMYK in printers. Figure 5.3 shows a comparison of the same VIMS band, mapped into 256 levels grayscale, two commonly used 256 levels colormaps, and 3 of the wider maps we developed, with 766, 1276 and 1786 levels. Careful choice of one of those expanded maps, along with the low and high saturation levels, thus reveals simultaneously more spatial structure in the dark and bright regions of the image, than is possible with the standard 256-level maps. As the middle 2 images in figure 5.3 show, the common choice

of "rainbow" colormaps is frequently inadequate, as it suppresses the contrast of over a broad range of middle values, which gets mapped into perceptually similar hues of blue, cyan and green.

The 3 maps we defined in figure 5.3 are made by linear variations in RGB space, as shown in figure 5.4. If the variable to be displayed is cyclical, in which one end of the scale should be joined to the other (such as angle related variables), these colormaps can be expanded, by adding a branch which smoothly connects the endpoints. In this case, the 1786 levels map we developed is directly extended to 2041 levels. Future improvements to these colormaps include tests with maps uniform in the conical HLS and HSV spaces, and to account for the effects of frequency-dependent perception, to achieve perceptually uniform maps (Backhaus et al., 1998; Rogowitz and Treinish, 1998; Rogowitz et al., 1996; Bergman et al., 1995).

Monochromatic mappings from arbitrary functions can be easily made with `titan_browse`, discussed in the next section. However, it is often useful to use the commonly available 3 color dimensions to display directly multiple bands, simple combinations of bands, or complex functions, such as the results of principal component analysis (Bellucci et al., 2004). These are usually done directly mapping each dimension to an RGB color, which is a rectangular mapping. However, 2D combinations of bands frequently have their distribution in shapes that are more similar to cylindrical distributions. This results from pairs of measurements from bands frequently being correlated, with different correlations on regions of different properties, such as presence of clouds or different absorption features. For this purpose, we use 2D color maps based on the distribution of the points in a 2D section of the conical HLS colorspace. Figure 5.5 shows one example, in which the pixels that fall on clouds have a different correlation between the bands used, so that the surface and cloud branches in the 2D band space naturally map to different hues in HLS space. Another such example is the intensity of the 0.61 μm methane band, shown in chapter 6 (figure 6.8).

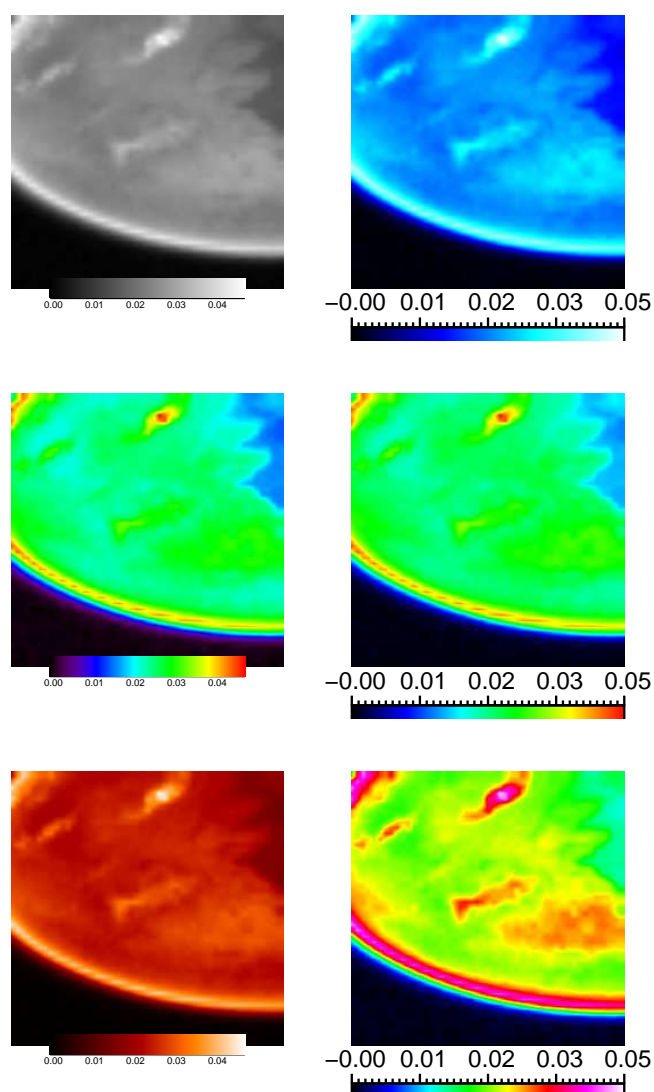


Figure 5.3 The same VIMS $2.71 \mu\text{m}$ image, with different choices of colormaps. The 3 maps on the left are 3 common standard 256-level maps. The 3 maps on the right are some of the expanded maps developed in this work, with 766 (top), 1276 (middle), and 1786 (bottom) levels. The middle left and middle right maps cover similar trajectories in RGB space (figure 5.4), and show the main limitation of the usual "rainbow" choice, a loss of contrast in the middle ranges, due to the perceptual similarity between green, cyan and blue hues. Yet, the middle right map shows more structure, due to its higher color resolution. This image is from the same cube as figure 5.2.

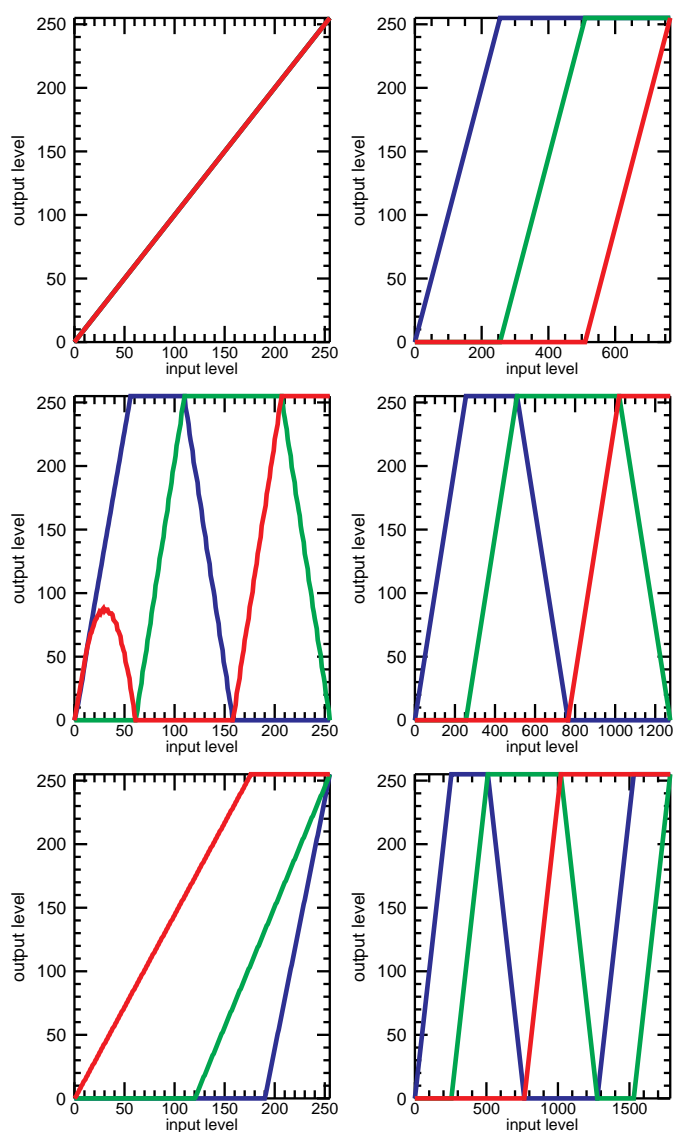


Figure 5.4 The functions that define the colormaps in figure 5.3. These functions map the input image value (measured in the number of resolved levels) to the red, green and blue output values. The output RGB values are always in the range 0-255, as standard computer displays only resolve each channel at 8 bits per pixel. As indicated by the length of the domains, the 3 functions on the left are 256-level maps, while the 3 on the right, defined in this work, are 766, 1276, and 1786 levels. In the top left function only one curve is visible because the 3 curves overlap exactly. Note the progressively wider domains in the 3 maps on the right.

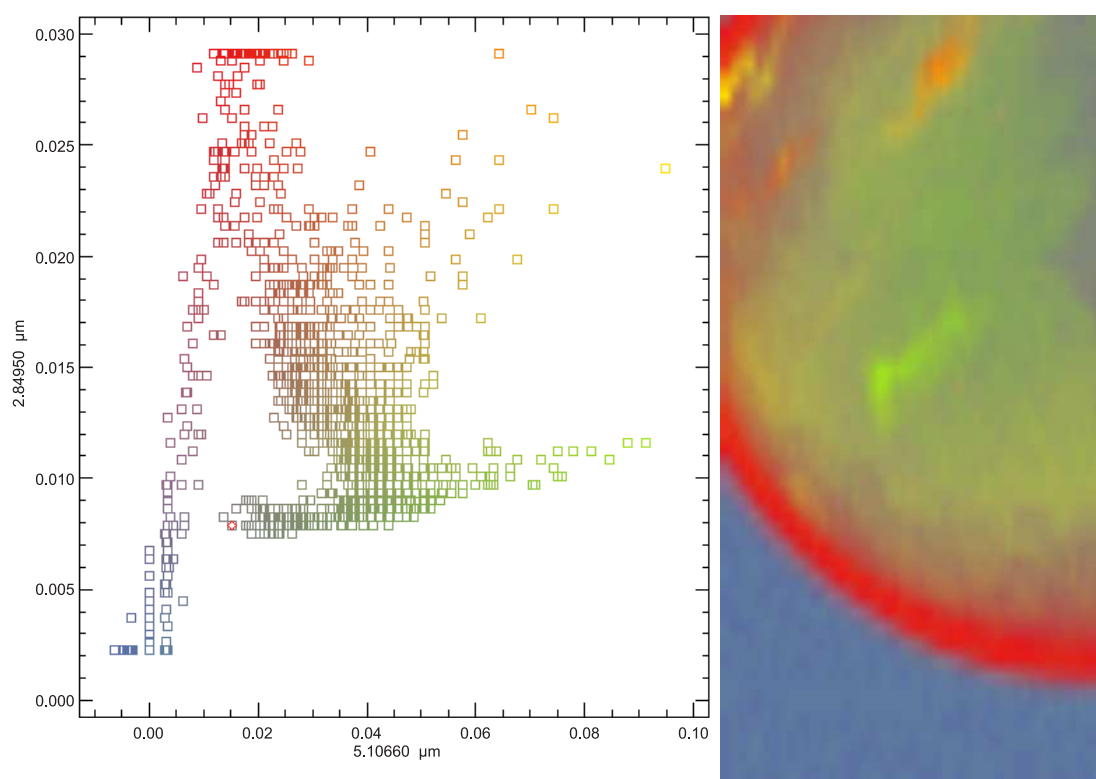


Figure 5.5 Two VIMS bands of the same cube as in figures 5.3 and 5.2. The pixels in the plot and the image had their color defined by their position in the $2.8 \mu\text{m}$, $5.1 \mu\text{m}$ 2D space (plotted on the left). This plane is mapped to the circular section $L=0.5$ of the HLS conical space, in this case with the axis ($S=0$) at $(0.015, 0.0079)$. This provides a greater difference between the colors of the different types of structures, such as the bright surface, the clouds (near the top), and the spectrally distinct brighter surface feature (near the center).

5.3 Data selection

The large number of cubes recorded presents challenges in finding the observations most suitable for any particular study. From orbital insertion (July 2004), to the end of the nominal mission (July 2008), over 1.6×10^4 Titan cubes were recorded (not including those in late downlinks), in which the spectra that intercept Titan's disk exceed 6.2×10^6 . The observations vary greatly in coverage, viewing geometry, resolution, noise levels,

illumination, and features such as presence of diverse types of clouds. The most useful observations might be defined by the presence of spectral features, such as an absorption band, albedo variations or the effects of clouds. Additionally, observations are frequently constructed from a large (up to hundreds) number of cubes that each cover a very small area. These cubes, particularly those that are very narrow (one or few pixels wide in one spatial dimension), can only be well visualized if combined in a mosaic. Therefore, it is unpractical to check for the presence of features of interest, or select observations, just by visual inspection of a limited number of cubes. The size and complexity of the VIMS dataset creates the need for a systematic way to search it. For that purpose, we developed a database of observations and tools for querying and visualizing its contents. The main characteristics required for it were:

- To be able to search the entire dataset for spectra, based on arbitrary characteristics of interest. Of particular importance is that the possible search criteria are flexible, with few predefined constraints. Depending on the purpose of the selection, the criteria might be based on a combination of geometrical, photometrical and spectral criteria.
- To provide convenient and robust visualization and data access of the search results, so that the dataset can be interactively explored, with different selections easily experimented with, and easy production of maps and mosaics of complex spectral functions.
- To be portable, allowing its use by different users, depending only on a compact and portable set of software and data files, without the need for direct access to calibrated cubes.
- To be efficient, working from datasets small enough to require practical amounts of memory and processing power.

The product developed to fulfill these requirements is a combination of a database preconstructed from select information from the cubes, and a tool to make and visualize

the queries. Its interface, named `titan_browse`, is shown in figure 5.6. The large volume of cubes recorded (~ 40 GB to date) means that searching directly in the cube files is unpractical, as it requires the user having all the cubes, organized in a standard way. Most importantly, direct access of the cubes would require reading thorough a very large volume in disk on each search, as the whole dataset cannot fit in RAM, thus making searches impractically slow. Thus the choice for `titan_browse` was to build a small set of database files, containing select information from each cube. This selection contains all the cube information (such as time taken, exposure times, instrument modes) and, for each spatial pixel, all geometrical data (such as emission and incidence angles and latitude and longitude), and the observed I/F on selected bands of most interest (such as bands where the surface is visible, bands that reveal clouds with the most contrast, and bands with absorption/emission features of interest). This reduction allows the database from which selections are made to be small enough (few GB) to fit in RAM, to become practical to work interactively with it.

Only to prepare the database files it is necessary to have the access to all cubes and to the pointing information data and libraries (SPICE, Acton (1999), and the associated data for Cassini VIMS), and other libraries for reading the cubes and accessing SPICE. To use `titan_browse` it is necessary only the database files (only two files per flyby), `titan_browse` and IDL. Database files containing a few standard sets of bands have been built for all the cubes after each flyby. At a lower level, these files are made reading every cube, and storing in linked lists of structures, the cube information (such as flyby, observation sequence, instrument modes, exposure times, plus ranges of the fields for the core bands included) for each cube, indicated in table A.1, and for each spatial pixel, all the cube backplanes (geometrical information such as geographical coordinates and viewing geometry), indicated in table A.2, and the selected bands. The total volume of those database files, which are stored compressed, is only hundreds of MB, depending on the number of spectral (core) bands it includes. As only the available backplanes are constant and the presence of core bands is optional, the core bands are treated by the software in the same form as the backplanes, and are thus referred by `titan_browse` as "extra backplanes".

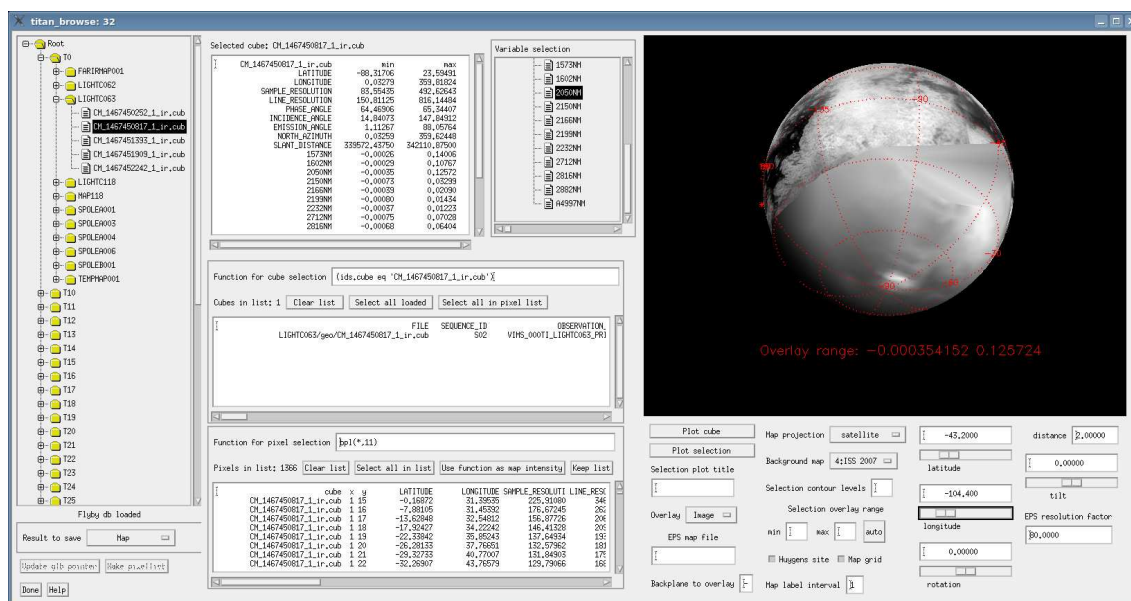


Figure 5.6 The interface of titan_browse. The left panel contains the flyby tree structure, where individual cubes can be selected. The middle panel contains the cube information text (top left), the variable selection tree (top right), and the cube and pixel lists, with their controls (middle and bottom, respectively). The right panel contains the map display and its controls, in this case displaying the function in the pixel selection field ($2.050 \mu\text{m}$ albedo) for all spatial pixels in the list.

The software to access the database, titan_browse, was written entirely in IDL, thus making it seamlessly portable between different platforms, without requiring any additional libraries or other software. The choice of IDL to implement the database, as opposed to using a database server, was also made to allow the user to write functions for spectral selection, instead of only a small predefined set of functions, as it would be the case with standard databases. Selections can be made from any function of the available variables. Portability and freedom of selection criteria are more important to this application than the performance gain that would be obtained from the use of a database server. Other important reasons for choosing IDL were the availability of a large library of standard functions, which can be used when writing the functions for selection, providing a portable environment for the graphical interface, and the ease of writing and maintaining the code.

titan_browse is intended as a search tool that works flexibly with all the cubes, with its visualization tools as an aid for the searches. It is thus complementary to the JBody tool in development by the VIMS support team, which is devoted more to flexible visualization. More information on availability and use of titan_browse is given in appendices A and B.

The analysis of Titan's haze and methane variation discussed in chapter 6 was performed with datasets selected with titan_browse. Those contain large numbers of spectra with similar characteristics, to minimize the effects of variable haze scattering, derived from a large number of cubes collected during the entire nominal mission.

Future improvements to titan_browse include changes in the algorithms for better efficiency, and a reorientation of the database files, so that core and backplane bands constitute the higher level in the structures for the individual pixels. This will allow database files to contain all the bands in all the cubes. The requirement for disk storage will be much larger in this version, but it will be possible for the program to only read into the memory those pixel variables (core/backplane bands) that appear in the function to be executed. Thus the search and plot functions will no longer be limited to the bands selected when the database files were built, and there will be a better runtime efficiency, from only having to read from disk the data actually being used in the selection. This would also allow the extraction of full spectra directly from the database files, since currently titan_browse can only provide the spectra if all the cubes are available, and organized in the same directory structure used where the database files were made.

CHAPTER 6

LATITUDINAL VARIATIONS IN TITAN'S METHANE AND HAZE FROM
CASSINI VIMS OBSERVATIONS

To determine the latitudinal variation of the haze and the upper tropospheric methane, we analyze VIMS observations at 0.4-1.6 μm , where variable haze and methane optical depths result in the spectra sampling variable altitudes on Titan's atmosphere.

Figure 6.1 shows the altitude where the downward and upward fluxes reach half their value. This provides an indication of the variation with wavelength of the altitudes where the spectra are most affected by the haze and methane, which cover the lowest 200 km of Titan's atmosphere.

6.1 Observations

The observations were recorded during the 2004-2008 period, thus entirely in the southern summer, which extends from 2002 to 2009. Figure 6.6 shows a typical spectrum for the Huygens probe region, along with calculated models.

The haze is not fully known at every location on Titan, and its scattering is highly forward peaked. Thus the spectra recorded across Titan's disk in any single observation are affected by spatial variations in the haze and observing geometry. For a typical observation the phase angle does not vary by more than 2° over the entire disk; the variability in incidence angle most strongly affects the continuum level of the spectra, which for example changes by 22% as the incidence angle changes from 50° to 60° , for a phase angle of 70° . To remove the effects of varying scattering geometry, we worked with samples of spectra with similar geometry, with subsolar latitudes from 24.1°S to 6.6°S . The methane and haze variations were derived from 13 averaged VIS and IR channel spectra at different latitudes from 3 selections (1-3, table 6.1), taken between the T0 (3 July 2004) and T26 (10 March 2007) passes, as well as a more extended data set of 10988 VIS channel

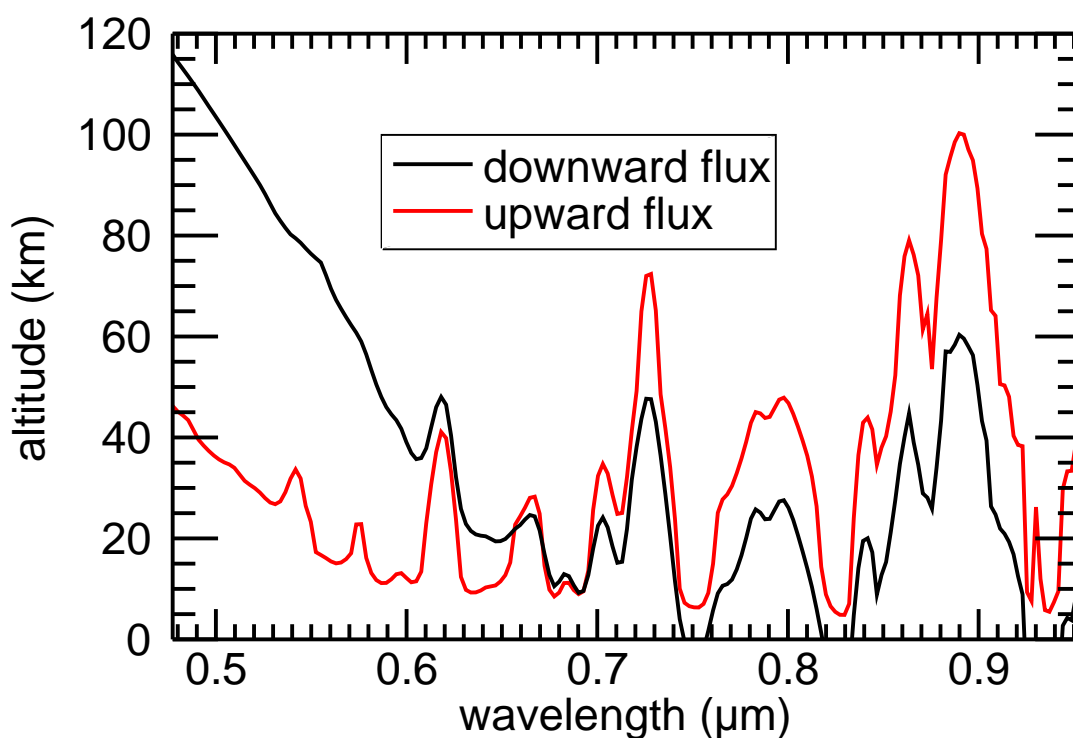
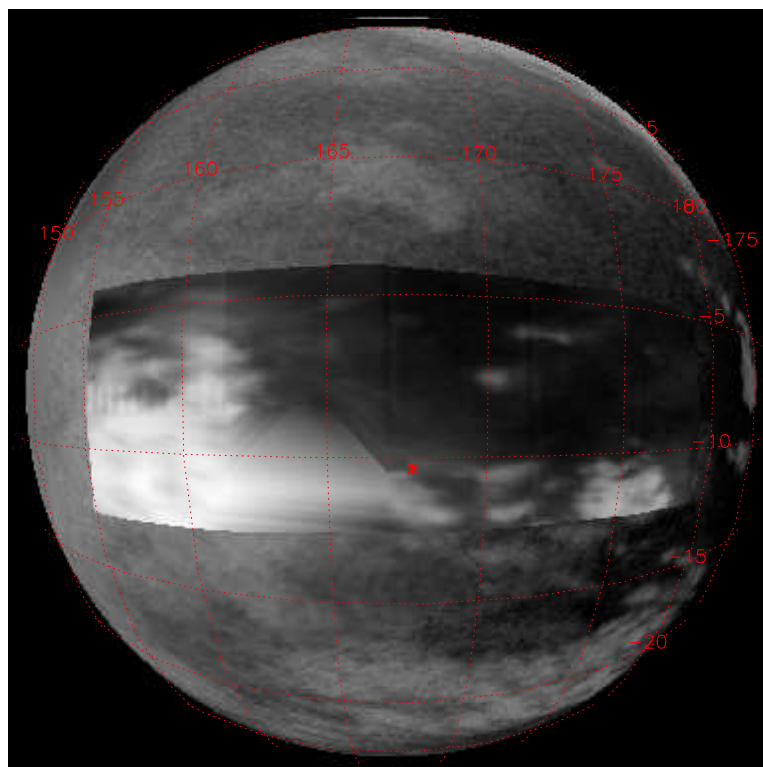


Figure 6.1 Altitudes where the model downward and upward (black and red, respectively) fluxes on Titan's atmosphere reach half their maximum value, in the region covered by the VIMS VIS channel. The downward flux is the sum of the direct solar flux and diffuse flux from scattered light. The altitudes for the upward flux indicate the altitude region where the spectra are most sensitive to the methane and haze. The altitudes for the downward flux indicate the altitude region where most absorption and scattering occurs.

spectra taken between the T0 and T42 (25 March 2008) passes (selection 4, table 6.1). The latter selection allows us to quantify uncertainties due to systematic errors and noise. To directly map the spatial variation of the continuum characteristics, indicative of the haze, and the 0.61 μm band depth, we used one VIMS cube taken at low phase angle during the TB flyby (12 October 2004), that covers Titan's entire disk in a single image. This observation was recorded at a phase angle of 16° , at 7.7×10^4 km from Titan, and the best spatial resolution on Titan's surface was 130x90 km/pixel (figure 6.8).

Table 6.1 Geometry of the datasets used for this analysis.

Selection	Spectra	Incidence	Emission	Phase	Latitude	Longitude	Period
1	21	42.86°-47.13°	41.82°-44.01°	17.80°-18.18°	12°S-4°S	180°W-205°W	12/Oct/2004
2	31	38.24.25°-41.39°	28.05°-31.65°	63.28°-65.54°	61°S-18°N	4°W-360°W	Jul/2004-Mar/2007
3	12	53.23°-55.67°	29.51°-31.65°	68.01°-69.94°	52°S-41°N	156°W-345°W	Jul/2004-Mar/2007
4	10988	53.25°-56.75°	25.00°-35.00°	60.00°-76.78°	80°S-45°N	0°W-360°W	Jul/2004-Mar/2008



Overlay range: 0.0456856 0.0988085

Figure 6.2 $2.0 \mu\text{m}$ image of the location of the spectra contained in dataset 1. This is the only selection made from entire cubes in a contiguous region, as all cubes are a high resolution mosaic of a small area. The image on top of the background is a mosaic of the $2.0 \mu\text{m}$ band on all pixels in that selection, in a satellite (perspective) projection. The point marked with the red "*" is the Huygens site. The background image is the ISS October 2007 base map.

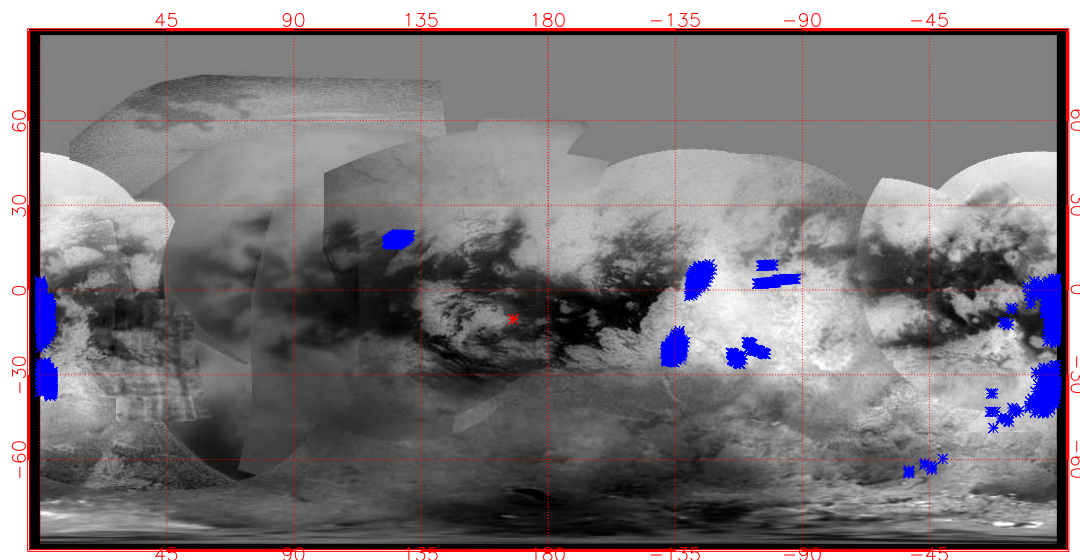


Figure 6.3 Location of all the spectra in selection 2 (blue symbols), on top of the ISS October 2007 base map, on a cylindrical projection. The point marked with the red "*" is the Huygens site.

6.2 Radiative transfer modeling of Titan's spectrum

We begin with the haze and methane profiles derived from the Huygens probe data and determine the alterations thereof that are needed to interpret the VIMS spectra of other latitudes and longitudes. We first analyze VIMS data of the landing site with the opacity model derived by DISR. The Huygens probe collected *in situ* data of Titan's atmosphere during its descent on 14 January 2005. Besides imagers, the DISR instrument contained upward and downward looking spectrometers ranging from 0.35 to 1.6 μm , a sun sensor, and a solar aureole camera, which recorded the intensity profile near the sun. From

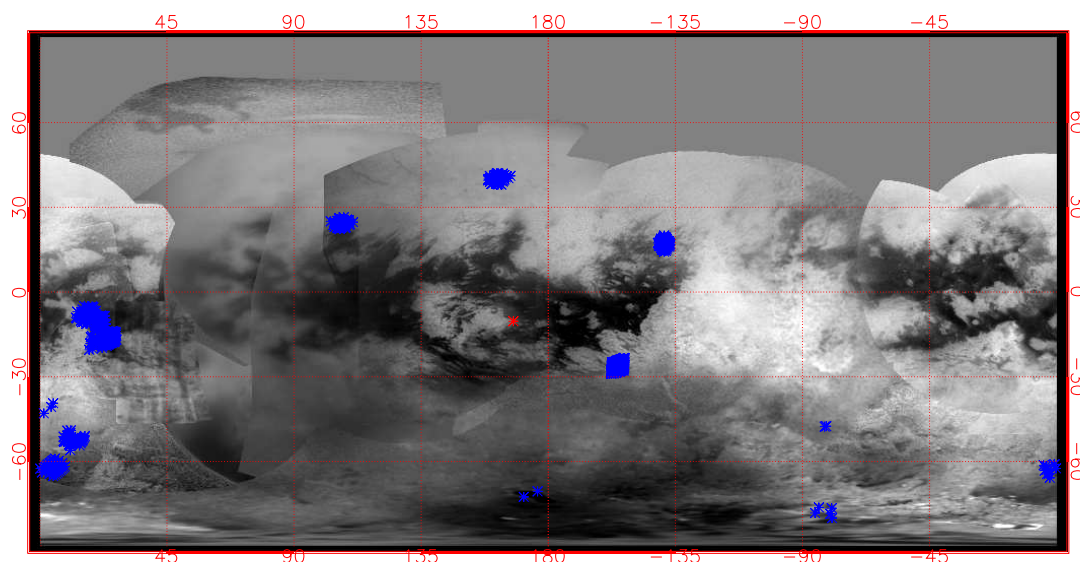


Figure 6.4 Location of all the spectra in selection 3 (blue symbols), on top of the ISS October 2007 base map, on a cylindrical projection. The point marked with the red "*" is the Huygens site.

this data a model of Titan's aerosols was created as described by Tomasko et al. (2008c). The DISR measurements constrain the vertical distribution and wavelength dependence of opacity, single scattering albedo, and scattering phase function of Titan's aerosols. Comparison of the aerosol properties to computations of scattering from fractal aggregate particles indicates the size and shape of the aerosols. The data suggest three strata of different aerosol characteristics, with their opacity having stronger wavelength dependence above 80 km than below and decreasing further below 30 km.

First we analyze a small representative sample of spectra (selections 1-3, table 6.1),

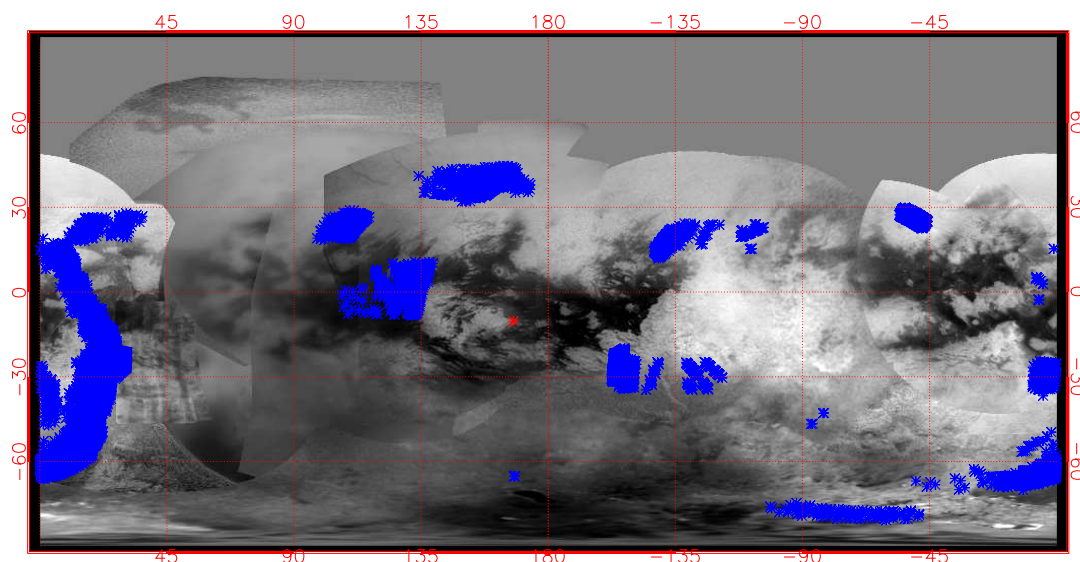


Figure 6.5 Location of all the spectra in selection 4 (blue symbols), on top of the ISS October 2007 base map, on a cylindrical projection. The point marked with the red "*" is the Huygens site.

to determine how the haze and methane must be changed to fit the observed spectral variation. For this analysis we use the doubling and adding algorithm that was developed and employed by the DISR team for the analysis of DISR observations (Tomasko et al., 2008c). This algorithm provides accurate solutions with no approximations of the form of the phase functions or intensity fields. Selection 4 extensively samples Titan's disk at similar geometries, to measure the spectral variation at every latitude. For the larger number of spectra in selection 4, we approximate the radiative transfer solution with a less computationally intensive discrete ordinates algorithm (DISORT, Stamnes et al. (1988)),

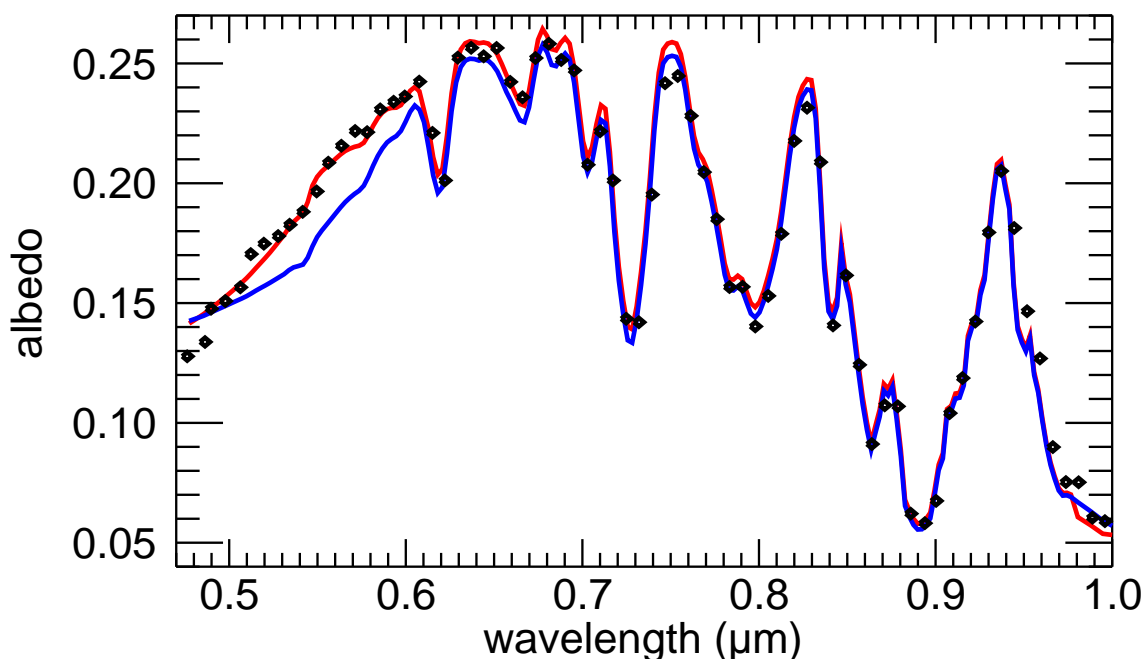


Figure 6.6 Comparison of VIMS observations (diamonds) recorded at 10°S and 181°W , near the Huygens Landing Site with a model generated from the DISR data. The blue line is the original model derived from the DISR observations. The red line is the DISR model with the DISR haze adjusted within its uncertainty, as indicated in figure 6.10, to more closely match the VIMS data between $0.5\text{-}0.6\ \mu\text{m}$.

with 32 streams and 51 vertical layers. We find that the two different codes are consistent for spectra at the Huygens site. When considering the dependence between haze and methane abundance (discussed in section 6.5), the discrete ordinates code shows a similar relative variation in haze parameters to that found with the doubling and adding code, except for the lowest methane abundances (abundance factors of ~ 0.25 and lower, in figure 6.16).

The methane vertical distribution measured by the Huygens GCMS (Niemann et al., 2005) was assumed in the analysis of VIMS spectra at 10°S latitude, that of the probe landing site. The methane absorption coefficients are calculated with band models derived from an analysis of the Huygens DISR and GCMS measurements, described by Tomasko et al. (2008a). We initially adopt the haze parameters (vertical density distri-

bution, phase function and single scattering albedo) for the landing site as derived by the DISR observations. The surface is not visible at $0.6 \mu\text{m}$, and thus the surface albedo was kept constant in the analysis of the $0.61 \mu\text{m}$ band. As described by Tomasko et al. (2008c), the haze scattering phase function was determined by a fractal particle model that fits the values observed by DISR at $0.4\text{-}1.6 \mu\text{m}$. Vertically, the phase functions change only at 80 km altitude. The vertical optical depth profile has 3 different sections: Above 80 km, it falls with altitude exponentially with a scaleheight of 65 km. Below 80 km, it increases linearly with decreasing altitude, at different slopes for 80-30 km and 30-0 km. The wavelength variation in optical depth is defined by a power law, with different coefficients at each of these 3 altitude regions. The single scattering albedo is a linear interpolation between the wavelengths of the DISR measurements, which change at 80 km altitude.

6.3 Approach

We initially examined VIMS observations covering the whole disk, to acquire a first order understanding of the variation of the $0.61 \mu\text{m}$ methane band depth. We sampled the VIMS data at 4 bands that cover the continuum and the methane absorption. We define A as the albedo at $0.5342 \mu\text{m}$, B as the average of the albedos at $B_1=0.5994 \mu\text{m}$ and $B_2=0.6294 \mu\text{m}$, and C as the albedo at $0.6151 \mu\text{m}$, as shown in figure 6.7. The measures $(B-C)$ and $(B-A)$ give an indication of the variability in the methane band depth and the increased absorption of the haze at lower wavelengths, respectively. Their distributions are shown in figures 6.8 and 6.9, where they are normalized by the cosines of the incidence and emission angles, to decrease the effect of the airmass variations. Figure 6.8 indicates that the measures $\frac{(B-C)}{\cos(i)\cos(e)}$ and $\frac{(B-A)}{\cos(i)\cos(e)}$ are strongly correlated, but they follow different correlations in each hemisphere, with the higher methane band depths towards the south.

The variation shown in figures 6.8 and 6.9 may arise from a latitude variation in haze, in methane, or both: higher haze optical depths obscure the methane in the lower atmosphere, thereby rendering the methane bands shallower for a constant methane abundance. We thus need to determine to what extent the data limits the ambiguity between methane and haze variation. We address this question using three complementary approaches. We

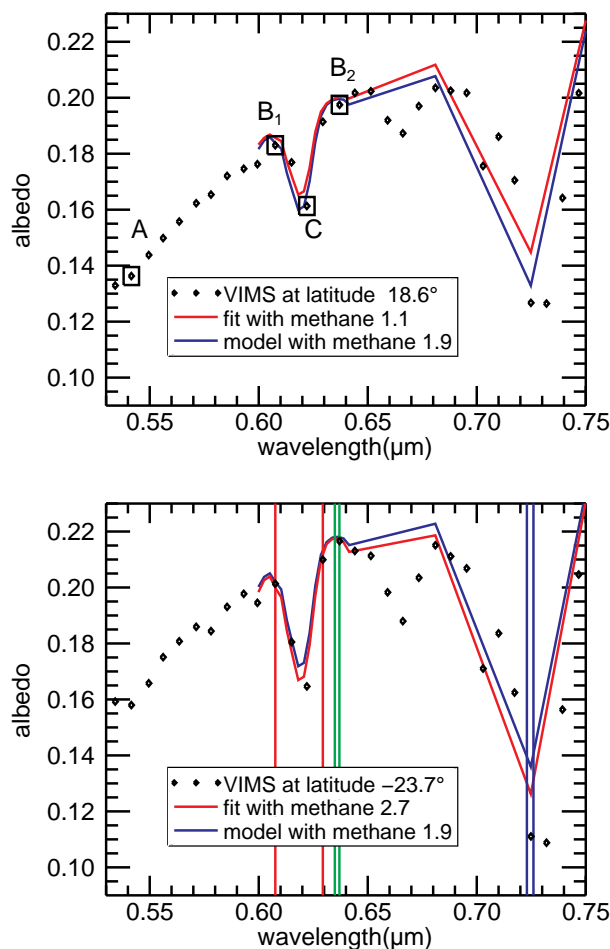


Figure 6.7 Averaged VIMS spectra (diamonds) around the $0.61 \mu\text{m}$ band, at latitudes 19°N (top) and 24°S (bottom). Red lines: model fits, with relative methane abundance factors (defined in section 6.5) of 1.1 (top) and 2.7 (bottom). Blue lines: models with relative methane abundance set to 1.9. The squares on the top show the measures A ($0.5342 \mu\text{m}$), B (average of $B_1=0.5994 \mu\text{m}$ and $B_2=0.6294 \mu\text{m}$) and C ($0.6151 \mu\text{m}$) used to derive figures 6.8 and 6.9. The vertical lines mark the wavelength regions where the 3 indicators (defined in section 6.6) used to measured the data and fits are taken ($0.6076\text{--}0.6294$, $0.6349\text{--}0.6370$ and $0.7230\text{--}0.7260 \mu\text{m}$, red, green and blue, respectively). The regions $0.64\text{--}0.68$ and $0.70\text{--}0.72 \mu\text{m}$ are not used, as those do not affect the values of the indicators.

first analyze the data assuming a constant methane abundance to determine whether haze changes alone can explain the spectral variations observed across Titan's disk (section

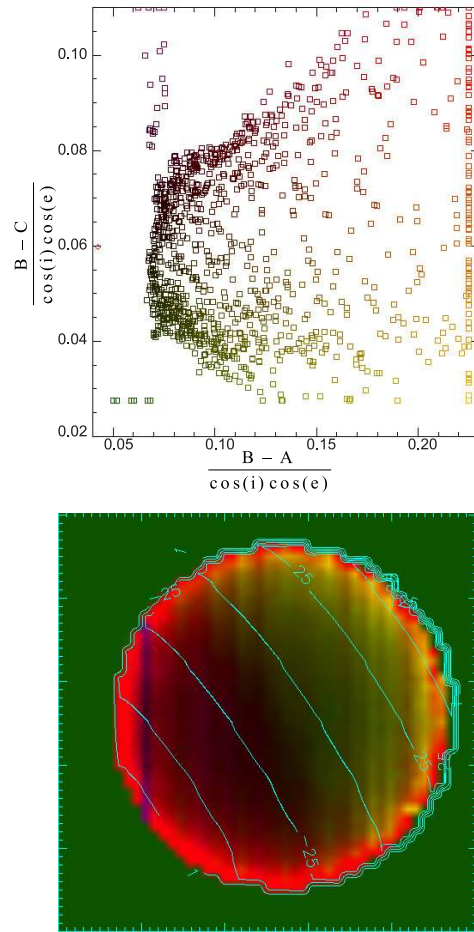


Figure 6.8 Top: The distribution in $\frac{(B-C)}{\cos(i)\cos(e)}$, $\frac{(B-A)}{\cos(i)\cos(e)}$ space of all pixels in one VIMS cube. Each pixel's color is assigned by its location on this plane and is the same color on both figures. The pixels separate in two branches, that map to separate hemispheres on Titan's disk (bottom figure). The methane band depth has a variation (indicated by B-C) independent of that of the haze absorption (indicated by B-A). The higher methane band depths (red hues) occur south of the equator, and the lower band depths (green hues) occur to the north. The red-orange region at the limb is saturated in this colormap due to the high airmass. The cube used is CM_1481501331, from the TB flyby.

6.4). Next we investigate the combined effects due to methane and the haze to constrain the range of possible methane and haze profiles (section 6.5). Finally, the $0.61 \mu\text{m}$ band is further analyzed to determine its variability at each latitude, and its sensitivity to the vertical methane distribution (section 6.6). The constraints that we derive for the latitudi-

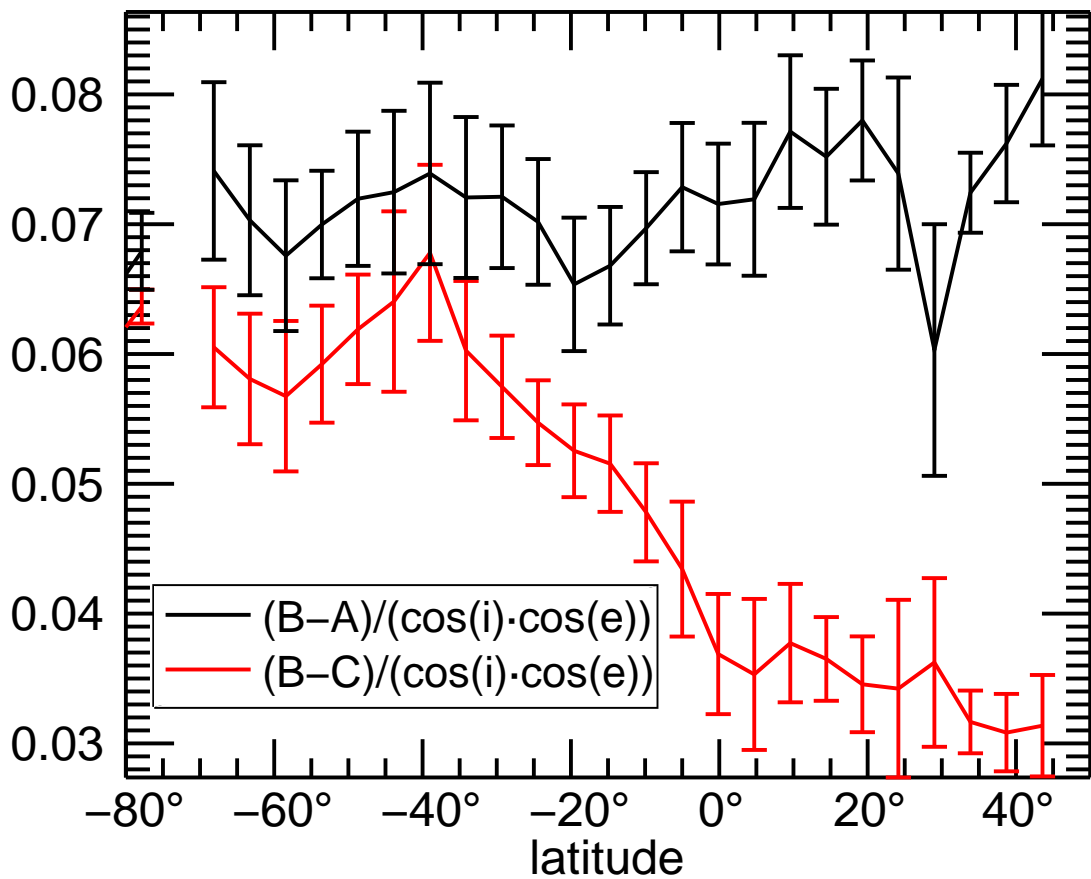


Figure 6.9 Latitudinal distribution of $\frac{(B-C)}{\cos(i)\cos(e)}$ (red), and $\frac{(B-A)}{\cos(i)\cos(e)}$ (black), for all spectra in selection 4. The profiles are averages in 5° latitude bins, with the errorbars indicating their standard deviation within each bin. As indicated by figure 6.8, the methane band depth (estimated by B-C) decreases markedly towards the north.

nal methane and haze variations are used to determine the atmospheric heating rate as a function of latitude (section 6.7).

6.4 Fits with constant methane abundance

The atmospheric model generated from DISR data matches VIMS observations of the Huygens landing site at all wavelengths except between 0.5 and $0.6 \mu\text{m}$ (figure 6.6). The

accuracy of the DISR spectrometer is lower in this region, despite the inclusion of measurements from the violet photometer and blue Solar Aureole (SA) detectors. The lack of precision in this region is due to a small amount of crosstalk from the DISR imagers to the visible spectrometer, the shifting of the bandpass of the SA filters with zenith angle, and the broad bandpass of the violet photometer. Therefore we bias the values for the single scattering albedo in this area toward the edge of the errorbars, as shown in figure 6.10, which produces spectra that agree with both the VIMS and DISR data (figure 6.6).

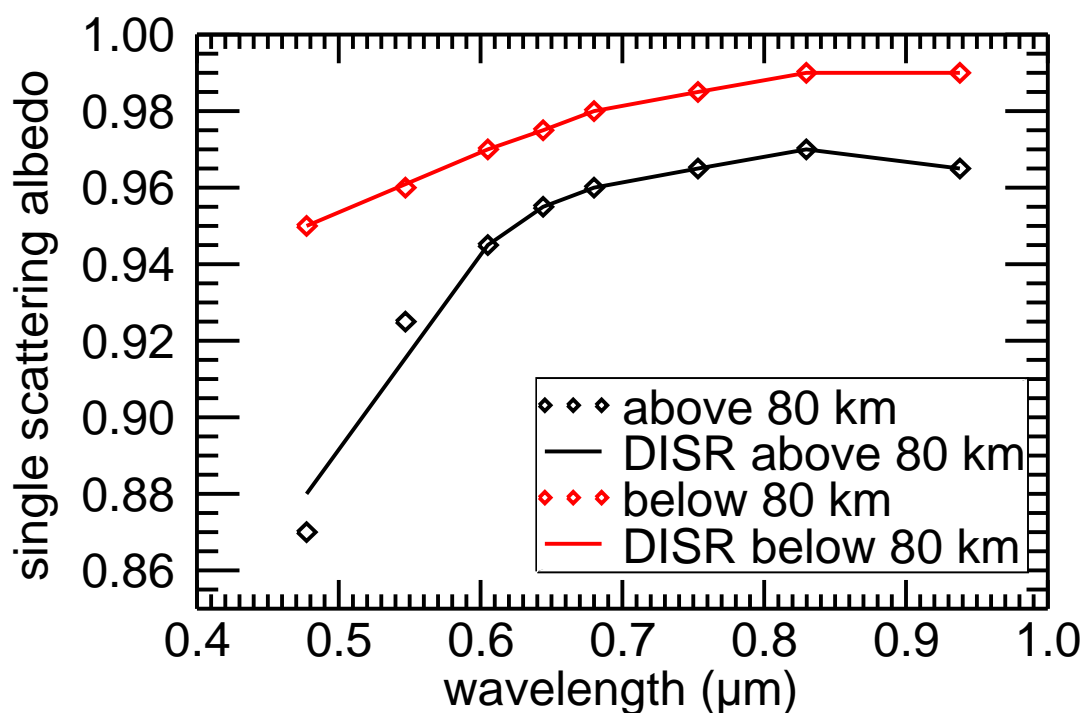


Figure 6.10 Adjustment made to the single scattering albedo in the DISR model in order to better match the shape of the VIMS data in the region where the DISR spectrometer is less sensitive. The lines show the published DISR functions (for above and below 80 km) while the diamonds show the modified functions. There is no change for the region below 80 km (red lines and diamonds).

The marriage of the VIMS and DISR datasets enables the derivation of Titan's global atmospheric properties. The DISR measurements provide constraints on the methane ab-

sorption (at long path lengths and low temperatures), vertical variations in phase function, ground albedo, single scattering albedo and aerosol distribution over the Huygens descent area. Using these measurements as a baseline we can then perturb the model parameters in a minimalistic but realistic way to match the VIMS observations at other latitudes and longitudes. At first we retain the methane abundance and phase function characteristics and attempt to achieve an acceptable fit by varying only the ground albedo, the single scattering albedo of the particles, and the optical thickness of the haze in each of the 3 layers.

These adjustments were carried out by multiplying the values at the Huygens site by a wavelength independent factor, which, in the case of the single scattering albedo (ω) variations, was applied to its complement ($1-\omega$). The ground albedo was adjusted in order to match the VIMS spectral window regions in the near IR (0.8-1.6 μm) where it is possible to see the surface. The scattering absorption (1 -single scattering albedo) was adjusted so that the model matches the VIMS continuum data at 0.6-0.7 μm where the haze thickness is semi-infinite (optical depth ≈ 5). The optical thickness (τ) was adjusted to match the absorption band observations. Although adjustments in τ in the lower layers (below 80 km) allowed us to closer match the medium depth absorption bands, in general the data could be modeled within error adjusting only the optical depth above 80 km.

To determine the variability of Titan's haze and methane with longitude, we studied several spectra at different longitudes for two latitudes. We compared the data at the Huygens landing site (figure 6.6) to other VIMS data at roughly the same latitude, but 20° further west in longitude (figure 6.11). The same atmospheric parameters fit the spectra at both sites with only a change in ground albedo necessary (increased by a factor of 2). The second test case is presented in figure 6.12. We fit two sets of VIMS data near the equator, but separated in longitude by 130° . Again, only a change to the ground albedo (increased by 70%) is necessary to fit the data at both longitudes.

The variability of Titan's haze with latitude, assuming a constant methane, was determined from the spectra contained in selections 1-3. We find that good fits were possible by varying only 1) the ground albedo, 2) the single scattering albedo of the particles above 80 km, and 3) the haze thickness above 80 km. It was not necessary to vary phase func-

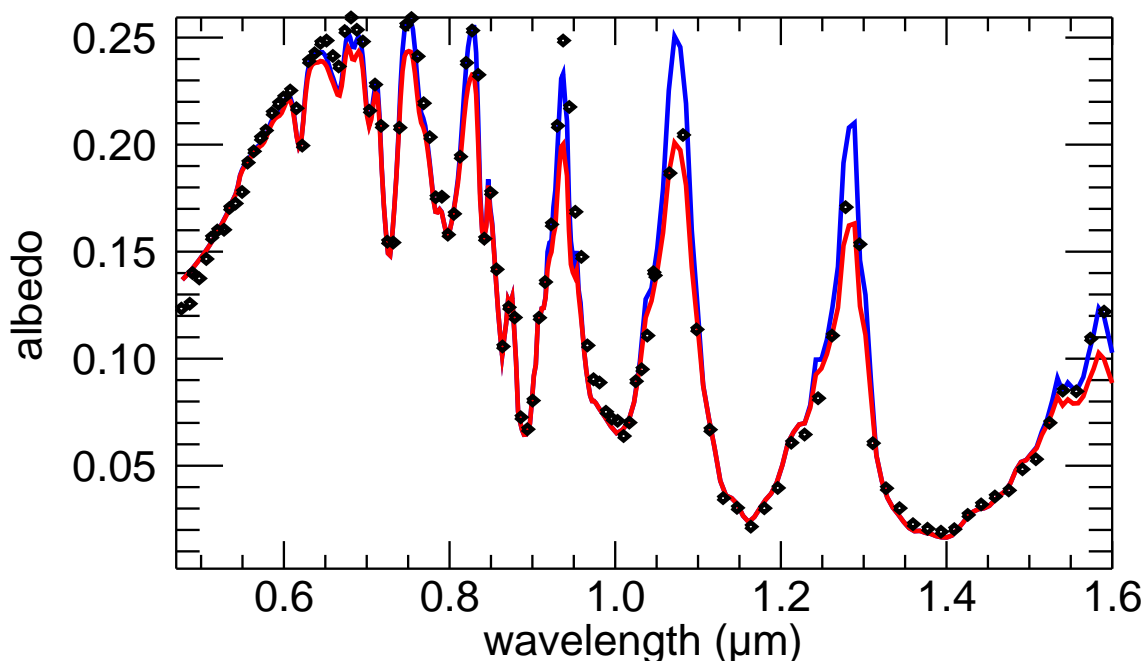


Figure 6.11 Comparison of the VIMS observations recorded at 11°S and 200°W , near the Huygens Landing Site, with the DISR model for two values of ground albedo. In this case a doubling of the ground albedo was necessary for the DISR model to match the VIMS data. The black diamonds are the VIMS data, the red line is the DISR model at the landing site, and the blue line is the DISR model with the ground albedo doubled.

tions, or atmospheric properties below 80 km. Figure 6.13 shows the fits of the DISR model to the VIMS data for selected locations on Titan. The multiplicative factors which produced the best fits are presented in figure 6.14.

With a constant methane abundance we can fit the latitudinal variations in the spectra by changing the surface brightness and the optical depth and single scattering albedo of the haze above 80 km (figure 6.14). The single scattering absorption ($1-\omega$) above 80 km increases almost linearly by 20% from 60°S to 40°N latitude. The haze thickness above 80 km is constant north of $\sim 10^{\circ}\text{S}$; it is also constant south of 20°S latitude, but at about 60% of the northern value. A transition in the haze thickness occurs between $\sim 10^{\circ}\text{S}$ - 20°S latitude, near the sub-solar latitude. Our study suggests that Titan's north-south brightness asymmetry results primarily from variations in the thickness of Titan's haze above 80 km.

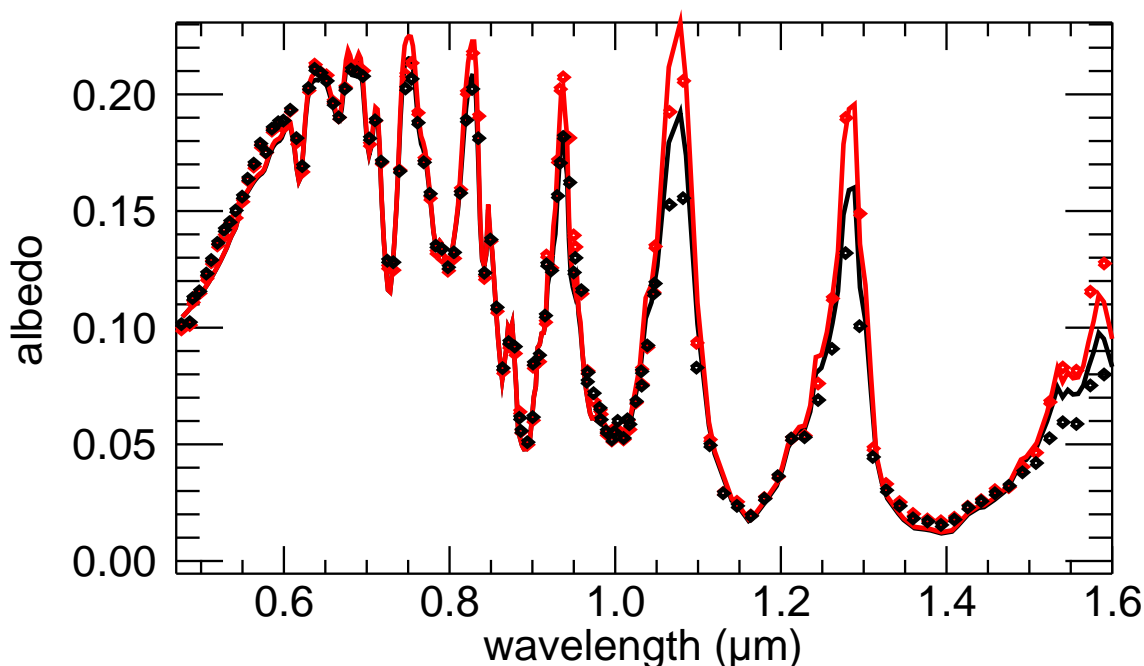


Figure 6.12 Comparison of the VIMS observations of Titan near the equator with the DISR model at two diverse longitudes. The black diamonds show the VIMS data near 0° longitude, and the red diamonds show the VIMS data at 130°W . Notice the close agreement, except in the continuum. The black line shows the DISR model of the data at 0°W ($f_{\text{gr}}=1.15$) and the red line shows the fit at 130°W with the same atmospheric parameters, but increasing the ground albedo by 48%. (to $f_{\text{gr}}=1.7$) in order to match the continuum data in the red.

6.5 Methane and haze variation coupling

The analysis above demonstrates that Titan's spectra can be interpreted with a constant methane abundance, but does not exclude the possibility of methane variability, with a correspondingly smaller haze variation. To investigate the change in the haze optical depth south of 20°S , which differs from that sampled by Huygens at 10°S latitude, we modeled a representative spectrum at 27°S . Using the doubling and adding calculation, we varied the methane abundance, and derived the haze optical depth and single scattering albedo that best matched the data. The resultant model spectra reproduced the observations well for methane abundances 0.3-2.0 times those measured at the Huygens landing

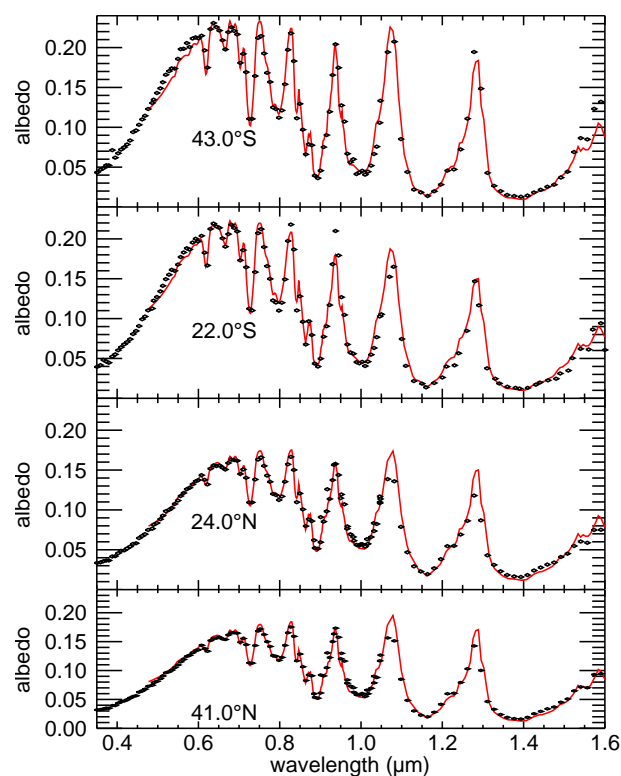


Figure 6.13 VIMS spectra (diamonds) and models assuming no methane variation (lines), for selected locations on Titan, from top to bottom: 43°S , 22°S , 24°N , 41°N . The shallower methane bands towards the north can be fit entirely with haze changes, though the ambiguity between haze optical depth and methane abundance allows other fits to the same spectra, with variable methane.

site (figure 6.15). Thus we find that a family of solutions for the methane abundance and the optical depth and single scattering albedo of the haze above 80 km that fit the data (figure 6.15).

6.6 Analysis of 10,988 spectra

To evaluate whether all the spectral variations observed by VIMS for the chosen lighting conditions of sample 4 can be explained by the methane and haze variations derived from the smaller samples discussed above, we analyze all the spectra in selection 4. We first derive one combination of the possible haze and methane variations that fit the data. This

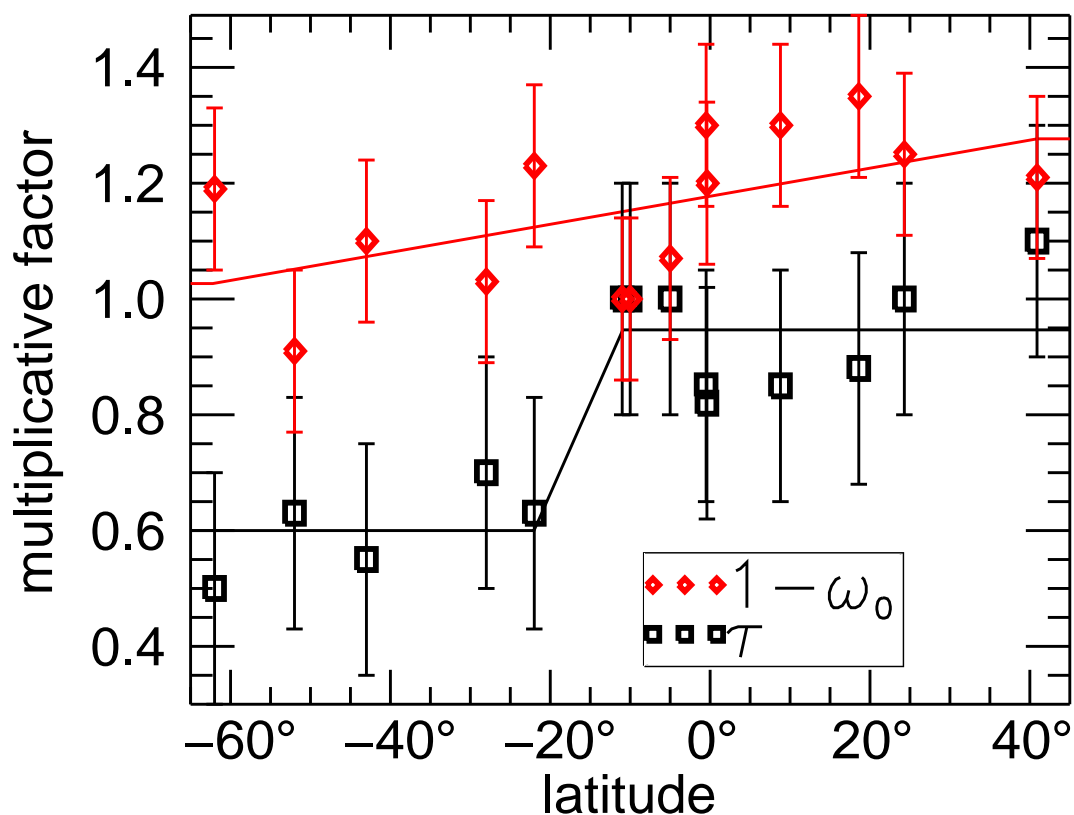


Figure 6.14 Variation in the optical depth (black) and single scattering albedo factors (red) that reproduced the spectra in selections 1-3, assuming no variation in the methane abundance.

solution is stabilized with a dampening that biases the parameters towards the smallest change from their values at the Huygens site. We concentrate on the region of the $0.61 \mu\text{m}$ band, which is most sensitive to methane variations in the upper troposphere (20-50 km altitude, figure 6.19). Models were calculated in a 3D grid defined by the 3 variable parameters, and a fit obtained from the model that best matches the 3 spectral indicators defined below. Our standard model varies the methane abundance by a multiplicative factor that is 1 below 20 km, changes linearly to the selected value between 20 and 30 km, and remains constant above 30 km. Methane variations outside 20-50 km do not strongly affect the results. A profile with a multiplicative factor 1.5 has an additional

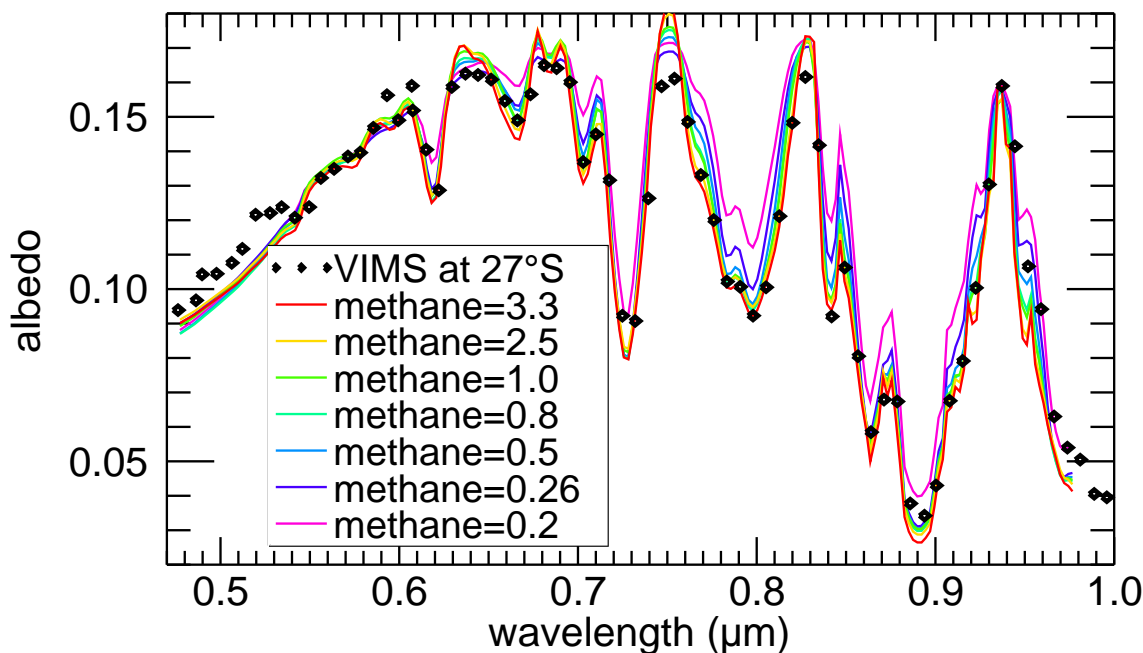


Figure 6.15 VIMS spectrum of a bright terrain at 27°S, 343°W (diamonds) compared to model spectra calculated for methane profiles equal to that measured at the Huygens landing site multiplied by a factor shown in the legend. For each model the haze and surface albedo were adjusted to fit the observation, resulting in the parameters shown in figure 6.16. Note that models with methane factors of 0.2, 0.26, 2.5 and 3.3 do not match the observations.

$0.18_{-0.09}^{+0.05}$ km-am of methane ($6_{-3}^{+2}\%$ of the GCMS methane column abundance), relative to a profile with a 1.0 factor.

This analysis was automated with the use of average albedos (for the data and models alike) at specific wavelength regions, referred to as indicators. The 3 wavelength regions are 0.6076-0.6294 μm (a_1 , in the methane band), 0.6349-0.6370 μm (a_2 , continuum next to the band), and 0.7230-0.7260 μm (a_3 , a methane band of higher optical depth), shown in figure 6.7. The first indicator is a relative 0.61 μm band depth, defined as $\frac{a_2 - a_1}{a_2}$. The second indicator is an average continuum level, a_2 , and the third is the average at 0.72 μm , a_3 . Figure 6.17 shows the latitudinal distribution of these 3 indicators for all the 10988 spectra in the sample, and their averages on 10° latitude bins, along with the averages

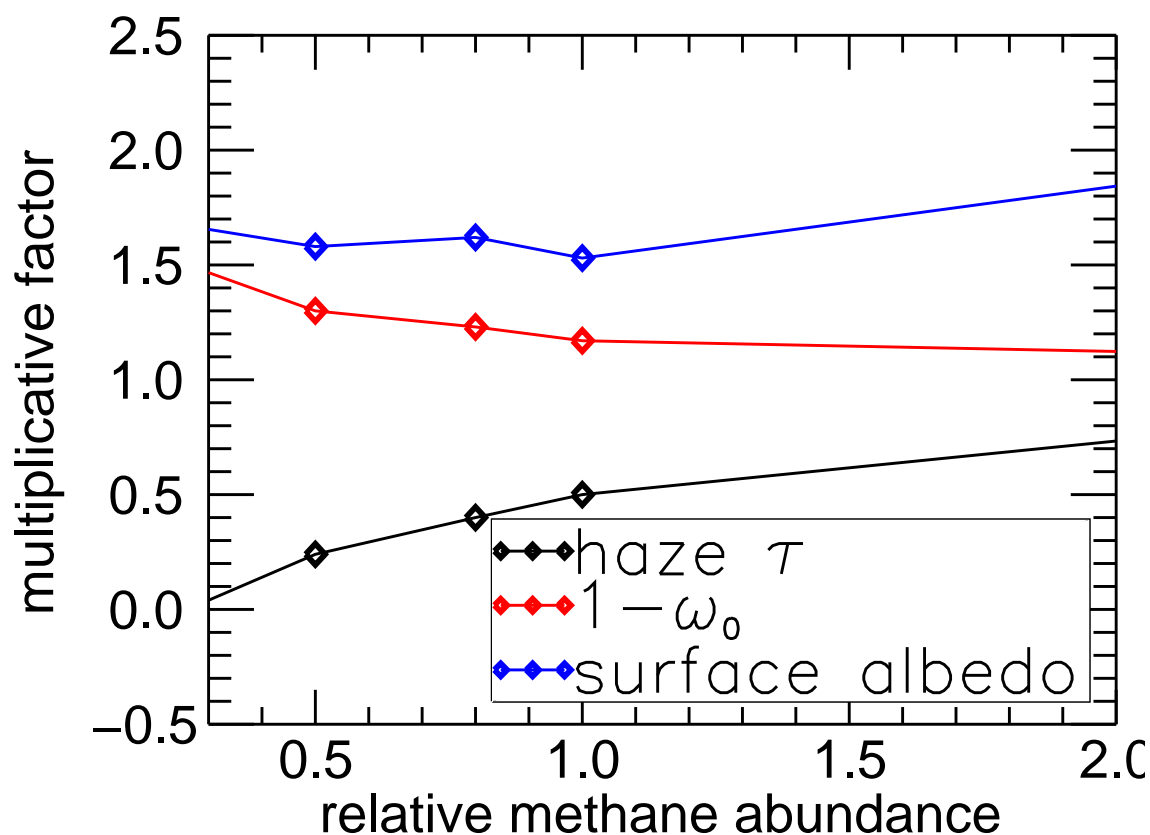


Figure 6.16 The 3 parameters found to fit to the spectrum shown in figure 6.15, depending on the methane abundance assumed. Methane factors less than 0.3 and greater than 2 do not fit the spectra (figure 6.15).

from the best fit models. Besides methane absorption, the relative band depths are affected by the variable haze scattering, which is constrained from the measurements of the continuum level and the $0.72 \mu\text{m}$ methane band. The sensitivities of the 3 indicators with respect to variations in methane abundance and haze density and opacity above 80 km are indicated in figure 6.18. The typical variation in the band from models with different methane abundances and data observed at different latitudes is exemplified in figures 6.7 and 6.18.

We interpret the data by changing 3 parameters: two haze parameters and one parameter for the methane abundance. The two haze parameters are identical to those used in

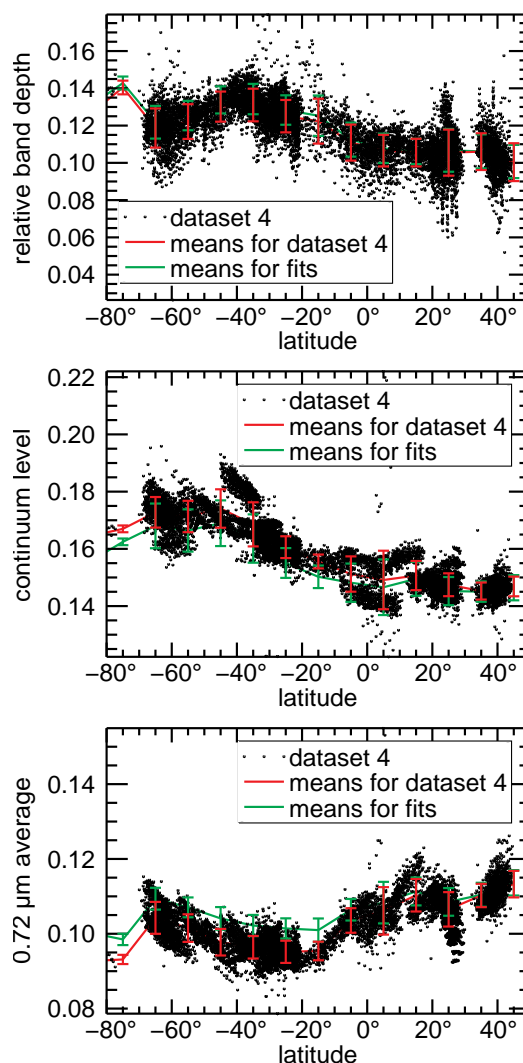


Figure 6.17 The latitudinal distribution of the 3 indicators used to measure the data and spectra. Black points: indicators for every spectrum of selection 4. Red lines: 10° latitude averages of the indicators for all spectra in dataset 4. The errors are defined by the standard deviation among the indicator values in each latitude bin. Green lines: 10° latitude averages of the indicators for the best fit models for all spectra in dataset 4. The errors are defined by the standard deviation of the derived indicators. The indicators for the fit of each of the 10988 spectra are not plotted because of their near exact match for band depth and continuum level, as indicated by the small difference between the red and green lines.

the doubling and adding analysis discussed above; they are multiplicative factors for the optical depth and the single scattering absorption above 80 km. We find that variations in

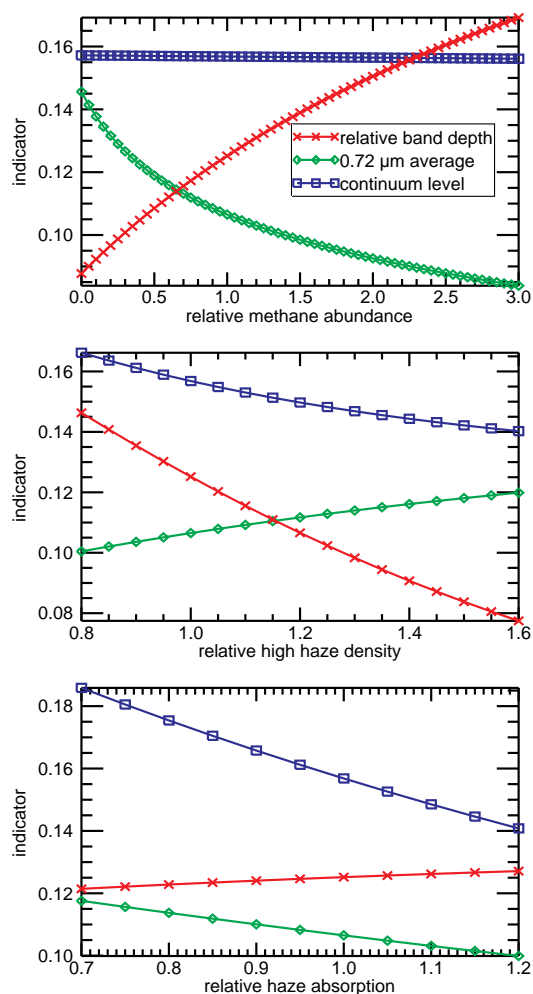


Figure 6.18 Sensitivity of each of the 3 model indicators used to measure data and model spectra, relative to variations on each of the 3 model parameters used for the fits. Top figure: methane abundance variations by a vertically uniform multiplicative factor. Middle figure: changes in haze density by a constant multiplicative factor above 80 km. Bottom figure: changes in the single scattering absorption ($1 - \text{single scattering albedo}$) by a constant multiplicative factor above 80 km. As shown in the top figure, the continuum region selected is nearly insensitive to methane variations, with the relative band depth at $0.61 \mu\text{m}$ being the most sensitive measure of the methane.

the haze solely below 80 km do not simultaneously reproduce the amplitude of the variations in the $0.6 \mu\text{m}$ continuum and the $0.61 \mu\text{m}$ band. Such low altitude haze changes, while they strongly affect the methane band, are not indicated in the latitudinal and longi-

tudinal spectral variations. These considerations suggest that the haze above 80 km is the predominant factor that causes spectral variations in the continuum and strong methane bands. While haze variations below 80 km may simultaneously occur to a lesser extent, we do not consider such changes here.

Variations in methane at 20-30 km altitude can result from temperature variations, which change the saturation pressure. We quantify this possibility by alternatively using methane vertical profiles determined by their relative humidity. These profiles start with the methane at 45% relative humidity at the surface (after Niemann et al. (2005)). The mixing ratio is kept constant until the altitude where saturation is reached, above which a 100% saturation mixing ratio is kept up to the tropopause. We apply a temperature difference that is null below altitude 20 km, rises linearly from 20 to 30 km, and remains constant above 30 km.

At every latitude the observed spread in the model indicators exceeds the difference between the observations and its fits. At all latitudes the spread in the measured indicators is not correlated with longitude. The difference between data and model indicators has a standard deviation of 1.6%, 2.0% and 3%, for the relative band depth, continuum level and 0.72 μm band average, respectively. The larger deviation in the 0.72 μm band results from the higher weight in the fits given to the 0.6 μm region, since it is the most sensitive to the tropospheric methane.

The derivation of the haze and methane variations forms one example of the family of solutions derived from the more limited spectra (sections 6.4 and 6.5). The results of the extended data set agree with those of the smaller data set, with a couple of exceptions. Two separate populations of points appear south 40°S in the continuum indicator (middle panel, figure 6.17). We hypothesize that this division in points results from optically thick clouds, which are common at high southern latitudes. These clouds often reach the top of the troposphere (40 km altitude, Griffith et al. (2005a)) and obscure the methane below, which would cause a drop in the inferred methane at those latitudes. There is also a less pronounced double population of points at 10°S-10°N, whose origin is unknown, since clouds were typically absent at this region.

For this model we derive an increase in haze density above 80 km of $20_{-15}^{+5}\%$ between

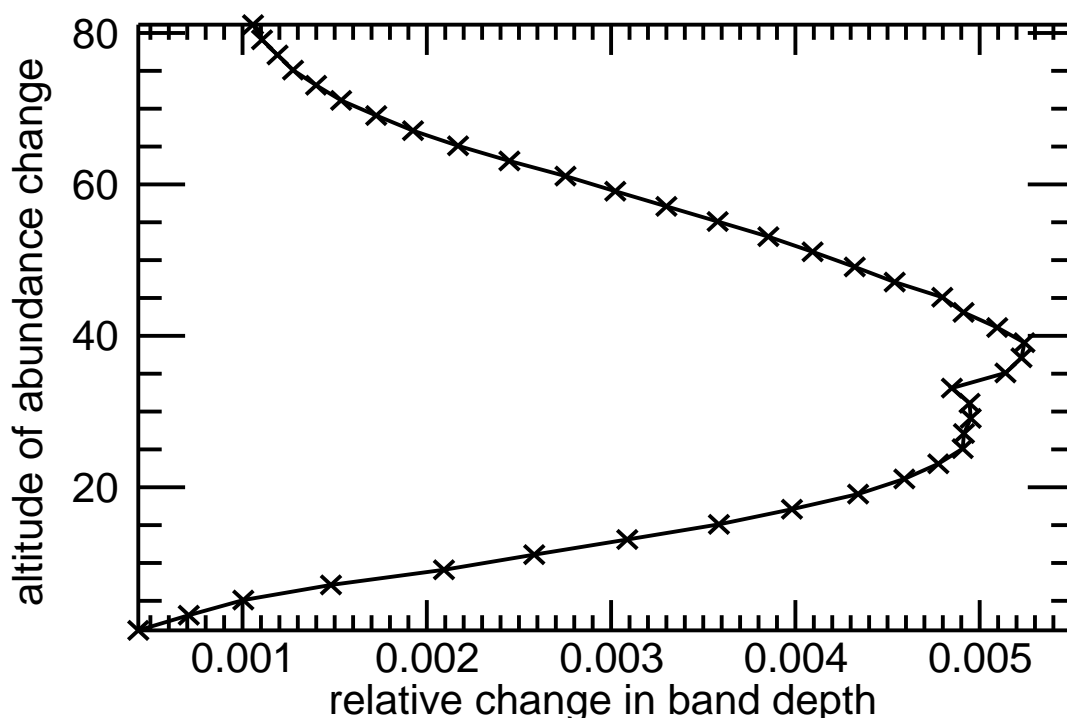


Figure 6.19 The variation of the relative $0.61 \mu\text{m}$ band depth, as a function of the altitude where the methane abundance is changed, indicates the altitude region probed by the methane band. The abundance is changed only in a 2 km region centered at the indicated altitudes. In that region, the abundance varies by a multiplicative factor that is a linear function of altitude, varying from a value of 2 at the indicated altitude, to a value of 1 (no change) 1 km above or below the selected altitude.

35°S and 5°S , and a single scattering absorption increase by $18 \pm 8\%$ over 45°S - 15°N (figure 6.21). The methane abundance variation, the largest allowable by the data, is a decrease of $50_{-25}^{+15}\%$ between 25°S to 35°N latitudes (figure 6.22). Here, the errors indicate the spread of I/F values in the data. The observed methane variation is compatible with a $1.5_{-1.0}^{+1.3}$ K drop in temperature above 20 km between 25°S - 35°N latitudes. Another member of the family of possible solutions was also examined with the extended data set: that with a constant latitudinal methane abundance. We find that the extended data indicate haze parameters consistent with those derived previously (figure 6.20). We find that the VIMS dataset agrees with several exemplar solutions, and indicates no additional

effects except the occasional occurrence of methane clouds. In addition, the variations are not correlated with longitude, indicating that any upper tropospheric and stratospheric methane changes correlate with latitude only.

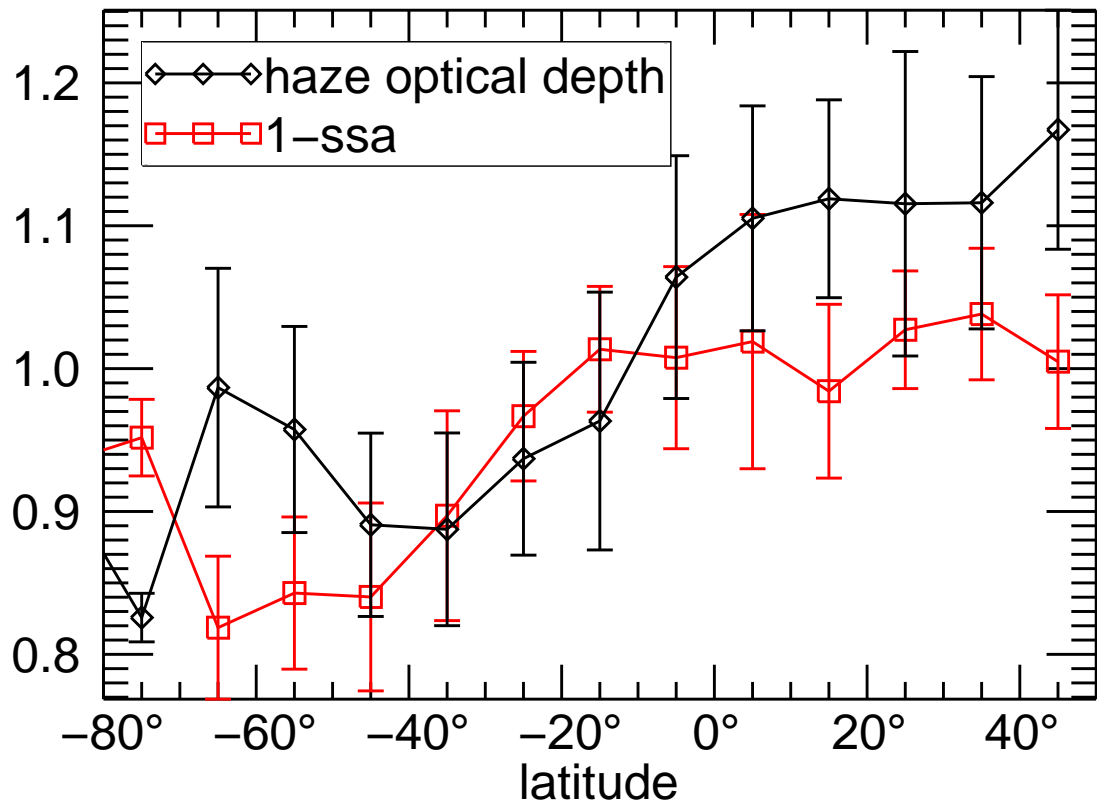


Figure 6.20 Parameters that fit the spectra in selection 4 for the model that assumes a constant methane abundance. Error bars indicate the standard deviation of parameters in each latitude bin, and result primarily from the measured variations of the spectral signatures at each latitude. The latitudinal variations derived by discrete ordinates analysis of spectra from selection 4 agree with those derived by doubling and adding analysis of spectra from selections 1-3.

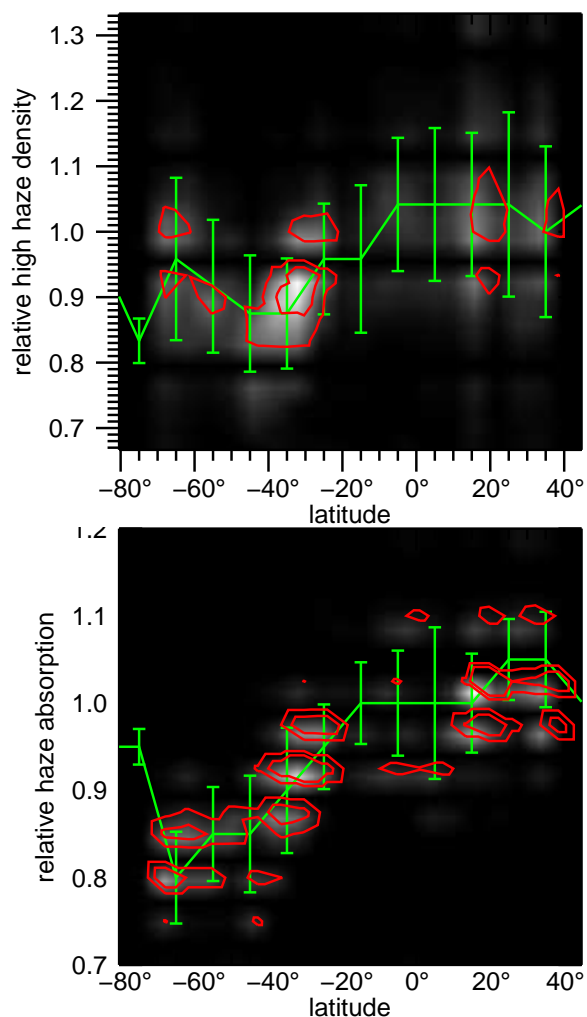


Figure 6.21 The distribution of the 2 haze model parameters that fit each spectrum in selection 4 in our exemplar solution. The distributions of the model parameter governing the methane abundance are shown in figure 6.22. Background grayscale image: 2D histogram of the distribution of the measured parameters. Red lines: contour levels of the 2D histograms, at levels 100 and 200. Green lines: averages of the model parameters found for all spectra on each 10° latitude bin. The error bars are defined by the standard deviation among the indicators of the model spectra in each bin, and result predominantly from the effect of the spectral variation at each latitude.

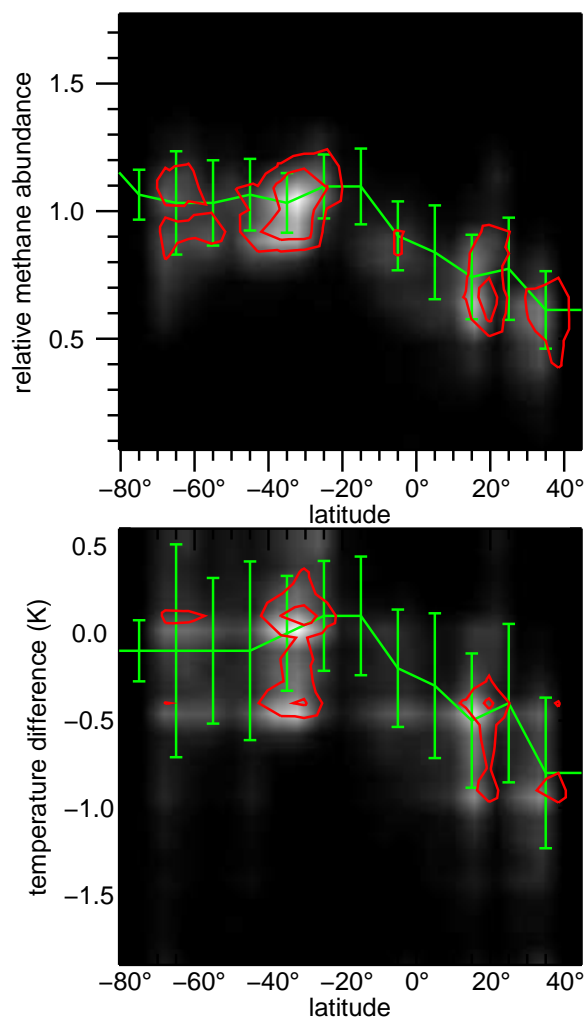


Figure 6.22 The distributions for the 2 alternative model parameters used to vary the methane abundance, shown in the same way as the parameters for the haze (figure 6.21). These results derive from the same model that produced the haze characteristics in figure 6.21. The methane abundance distribution was derived by applying a multiplicative factor to the GCMS methane profile above 20 km (top), or by applying a temperature difference to the HASI profile above 20 km (bottom).

6.7 Heating rate

Titan's haze absorbs 40% of the incoming solar radiation (McKay et al., 1991), thereby affecting the radiative forcing of the atmosphere. The latitudinal variations in the haze therefore affect the atmospheric heating of each hemisphere. To evaluate this effect, we

calculate the heating rate of the current season for our model which has a uniform latitudinal methane abundance. We find, fortunately, that the haze variations have a limited effect. Instead, the solar heating rate at each latitude is controlled mostly by the local solar zenith angle. As shown in figure 1 of Tomasko et al. (2008b), the heating above 80 km results from the visible absorption of the haze aerosols rather than by methane gas. Changes in the thickness and absorptive properties in the haze cause the heating to shift only slightly to higher or lower altitudes. At deeper levels, the single-scattering albedo of the haze aerosols is higher, and the absorption by methane gas has a larger relative contribution. At the lowest levels, the wings of the methane bands become optically thick, and their absorption dominates the solar heating. Since none of our families of solutions changes the methane mixing ratio at deep levels (consistent with the high resolution observations of chapter 4) the solar heating at these levels does not vary.

We compute the net solar flux of sunlight integrated over the passband from 0.3 to 3.0 μm . We average the flux over a Titan day for a range of latitudes, assuming a subsolar latitude of 22.54°S (that of 14 January 2005, the day Huygens landed on Titan). We calculate the difference in the net solar flux at each altitude, which when divided by the heat capacity of the gas, provides the solar heating rate. The results, shown in figure 6.23 and in table 6.2, minus the thermal infrared cooling rates when they become available, will yield the net heating or cooling rates for the current season.

As expected, the solar heating rates vary over several orders of magnitude with altitude due to the differing penetration of sunlight and even more by the greater heat capacity of the denser gas at low altitudes. Figure 6.23 shows the heating rate at 30°S and 10°S, two latitudes straddling the sub-solar point, with therefore similar insolutions. The small 10-15% difference in the heating rates below 150 km results from the different haze optical depths associated with the NSA. We find therefore that although the haze optical depth above 80 km altitude varies significantly in this uniform methane model, the solar heating rates are quite similar.

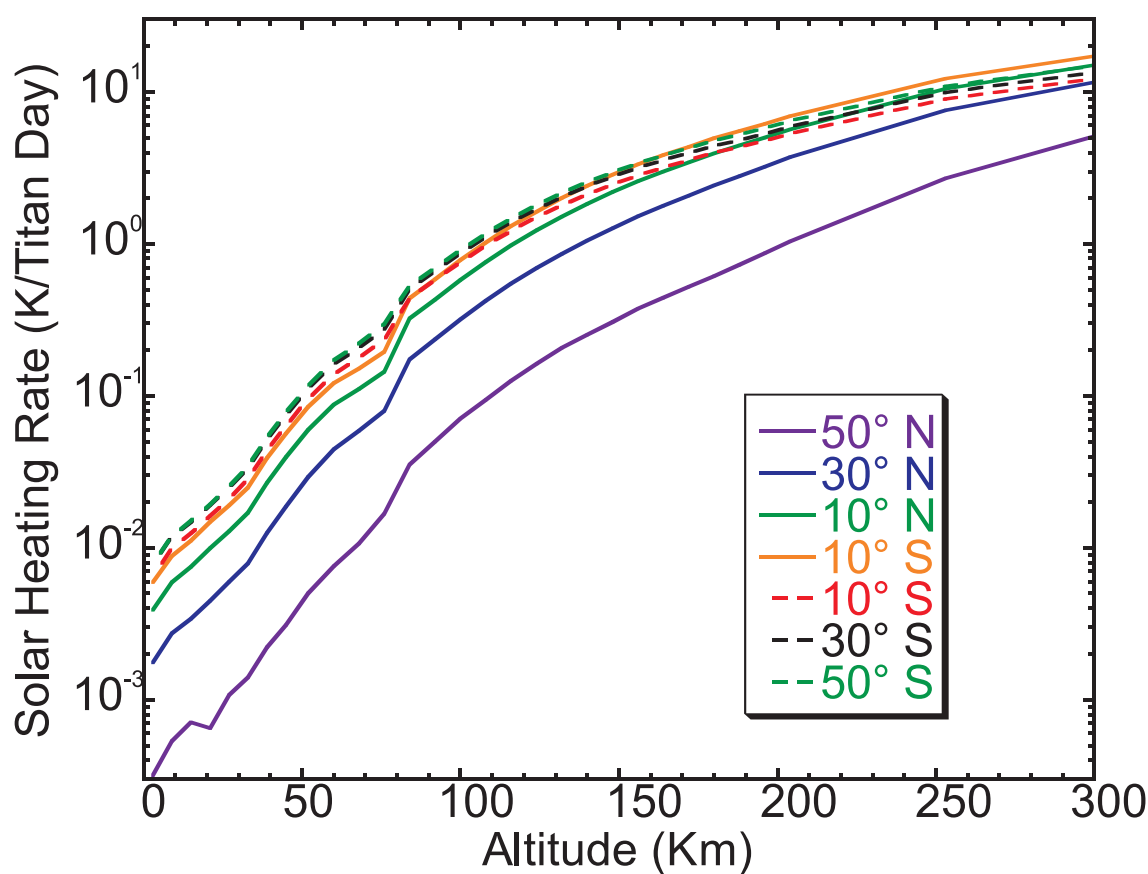


Figure 6.23 Solar heating rates as a function of latitude calculated for sub-solar latitude of 22.54°S , which occurred on 14 Jan 2005. We adopt a constant methane with latitude and the corresponding derived haze abundances (figure 6.14). The heating rates at 10°S are calculated for haze thicknesses characterizing the northern and southern hemispheres to indicate the effect of the NSA.

Table 6.2 Solar heating rate (K/Titan day).

Altitude (km)	50°N	30°N	10°N	10°S (from N)	10°S (from S)	30°S	50°S
351	10.22	18.41	22.33	25.00	17.14	18.76	21.17
253	2.70	7.57	10.45	12.27	8.99	9.91	10.93
204	1.034	3.721	5.657	6.910	5.327	5.910	6.442
196	0.867	3.220	4.996	6.147	4.779	5.314	5.778
188	0.726	2.801	4.439	5.521	4.347	4.837	5.236
180	0.615	2.430	3.942	4.942	3.975	4.435	4.786
172	0.524	2.084	3.430	4.339	3.563	3.978	4.288
164	0.444	1.786	3.001	3.839	3.176	3.558	3.819
156	0.376	1.521	2.590	3.336	2.822	3.172	3.395
148	0.306	1.267	2.188	2.852	2.470	2.777	2.960
140	0.254	1.058	1.840	2.413	2.119	2.397	2.555
132	0.208	0.860	1.517	2.002	1.804	2.040	2.167
124	0.163	0.695	1.230	1.635	1.501	1.704	1.805
116	0.126	0.547	0.976	1.306	1.220	1.389	1.469
108	0.094	0.422	0.758	1.017	0.972	1.110	1.169
100	0.071	0.318	0.577	0.779	0.754	0.863	0.908
92	0.0501	0.2358	0.4310	0.5845	0.5781	0.6624	0.6938
84	0.0352	0.1736	0.3225	0.4396	0.4398	0.5059	0.5280
76	0.0168	0.0798	0.1448	0.1954	0.2354	0.2752	0.2966
68	0.0107	0.0591	0.1109	0.1514	0.1777	0.2075	0.2216
60	0.0076	0.0445	0.0874	0.1209	0.1387	0.1622	0.1717
52	0.0050	0.0292	0.0598	0.0845	0.0955	0.1121	0.1173
45	0.0031	0.0186	0.0394	0.0566	0.0639	0.0753	0.0781
39	0.0022	0.0125	0.0268	0.0390	0.0440	0.0519	0.0535
33	0.0014	0.0079	0.0170	0.0249	0.0282	0.0334	0.0343
27	0.0011	0.0060	0.0129	0.0190	0.0211	0.0250	0.0256
21	0.0007	0.0045	0.0099	0.0148	0.0162	0.0191	0.0193
15	0.0007	0.0034	0.0075	0.0111	0.0124	0.0148	0.0150
9	0.0005	0.0027	0.0059	0.0088	0.0099	0.0118	0.0120
3	0.0003	0.0018	0.0039	0.0059	0.0065	0.0078	0.0078

CHAPTER 7

CONCLUSIONS

Our analysis indicates that VIMS observations at 0.35-1.6 μm measure the spatial variation of Titan's stratospheric haze and, as a result of the low spectral resolution, the methane abundance variations only in the upper troposphere (figure 6.19). The large altitude range sampled by the visible to near-IR wavelength coverage only in part limits the ambiguity between the methane and haze spectral effects.

The latitudinal haze variation that we have measured for the current epoch has been tracked to change with Titan's season such that the hemisphere with the largest optical depth in the high haze (currently the northern hemisphere) follows winter (Lorenz et al., 2004, 2001, 1999, 1997). Called the north-south asymmetry (NSA), this differential hemispherical haze structure exhibits a characteristic wavelength dependence: the winter hemisphere is found to be darker than the summer hemisphere for wavelengths between 0.34 μm and 0.6 μm , and brighter at wavelengths between ~ 0.61 μm and 0.9 μm (Lorenz et al., 1999). VIMS data indicate that the NSA extends to ~ 2.2 μm , where the northern hemisphere is currently $\sim 38\%$ brighter than the south.

The larger optical depth of Titan's haze in the winter hemisphere indicates a greater number density of haze particles. This density disparity is explained as resulting from the seasonal transport of haze due to the atmosphere's general circulation, which flows roughly from the summer to the winter hemisphere (Hutzell et al., 1996). Lorenz et al. (1999) reproduce the wavelength dependence of the NSA with a simple model that entails the transport of dark particulates. This transport of dark particles predicts the 15% brightness ratio that VIMS measures currently at 480-500 nm (figures 7.1, 7.2 and 7.3). Consistent with Lorenz *et al.*'s model, we find that the current NSA can be explained by a difference in the population of particles above 80 km, which, according to DISR measurements, are indeed slightly darker than the haze particles below 80 km (Tomasko et al., 2008c). Our constant methane model explains moreover the measured wavelength depen-

dence of the NSA as shown in figure 7.2. This study thus supports Lorenz's hypothesis that the transport of dark particles causes the NSA. Moreover, VIMS data suggest that the transport of the DISR-detected dark particles above 80 km, in particular, causes the NSA. A picture emerges that the NSA is due to the fact that visible and near-IR observations sample altitudes of roughly ~ 50 -100 km (figure 6.1) that straddle the 80 km boundary between two haze layers that differ in scattering properties (Tomasko et al., 2008c). At visible wavelengths, methane absorption is weak and the addition of slightly darker particles above 80 km is sufficient to darken Titan's winter hemisphere, since less light is reflected back from the underlying brighter particles. At near-IR wavelengths, the NSA is observed within the strong methane bands. Here the extra dark particles increase the scattering such that more light is scattered from Titan's atmosphere rather than absorbed by methane. The winter hemisphere thus appears bright (figure 7.4). These combined effects are possible because the single scattering albedo (SSA) from 0.5 to 1.6 μm of the haze above 80 km (SSA=0.90-0.96) and below 80 km (SSA=0.95-1.00) does not differ substantially, and yet nonetheless incurs a significant effect because multiple scattering is involved (figure 6.10).

We find that between 27°S and 19°N latitude, a constant methane abundance, as well as one that decreases by 60% towards the north, is allowed by the data. At 70°S-27°S, and 19°N-45°N, spectral variations with latitude are of similar amplitude as those at a constant latitude, and thus indicate no measurable methane variation. The lowest altitudes probed, those at 20-30 km by the 0.61 μm band, occur where the atmospheric methane at the landing site is saturated (Tokano et al., 2006). Thus any methane variations in these altitudes likely derive from slight temperature variations. A 1.5 K tropopause temperature drop is enough to decrease the methane abundance by 50%. The methane variation that we measure is consistent therefore with a 0-2 K drop in the tropopause temperature between 25°S and 35°N latitude.

The global methane abundance retrieved with the CH₃D 3v₂ band, $4.2^{+1.3}_{-0.9}$ km-am ($4.9^{+1.5}_{-1.0}\%$ of the total column abundance), is higher than that measured by Huygens GCMS at 10°S, 2.94 km-am (3.4% of the total). The spatial variation of this band is most sensitive to the methane variation at the low troposphere (below 20 km al-

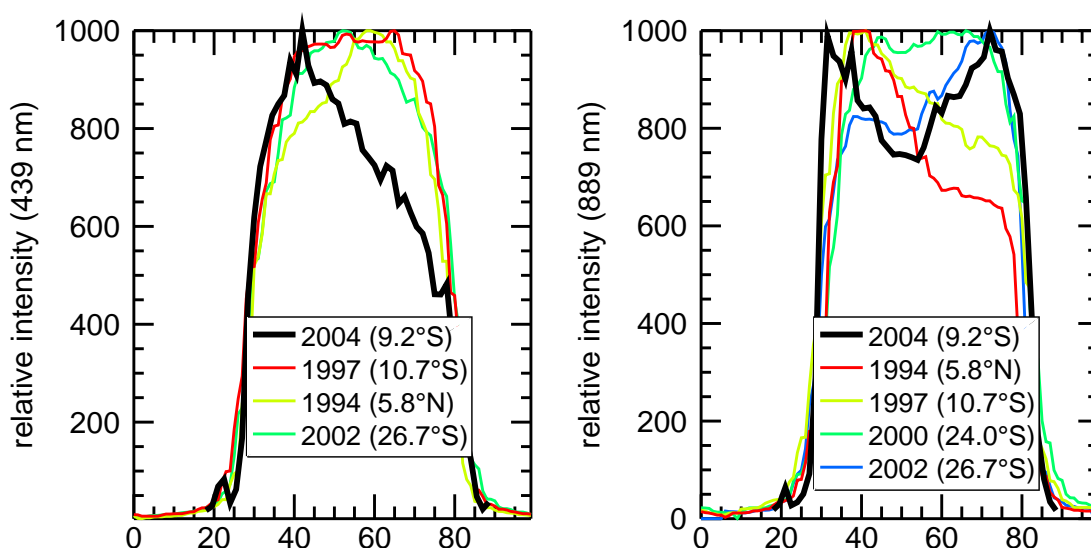


Figure 7.1 Profiles along the central meridian of Titan's disk indicate the temporal evolution of the north-south haze asymmetry, in the blue continuum (439 nm, left) and the middle of a saturated near-IR methane band (889 nm, right). Each profile has south on the left side, and covers a different range in latitude, centered at the values given in the labels. The profile for 2004 was obtained from the VIMS cube shown in figure 6.8, while the others are from the HST observations of Lorenz et al. (2004) (figure 2).

titude), and is thus complementary to the VIMS observations. No changes to within 20% were found in the low altitude methane between 32°S-32°N latitudes. We did not detect any local increase in methane that would indicate outgassing, yet we sampled, for lack of time, only a small fraction of Titan's disk. We have not yet investigated the humidity at high latitudes, where seasonal swings in insolation are sufficient to fuel large humidity changes (Griffith et al., 2008), and where lakes exist as a source of atmospheric methane.

Both the VIMS and Keck observations of the upper and lower tropopause, respectively, are consistent with a constant methane latitudinal profile from 32°S and 32°N. A constant methane abundance in the tropical lower atmosphere is consistent with the atmosphere's thermodynamics, which indicates insufficient seasonal and daily variations in insolation to fuel large humidity changes (Griffith et al., 2008). In contrast, the polar atmosphere, not fully sampled here, experiences a summer increase in insolation potentially

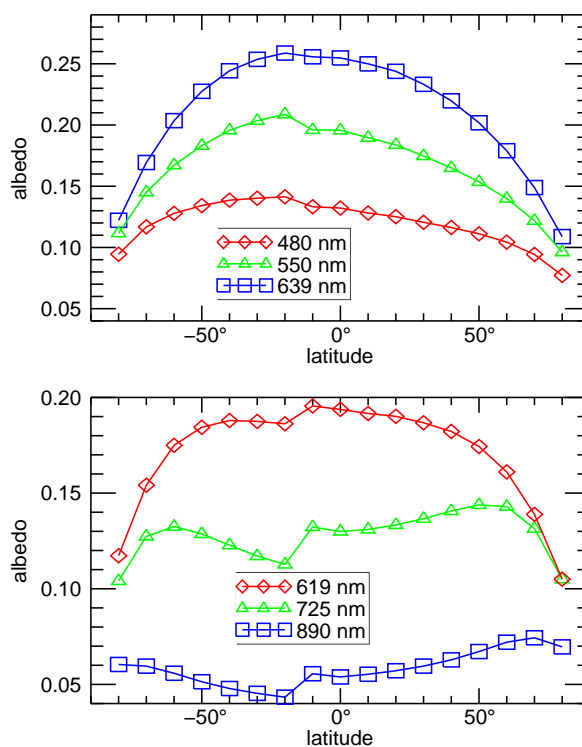


Figure 7.2 Calculations of the I/F at 6 wavelengths indicate that an increase in the slightly darker haze above 80 km altitude causes a reversed effect in the infrared I/F compared to the effect at visible wavelengths. The profiles in the top panel are at continuum wavelengths, those in the bottom are methane band wavelengths. These calculations assume the model that has a constant methane abundance with latitude and the corresponding haze characteristics (figure 6.14).

high enough, depending on the overlying polar cap opacity, to fuel an increase in humidity due to the evaporation of polar lakes (Griffith et al., 2008). High summer humidities, allowed by our data, may thereby fuel summer storms. Observations of the emerging northern pole will address this possibility further.

We find that the atmospheric heating rate at each latitude is affected mainly by the solar incidence angle, rather than the north-south variation in the haze distribution. However, the thick winter polar cloud, not investigated here, may play a large role in establishing the heating rate over the winter pole. Solar heating may cause temperature variations at the tropopause, depending on the circulation and the manifestation of the long radiative

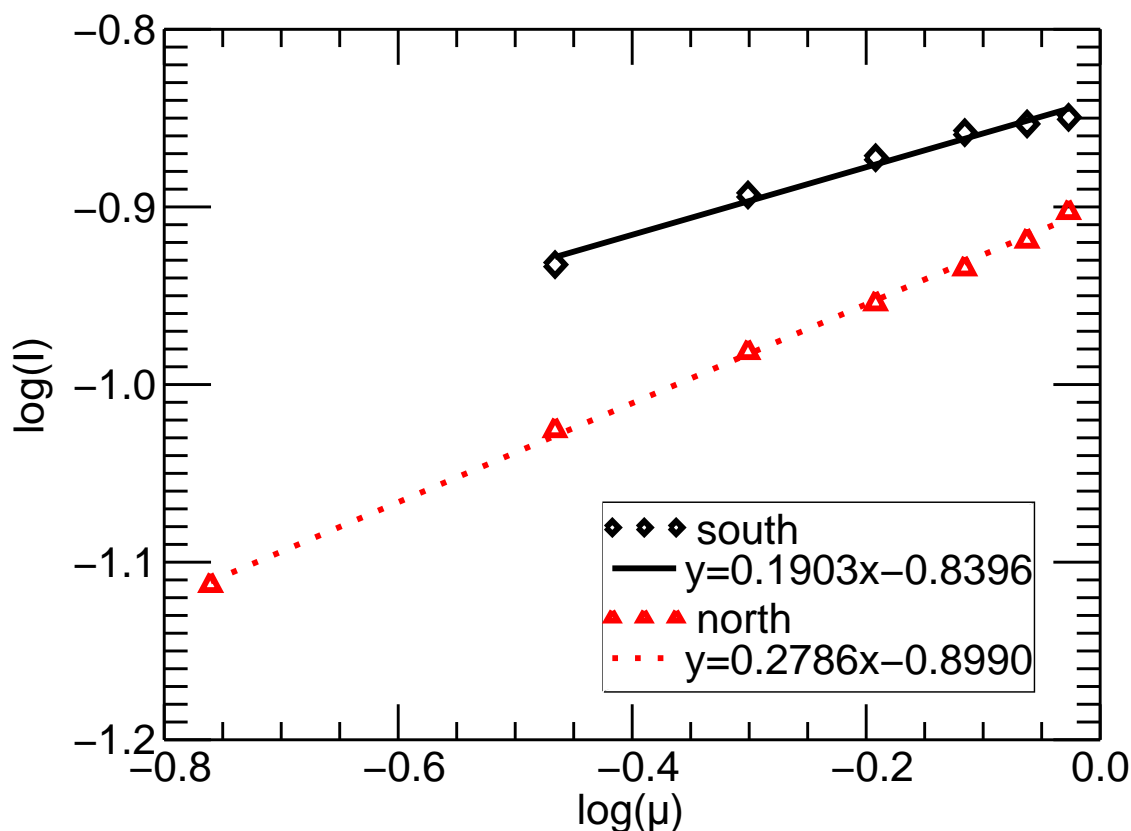


Figure 7.3 Minneart function fits to Titan's limb darkening at 480 nm for the northern and southern hemispheres indicate a 15% difference in the intensities.

time constant of the troposphere, which exceeds a Titan year (Smith et al., 1981). The range of possible methane profiles can be further constrained with temperature measurements. Voyager measured a tropopause temperature increase of 0-1 K between 60°S and 60°N latitude in the northern spring (Courtin and Kim, 2002; Samuelson et al., 1997). Cassini radio occultation measurements, in the process of being analyzed, will more precisely quantify the current latitudinal temperature gradients of Titan's tropopause.

The latitudinal haze and methane variations will be further constrained with an analysis of VIMS limb and occultation observations. These data resolve Titan's vertical opacity structure, thereby indicating which latitudinal changes in the spectra originate in the troposphere and which originate in the stratosphere. Tropospheric changes are more sen-

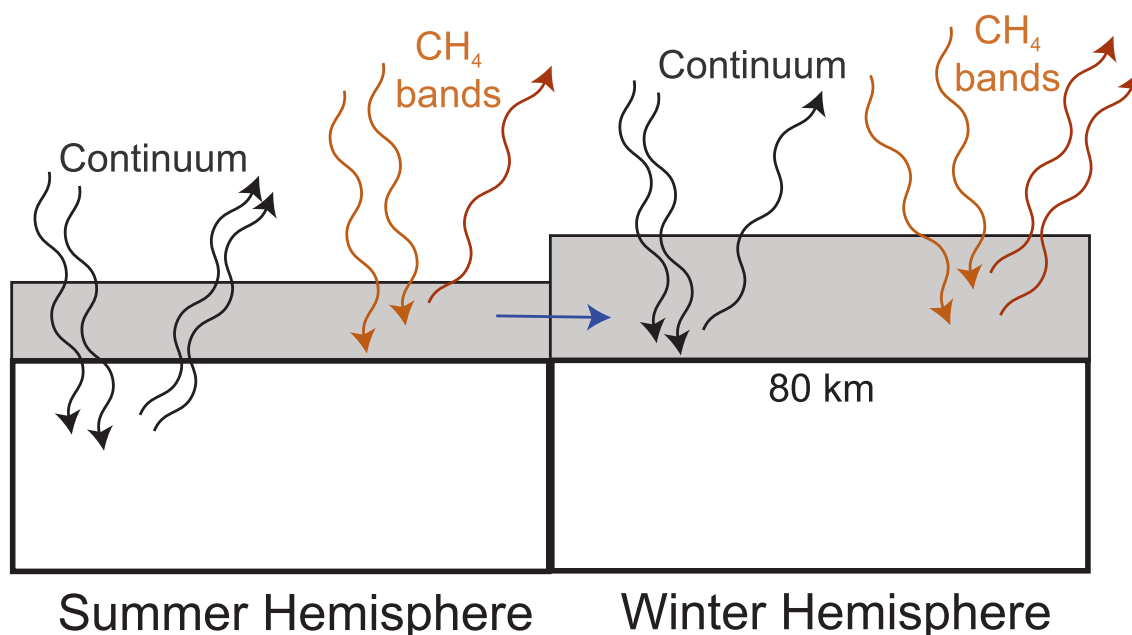


Figure 7.4 Cartoon explanation of the formation of Titan's NSA. Huygens DISR measurements detected a change in the reflective properties of Titan's haze at 80 km altitude; the slightly darker haze above 80 km is represented by the gray boxes, and the brighter haze by the white boxes. Black and red wiggly lines represent sunlight within the strong methane bands (well sampled at near-IR wavelengths) and in the continuum outside the bands, (well sampled at visible wavelengths) respectively. Our calculations indicate that the NSA results from the transport and buildup of the dark haze in the winter hemisphere. At continuum wavelengths, sunlight is reflected from both haze layers, with little methane absorption; an increase in the thickness of the dark haze causes more light to be absorbed, and a decrease in Titan's I/F. Within the methane bands, the addition of the darkish haze decreases the column abundance of methane traversed by the photons, thereby incurring more scattering and a higher I/F.

sitive to the methane abundance, due to its increasing abundance towards lower altitudes, and thus these observations will further constrain the possible methane and haze profiles. Observations similar to these will be conducted through Cassini's extended mission, which is currently planned to cover almost half a Titan year. Similar analyses will constrain the seasonal radiative forcing, haze transport, and methane content of the atmosphere, all of which are needed to understand Titan's circulation and methane cycle.

Future work on the radiative transfer models includes a rewriting of the entire discrete

ordinates code, to make better use of vectorization and parallelization, thus improving its efficiency. The implementation of the linearized singular value decomposition algorithm to fit the spectra will be improved so that it can work from a precalculated set of model spectra. This will free the current SVD code of its main limitation, that is the need to recalculate a large number of model spectra for every observation analysed, and with every change to the fitting parameters. The SVD solutions, which so far could not be extensively calculated due to their high computational cost, will then provide more precise derivations and better constraints on errors and degeneracies. The code revisions will also make it more robust and portable, with a uniform implementation of the atmospheric model, allowing a free choice of the radiative transfer code, with the addition of 2-stream, doubling and adding and raytracing algorithms in a unified code, so that the radiative transfer algorithm can be freely chosen at runtime.

The expansions of titan_browse discussed in chapter 5 will make it more efficient and flexible, allowing the use of all core bands for selections and maps, and direct access the selected spectra. The visualization of VIMS data will also be improved with colormaps calibrated to uniform perceptual distances, including tests with colormap selection systems similar to Pravda (Rogowitz and Treinish, 1998).

APPENDIX A

AVAILABILITY AND USE OF TITAN_BROWSE

titan_browse, and the standard database files produced, are available for VIMS team members. There are 4 standard database file sets produced for each flyby: IR and VIS channel with no extra backplanes, and IR and VIS channel with selected bands where the surface is visible, and with different methane and haze optical depths, which probe different altitudes on Titan's atmosphere. Its use is detailed in its documentation, accessible directly from titan_browse, and copied in Appendix B.

The user interface is shown in figure 5.6. titan_browse organizes the cubes in a tree structure, with flybys at the root level, followed by observation sequences in each flyby, followed by individual cubes in each sequence. This tree is shown in its window on the left side of the interface, and is used for loading and unloading database files for each flyby, and for browsing and selecting individual cubes. Selecting an individual cube shows the cube information in the top text window, and plots the locations of its spatial pixels in the map panel (or an EPS file, if enabled).

The map window on the right side is the same for showing the location of pixels in a selected cube, and the search results. Since spectra from multiple cubes can be selected at one time, the map provides a direct mean of making mosaic maps, which is particularly useful with observations sequences that have many small or very narrow (frequently 1 pixel wide) cubes. The maps can then be used to view the selections, as a plot of the pixel locations, or as a projected image of any real function of the available variables. As an example, figure 5.6 shows the 2050 nm band (internally called bpl(*,11), which is the contents of the pixel function box) of some pixel selection, on a satellite projection, on top of the ISS 2007 base map. This example is the simplest kind of function to show in the map, but any function of the available variables can be used, with the same generality as the criteria for making selections. This tool thus provides an easy way to map complex functions of the spectra. Making multiple maps at the same geometry and exporting them

to EPS or PNG files is also a convenient way to make PDF or GIF (thus vector or bitmap, respectively) movies at a constant geometry, to search for temporal changes.

The maps can be made at variable rectangular, orthographic, stereographic or satellite (perspective) projection, with selectable background images (HST, VIMS and ISS mosaics) and overlays (spacecraft and sun positions, terminator, and the probe site). The EPS output for the map is created with vector elements for all lines and labels drawn, thus avoiding setting a hardware resolution to these elements. These are the maps shown in figures 6.2, 6.3, 6.4, 6.5 Alternatively, bitmaps (PNG) files can be made of all maps, which are sampled at the same resolution as in titan_browse's screen.

Database selections are made filtering through lists of cubes and (spatial) pixels, according to functions of their properties. The principle, both for selecting cubes or pixels, is to start with a large (cube/pixel) list, and apply functions to filter it, leaving only the elements (cubes/pixels) for which the function typed in the respective box evaluates to true. The parameters that can be used for selection are those listed in the "Variable selection" tree at the top, and are different for selecting cubes or pixels. Some available parameters are listed in tables A.1 and A.2 (core bands are not included in the tables). They are divided in keywords and backplanes. Keywords mean mostly (not only) parameters from the cube header, including flyby and sequence names, cube shape, exposure times and subsolar, subspacecraft and specular reflection point locations (SUN, CAS, SPP, respectively). Backplanes mean (for cubes) the range of the values of the usual backplanes in the cube, plus the range of the values of a few selected bands, if there are any selected bands. titan_browse treats those selected bands the same as backplanes, that is why those are generically called extra backplanes, or simply backplanes, in this context. Any IDL logical function of these variables can be constructed, including calling user-defined functions. The selections are filtered by removing all elements (cubes/pixels) for which the given function returns false, thus conferring it great flexibility in search criteria. There is no limitation on how many times the lists can be filtered further. Once a list of cubes is made, all the spatial pixels in it can be selected into a pixel list. From the pixel list, selections can be done of individual pixels by the use of functions in the same way as cube selections are made. Examples of some of the simplest forms for selections are contained

in the documentation, in appendix B. Common useful criteria for selection functions are statistical functions, band ratios or differences, integral transforms, or a user defined function of the bands, which may be an indicator of the presence of a feature of interest, such as absorption/emission by a particular substance, or cloud presence.

FILE	LIGHTC063/geo/CM_1467450252_1_vis.cub
SEQUENCE_ID	S02
OBSERVATION_ID	VIMS_000TI_LIGHTC063_PRIME
SEQUENCE_TITLE	VIMS_000TI_LIGHTC063_PRIME
PRODUCT_ID	1_1467450252.13981
TARGET_NAME	TITAN
TI	000TI
FLYBY	TO
OBSERVATION_T	TI
SEQUENCE_NAME	LIGHTC063
PRIME	PRIME
PATH	LIGHTC063/geo/
CUBE	CM_1467450252_1_vis.cub
START_TIME	2004-184T08:39:57.018Z
STOP_TIME	2004-184T08:46:26.219Z
VALID	1
NVAL	1340
LINES	36
SAMPLES	64
EXPOSURE	10000.000
IR_MODE	H
VIS_MODE	H
CAS_lat	-62.39
CAS_lon	20.65
SUN_lat	-24.10
SUN_lon	-58.98
SPP_lat	-49.76
SPP_lon	-34.39
LATITUDE_min	-39.42223
LATITUDE_max	24.45077
LONGITUDE_min	0.09662
LONGITUDE_max	359.96371
SAMPLE_RESOLUTION_mi	57.80128
SAMPLE_RESOLUTION_ma	396.97714
LINE_RESOLUTION_min	51.28688
LINE_RESOLUTION_max	451.32953
PHASE_ANGLE_min	64.07302
PHASE_ANGLE_max	64.69989
INCIDENCE_ANGLE_min	39.87609
INCIDENCE_ANGLE_max	139.37051
EMISSION_ANGLE_min	23.53728
EMISSION_ANGLE_max	87.56882
NORTH_AZIMUTH_min	179.74498
NORTH_AZIMUTH_max	315.10043
SLANT_DISTANCE_min	NaN
SLANT_DISTANCE_max	NaN

Table A.1 Fields available for cube selection. This list does not include core bands (extra backplanes), which are also available (in variable number) in the built databases. The right column has a sample of the field values for a cube.

cube	CM_1467450252_1_vis.cub
x	11
y	31
LATITUDE	-30.60669
LONGITUDE	357.55905
SAMPLE_RESOLUTION	60.13427
LINE_RESOLUTION	62.43610
PHASE_ANGLE	64.55738
INCIDENCE_ANGLE	54.34979
EMISSION_ANGLE	34.57103
NORTH_AZIMUTH	259.62885
SLANT_DISTANCE	NaN

Table A.2 Fields available for pixel selection. This list does not include core bands (extra backplanes), which are also available (in variable number) in the built databases. The right column has a sample of the field values for a pixel.

APPENDIX B

DOCUMENTATION OF TITAN_BROWSE

This is the documentation accessible from titan_browse's help button, generated in standard IDL format from the comments in the source file titan_browse.pro

NAME:

TITAN_BROWSE

PURPOSE:

Provides a graphical interface to select and display information from the database files made by flyby_db

By default, it will search for database files at ./t*/T*.db.sav.noids, or ./T*.db.sav.noids.

CALLING SEQUENCE:

It can be called simply by

TITAN_BROWSE

Provided there are database files to read in the default search locations.

KEYWORD PARAMETERS:

DBLIST:

An array of database file names to load.

If dblist is not provided, all files matching ./t*/T*.db.sav.noids, or, if none found, all matching ./T*.db.sav.noids are used to make it.

XSIZE, YSIZE:

Change the window size from the default (1600x800). Resizing the window with the mouse has no effect, this is the only way to change it.

MAPPT,CUBEINFOPT,PLISTPT,CLISTPT,OVERPT,DEBUG:

Pointers to the map, cube information text, pixel list, cube list, overlay variable and its coordinates, and to the global structure, respectively.

The global structure pointer target is only updated at program exit or when the corresponding button is used. It contains or points to all the variables that define the state of the program at one time.

MAPIM:

Variable to which the map image is returned at the end (causes xmanager to block the command line).

CUBE_INFO:

Variable to which the cube information is returned at the end (causes xmanager to block the command line).

PIXLIST:

Variable to which the pixel list is returned at the end (causes xmanager to block the command line).

CUBELIST:

Variable to which the cube list is returned at the end (causes xmanager to block the command line).

OVERLAY:

Variable to which the overlay image/pixel locations are returned at the end (causes xmanager to block the command line).

RESTRICTIONS:

All the database files used at one time must have the same type of contents (number and content of extra backplanes, also do not mix IR and VIS

files). The structure of the first file is assumed to be the same for all others.

If many databases are read at the same time, a lot of memory can be used. For T0 to T35 and 11 extra backplanes, some 2.5 GB of memory are used.

At least in some cases (observed on Linux x86-64) there was a much higher use of memory if `titan_browse` is called from a 64-bit IDL session. Starting IDL in 32-bit (with the `-32` switch), if available, avoids this inconvenience.

In the case above, the 2.5 GB were used in 32-bit, which became 3.5 GB in 64-bit.

If a lot of swap space is being used, exiting the program with the Done button can take a very long time due to the recursive pointer freeing. In those cases, it will be quicker to not close `titan_browse`, but to exit IDL directly.

The help button makes use of IDL calling a HTML viewer. The browser IDL calls might not be setup by default.

In some cases, it may be necessary to set the environment variable `IDL_ONLINE_HELP_HTML_BROWSER` to the name (not the path or filename) of the browser for IDL to use. The help shown with that button is just this documentation section, in HTML made by `mk_html_help`, with a png screen capture.

EXAMPLE:

To start `titan_browse` for only the T0 file in the a directory `t0` under the current, and obtain an structure with the pixel list, with window size 1000x700:

```
titan_browse,dblist= './t0/T0.db.sav.noids ',pixellist=pxl,$
xsize=1000,ysize=700
```

The use of the `pixellist` keyword will cause the command line to remain blocked while `titan_browse` runs.

After having a pixel list, with the updating of pixellist enabled, and exiting titan_browse, pxl will contain a structure like:

```
IDL> help,pxl,/structure
** Structure <ldaf858>, 3 tags, length=1583352, data length=1583352,
refs=1:
    PIXFIELDS      STRING      Array[23] -> the names of the contents of
pixfiles, and the 22 (in this case) columns of pixlist
    PIXFILES       STRING      Array[15221] -> the file name where each
pixel in the list came from
    PIXLIST        FLOAT       Array[15221, 22] -> the other columns shown
in the pixel list
```

PROCEDURE:

Once started, titan_browse 's window will contain a flyby tree on the left. This is used for loading and unloading database files for each flyby, and for browsing and selecting individual cubes.

A flyby database is loaded by double clicking its name on the tree. Below the tree there is an indicator showing if the currently selected flyby is loaded or not. The files for every flyby can be loaded/unloaded at once by double clicking the root of the tree. This can take several minutes for large numbers of files, so a confirmation box pops up when the root is double clicked.

Viewing a cube and making maps:

Once one (or more) flyby file is loaded, the cubes in it can be used. Selecting a cube name will replace the contents of the cube information text box. Double clicking a cube name will cause it to be plotted on the map at the right of the window, (OR at the specified EPS file, if any) with the current projection parameters, and will replace whatever cube selection function with one that can be used to select that single cube.

By default the map is made to the window. It can be made to an EPS, by filling the "EPS file name" box. It is necessary to hit enter to have the EPS file name take effect. Any subsequent plots will only be made at

that file, overwriting it with no warning, until the file name in the box is blank (and return is pressed, to update it with the blank).

Only after blanking the EPS file name the window will get updated again. The field EPS resolution factor determines the bitmap resampling factor for the bitmap part of the EPS maps (the lines and text are made as vectors), and therefore, the EPS file size.

The default EPS factor, 80, is a fairly high resolution.

Bitmap maps at the screen resolution can be made (png) by using the "Result to save" droplist below the flyby tree. That droplist can also be used to save a text file with the contents of the cube information, cube list or pixel list box.

All the map parameters are set by the controls below the map window.

Making selections of cubes and pixels by their properties:

The database can be searched at the cube and (spatial) pixel level, with the controls in the middle column of the window.

The principle, both for selecting cubes or pixels, is to start with a large (cube/pixel) list, and apply functions to filter it, leaving only the (cubes/pixels) for which the function typed in the respective box is true. The parameters that can be used for selection are those listed in the "Variable selection" tree at the top, and are different for selecting cubes or pixels.

A selection starts, after one (or more) flyby database is loaded, by filling the (initially empty) cube list with all the cubes of the currently loaded flyby files, with the "Select all loaded" button. Once there are cubes in the list, it can be filtered by typing a logical function in the "Functions for cube selection" box. The function is applied only when enter is pressed in that box.

The variables available for building a logical function for cubes can be browsed in the variable selection tree. They are divided in keywords and backplanes. Keywords mean mostly (not only) parameters from the cube header, including things like flyby and sequence names, cube shape, exposure

times and subsolar, subspacecraft and specular reflection point (SPP) locations. Backplanes mean (for cubes) the range of the values of the usual backplanes in the cube, plus the range of the values of a few selected bands, if there are any selected bands. For titan_browse, those selected bands are the same as backplanes, that is why those are generically called extra backplanes, or simply backplanes, in this context. Extra backplanes have the name of the band wavelength in nm. If the name starts with an "A", it means the backplane is not a single band, but an average of some bands, centered at the given wavelength.

When a variable name is double clicked in the tree, its internal name is typed in the relevant selection function box. The selection is based only on whatever function is in the box. The purpose of the variable tree is simply to know what the internal names of the variables are.

As an example, when titan_browse is started the cube selection function comes filled with

```
(ids.NVAL gt 0)
```

This function, if applied, would select the cubes with >0 valid pixels. It is there to provide a quick way to remove from the list the cubes with no valid pixels in them. For the database files used by titan_browse, a valid pixel is one for which there are valid coordinates in the backplanes of the cube that was used when building the database.

As an example, a selection of cubes in which the cosines of the maximum of the incidence angles are >0.5, and the maximum of the latitudes is >30 (degrees), can be done with the function `(cos(ids.bckrange(5,1)/!radeg) gt 0.5) and (ids.bckrange(0,1) gt 30)`

(the selection tree shows, by double clicking the in the maximum of latitude, that its internal name is `ids.bckrange(0,1)`).

As all the cube selection variables are part of the structure array called `ids` by titan_browse, any IDL logical function of the variable `ids` can be typed for the cube selection. Any cubes for which that function evaluates to true are kept in the current list, the others are removed.

The generality of this means that very complex functions can be used, including user defined functions. Defining a function in a .pro file might be convenient for more complex selections, to avoid typing a long one line function in the box, and serving as a record of how the selection was made. But note that if using your own functions, they are only automatically compiled by IDL the first time they are called in the session, therefore they will not automatically recompile if you edit your function after it.

Another way to do a complex selection is to do it by parts. There is no limitation on how many times the lists can be filtered further.

Once the desired cubes have been selected, a pixel list can be made with the button "Select all in list". This will put in the pixel list every pixel of every cube in the cube list. After there are some pixels in the pixel list, that list can be filtered in the same manner as the cube list, by typing a logical function of the pixel variables in the "Function for pixel selection" box.

Again, the variable tree can be used to type in the box the internal name of the desired pixel variable. For pixel selections, only backplane variables are available. This is because keywords and backplane ranges are constant for every pixel in a cube, so selections based on them must be done at the cube level.

The pixels are selected with their function in the same manner: the function is evaluated, and only the pixels for which it is true are preserved. As an example, to select pixels with latitudes between 0 and -10:

```
(bpl(*,0) gt -10) and (bpl(*,0) lt 0)
```

As double clicking on pixel latitude on the variable tree types `bpl(*,0)` in the function box. All pixel variables are internally a part of the structure `bpl`, so if you define a function in a .pro file to use it in there, it can be made a function of `bpl`, just as for cubes it could be made a function of `ids`. For pixels the internal variable names are always a column of the array `bpl` while for cubes the variables are always scalar parts of `ids`, but each `ids` is an array (each element of `ids` is a cube).

This is because internally the pixel selections are calculated vectorially for each cube at once, and the cube selections are done vectorially for each flyby at once.

After applying some pixel selections, it can happen that no pixels remain in some of the cubes that were used to fill the pixel list.

The cube list is NOT updated automatically to reflect this. To refresh it, so that only the cubes that have pixels in the pixel list are present, the "Select all in pixel list" button must be used. Note that any changes to the cube list, including this kind of update, automatically clears the pixel list.

If a large number of pixels would initially be in the pixel list, just the printing of the text box with the pixel list can consume a lot of time and memory. To avoid this during intermediate steps (for instance, before the pixel list gets filtered to a smaller list which would actually be of interest), there is the "Keep list" button. It enables or disables updating the text in the pixel list box.

The list still exists and can be filtered, as indicated by the number of pixels in it, it just is not printed. After the list gets reduced to a more manageable size, that button can be used to turn on again the filling of the text box.

Plotting pixel lists:

Once there are pixels in the pixel list text box, they can be plotted on the maps. The "plot selection" button will mark on the map the location of all pixels in the pixel list box.

There is another possibility, making use of the other purpose of the pixel selection function box. It can be used to type in a (usually real, not logical) function. Once a function is there (do not hit enter, this would cause the function to be used as a filter to the pixel list), use the button "Use function as map intensity". This will plot on the map the values of that function for all the pixels in the pixel list box (either as an image, or as a contour plot). One purpose of this is a simple way to

make approximate mosaics. Another is to look at the same thing in different cubes while projected to the same geometry, possibly saving the map images to combine them in a multiframe file, to look for temporal variations, for instance.

EPS map frames are usually simple to be combined in this way as pages of a pdf, just as the png bitmaps are easy to make into an animated gif.

The map in the screen capture image below was made plotting the 2050 nm band (the backplane bpl(*,11)) on a satellite projection, on top of the ISS 2007 base map.

MODIFICATION HISTORY:

Written by: Paulo Pentead, 4/2007

Last change to program 20080521 (added latlab and lonlab controls)

Last change to documentation 20080521

Screen capture:

The screenshot shows the titan_browse.pro software interface. The main window displays a satellite map of Earth with a red overlay range. The interface is divided into several panels:

- File Tree (Left):** Shows a hierarchical view of data files, including folders like 'LIGHT063' and 'LIGHT118', and sub-folders for different cubes.
- Selected cube: CH_1467450817_1.ir.cub** (Top Center): A table showing metadata for the selected cube.

Variable	min	max
LATITUDE	-86.31706	25.59491
LONGITUDE	0.02579	399.31024
SAMPLE_RESOLUTION	85.25435	452.52643
LINE_RESOLUTION	150.01125	815.14664
PHASE_ANGLE	54.46206	65.24407
INCIDENCE_ANGLE	14.84073	147.84512
EMISSION_ANGLE	1.11137	89.65764
NORTH_AZIMUTH	0.02559	399.52448
SUNT_DISTANCE	338676.45790	342110.07000
1573NH	-0.00026	0.14006
1602NH	-0.00029	0.10367
2050NH	-0.00035	0.12572
2150NH	-0.00073	0.02539
2162NH	-0.00093	0.02990
2159NH	-0.00080	0.01454
2223NH	-0.00037	0.01223
2712NH	-0.00075	0.07028
2823NH	-0.00088	0.06404
- Function for cube selection:** (ids.cube eq 'CH_1467450817_1.ir.cub')
- Cubes in list:** 1 (Clear list, Select all loaded, Select all in pixel list)
- Table:**

	FILE	SEQUENCE_ID	OBSERVATION
	LIGHT063/geo/CH_1467450817_1.ir.cub	502	VHNS_00011_LIGHT063_PSI
- Function for pixel selection:** bpl(*,11)
- Pixels in list:** 1366 (Clear list, Select all in list, Use function as map intensity, Keep list)
- Table:**

cube	x	y	LATITUDE	LONGITUDE	SAMPLE_RESOLUTION	LINE_RESOLUTION
CH_1467450817_1.ir.cub	1	15	-0.16872	31.39535	225.51089	348
CH_1467450817_1.ir.cub	1	16	-7.85095	31.46359	175.57045	261
CH_1467450817_1.ir.cub	1	17	-13.82849	32.54812	156.87726	206
CH_1467450817_1.ir.cub	1	18	-17.30427	34.22342	146.41809	206
CH_1467450817_1.ir.cub	1	19	-22.33842	35.85243	137.84334	131
CH_1467450817_1.ir.cub	1	20	-28.28133	37.78951	132.57862	181
CH_1467450817_1.ir.cub	1	21	-29.52723	40.77607	133.84993	171
CH_1467450817_1.ir.cub	1	22	-32.28907	43.76579	129.73966	161
- Plot cube:** (ids.cube eq 'CH_1467450817_1.ir.cub')
- Map projection:** satellite
- Background map:** 4:ISS 2007
- Selection plot title:**
- Selection contour levels:**
- Selection overlay range:** min: [], max: [], auto: [x]
- EPS map file:**
- Map label interval:**
- Overlay:** Image [x], EPS resolution factor [30.0000]
- Map resolution factor:** [30.0000]
- Map grid:** [x]
- Map label interval:** []
- rotation:**

(See titan_browse.pro)

REFERENCES

- Acton, C. H. (1999). SPICE Products Available to the Planetary Science Community. In *Lunar and Planetary Institute Science Conference Abstracts*, volume 30 of *Lunar and Planetary Inst. Technical Report*, pp. 1233–+.
- Backhaus, W. G., R. Kliegl, and J. S. Werner (eds.) (1998). *Color Vision*. Walter de Gruyter. ISBN 3110154315.
- Barnes, J. W., R. H. Brown, E. P. Turtle, A. S. McEwen, R. D. Lorenz, M. Janssen, E. L. Schaller, M. E. Brown, B. J. Buratti, C. Sotin, C. Griffith, R. Clark, J. Perry, S. Fussner, J. Barbara, R. West, C. Elachi, A. H. Bouchez, H. G. Roe, K. H. Baines, G. Bellucci, J.-P. Bibring, F. Capaccioni, P. Cerroni, M. Combes, A. Coradini, D. P. Cruikshank, P. Drossart, V. Formisano, R. Jaumann, Y. Langevin, D. L. Matson, T. B. McCord, P. D. Nicholson, and B. Sicardy (2005). A 5-Micron-Bright Spot on Titan: Evidence for Surface Diversity. *Science*, **310**, pp. 92–95. doi:10.1126/science.1117075.
- Bellucci, G., V. Formisano, E. D’Aversa, R. H. Brown, K. H. Baines, J. P. Bibring, B. J. Buratti, F. Capaccioni, P. Cerroni, R. N. Clark, A. Coradini, D. P. Cruikshank, P. Drossart, R. Jaumann, Y. Langevin, D. L. Matson, T. B. McCord, V. Mennella, R. M. Nelson, P. D. Nicholson, B. Sicardy, C. Sotin, M. C. Chamberlain, G. Hansen, K. Hibbits, M. Showalter, and G. Filacchione (2004). Principal components analysis of Jupiter VIMS spectra. *Advances in Space Research*, **34**, pp. 1640–1646. doi: 10.1016/j.asr.2003.05.062.
- Bergman, L., B. Rogowitz, and L. Treinish (1995). A rule-based tool for assisting colormap selection. *Visualization, 1995. Visualization '95. Proceedings., IEEE Conference on*, pp. 118–125, 444. doi:10.1109/VISUAL.1995.480803.
- Bouchez, A. H. and M. E. Brown (2005). Statistics of Titan’s South Polar Tropospheric Clouds. *ApJ*, **618**, pp. L53–L56. doi:10.1086/427693.
- Boussin, C., B. L. Lutz, C. de Bergh, and A. Hamdouni (1998). Line intensities and self-broadening coefficients for the $3\nu_2$ band of monodeuterated methane. *Journal of Quantitative Spectroscopy and Radiative Transfer*, **60**, pp. 501–514. doi:10.1016/S0022-4073(97)00246-X.
- Boussin, C., B. L. Lutz, A. Hamdounia, and C. de Bergh (1999). Pressure broadening and shift coefficients for H_2 , He and N_2 in the $3\nu_2$ band of $^{12}\text{CH}_3\text{D}$ retrieved by a multispectrum fitting technique. *Journal of Quantitative Spectroscopy and Radiative Transfer*, **63**, pp. 49–84. doi:10.1016/S0022-4073(98)00134-4.

- Brown, M. E., A. H. Bouchez, and C. A. Griffith (2002). Direct detection of variable tropospheric clouds near Titan's south pole. *Nature*, **420**, pp. 795–797.
- Brown, M. E., E. L. Schaller, H. G. Roe, C. Chen, J. Roberts, R. H. Brown, K. H. Baines, and R. N. Clark (2009). Discovery of lake-effect clouds on Titan. *Geophys. Res. Lett.*, **36**, pp. 1103–+. doi:10.1029/2008GL035964.
- Brown, R. H., K. H. Baines, G. Bellucci, B. J. Buratti, F. Capaccioni, P. Cerroni, R. N. Clark, A. Coradini, D. P. Cruikshank, P. Drossart, V. Formisano, R. Jaumann, Y. Langevin, D. L. Matson, T. B. McCord, V. Mennella, R. M. Nelson, P. D. Nicholson, B. Sicardy, C. Sotin, N. Baugh, C. A. Griffith, G. B. Hansen, C. A. Hibbitts, T. W. Momary, and M. R. Showalter (2006). Observations in the Saturn system during approach and orbital insertion, with Cassini's visual and infrared mapping spectrometer (VIMS). *A&A*, **446**, pp. 707–716. doi:10.1051/0004-6361:20053054.
- Brown, R. H., L. A. Soderblom, J. M. Soderblom, R. N. Clark, R. Jaumann, J. W. Barnes, C. Sotin, B. Buratti, K. H. Baines, and P. D. Nicholson (2008). The identification of liquid ethane in Titan's Ontario Lacus. *Nature*, **454**, pp. 607–610. doi:10.1038/nature07100.
- Courtin, R., D. Gautier, and C. P. McKay (1995). Titan's thermal emission spectrum: Reanalysis of the Voyager infrared measurements. *Icarus*, **114**, pp. 144–162. doi:10.1006/icar.1995.1050.
- Courtin, R. and S. J. Kim (2002). Mapping of Titan's tropopause and surface temperatures from Voyager IRIS spectra. *Planet. Space Sci.*, **50**, pp. 309–321.
- Coustenis, A. and B. Bezard (1995). Titan's atmosphere from Voyager infrared observations. 4: Latitudinal variations of temperature and composition. *Icarus*, **115**, pp. 126–140. doi:10.1006/icar.1995.1084.
- Coustenis, A., B. Bezard, and D. Gautier (1989). Titan's atmosphere from Voyager infrared observations. II - The CH₃D abundance and D/H ratio from the 900-1200/cm spectral region. *Icarus*, **82**, pp. 67–80. doi:10.1016/0019-1035(89)90024-9.
- Coustenis, A., A. Salama, B. Schulz, S. Ott, E. Lellouch, T. H. Encrenaz, D. Gautier, and H. Feuchtgruber (2003). Titan's atmosphere from ISO mid-infrared spectroscopy. *Icarus*, **161**, pp. 383–403. doi:10.1016/S0019-1035(02)00028-3.
- de Bergh, C., J. Chauville, B. L. Lutz, T. Owen, and J. Brault (1986). Monodeuterated methane in the outer solar system. II - Its detection on Uranus at 1.6 microns. *ApJ*, **311**, pp. 501–510. doi:10.1086/164790.
- de Bergh, C., B. L. Lutz, T. Owen, and J. Chauville (1988). Monodeuterated methane in the outer solar system. III - Its abundance of Titan. *ApJ*, **329**, pp. 951–955. doi:10.1086/166439.

- Elachi, C., S. Wall, M. Allison, Y. Anderson, R. Boehmer, P. Callahan, P. Encrenaz, E. Flamini, G. Franceschetti, Y. Gim, G. Hamilton, S. Hensley, M. Janssen, W. Johnson, K. Kelleher, R. Kirk, R. Lopes, R. Lorenz, J. Lunine, D. Muhleman, S. Ostro, F. Paganelli, G. Picardi, F. Posa, L. Roth, R. Seu, S. Shaffer, L. Soderblom, B. Stiles, E. Stofan, S. Vetrella, R. West, C. Wood, L. Wye, and H. Zebker (2005). Cassini Radar Views the Surface of Titan. *Science*, **308**, pp. 970–974. doi:10.1126/science.1109919.
- Fink, U. and H. P. Larson (1979). The infrared spectra of Uranus, Neptune, and Titan from 0.8 to 2.5 microns. *ApJ*, **233**, pp. 1021–1040. doi:10.1086/157466.
- Flasar, F. M. (1998). The composition of Titans atmosphere : a meteorological perspective. *Planet. Space Sci.*, **46**, pp. 1109–1124.
- Flasar, F. M., R. K. Achterberg, B. J. Conrath, P. J. Gierasch, V. G. Kunde, C. A. Nixon, G. L. Bjoraker, D. E. Jennings, P. N. Romani, A. A. Simon-Miller, B. Bézard, A. Coustenis, P. G. J. Irwin, N. A. Teanby, J. Brasunas, J. C. Pearl, M. E. Segura, R. C. Carlson, A. Mamoutkine, P. J. Schinder, A. Barucci, R. Courtin, T. Fouchet, D. Gautier, E. Lellouch, A. Marten, R. Prangé, S. Vinatier, D. F. Strobel, S. B. Calcutt, P. L. Read, F. W. Taylor, N. Bowles, R. E. Samuelson, G. S. Orton, L. J. Spilker, T. C. Owen, J. R. Spencer, M. R. Showalter, C. Ferrari, M. M. Abbas, F. Raulin, S. Edgington, P. Ade, and E. H. Wishnow (2005). Titan's Atmospheric Temperatures, Winds, and Composition. *Science*, **308**, pp. 975–978. doi:10.1126/science.1111150.
- Fouchet, T. and E. Lellouch (2000). Vapor Pressure Isotope Fractionation Effects in Planetary Atmospheres: Application to Deuterium. *Icarus*, **144**, pp. 114–123. doi:10.1006/icar.1999.6264.
- Gendron, E., A. Coustenis, P. Drossart, M. Combes, M. Hirtzig, F. Lacombe, D. Rouan, C. Collin, S. Pau, A.-M. Lagrange, D. Mouillet, P. Rabou, T. Fusco, and G. Zins (2004). VLT/NACO adaptive optics imaging of Titan. *A&A*, **417**, pp. L21–L24. doi:10.1051/0004-6361:20040027.
- Gibbard, S. G., B. Macintosh, D. Gavel, C. E. Max, I. de Pater, H. G. Roe, A. M. Ghez, E. F. Young, and C. P. McKay (2004). Speckle imaging of Titan at 2 microns: surface albedo, haze optical depth, and tropospheric clouds 1996-1998. *Icarus*, **169**, pp. 429–439. doi:10.1016/j.icarus.2003.12.026.
- Gillett, F. C. (1975). Further observations of the 8-13 micron spectrum of Titan. *ApJ*, **201**, pp. L41–L43. doi:10.1086/181937.
- Greene, T. P., A. T. Tokunaga, D. W. Toomey, and J. B. Carr (1993). CSHELL: a high spectral resolution 1-5 um cryogenic echelle spectrograph for the IRTF. In Fowler, A. M. (ed.) *Society of Photo-Optical Instrumentation Engineers (SPIE) Conference Series*, volume 1946 of *Society of Photo-Optical Instrumentation Engineers (SPIE) Conference Series*, pp. 313–324.

- Griffith, C. A., J. L. Hall, and T. R. Geballe (2000). Detection of Daily Clouds on Titan. *Science*, **290**, pp. 509–513. doi:10.1126/science.290.5491.509.
- Griffith, C. A., C. P. McKay, and F. Ferri (2008). Titan's Tropical Storms in an Evolving Atmosphere. *ApJ*, **687**, pp. L41–L44. doi:10.1086/593117.
- Griffith, C. A., T. Owen, G. A. Miller, and T. Geballe (1998). Transient clouds in Titan's lower atmosphere. *Nature*, **395**, pp. 575–578. doi:10.1038/26920.
- Griffith, C. A., P. Penteado, K. Baines, P. Drossart, J. Barnes, G. Bellucci, J. Bibring, R. Brown, B. Buratti, F. Capaccioni, P. Cerroni, R. Clark, M. Combes, A. Coradini, D. Cruikshank, V. Formisano, R. Jaumann, Y. Langevin, D. Matson, T. McCord, V. Mennella, R. Nelson, P. Nicholson, B. Sicardy, C. Sotin, L. A. Soderblom, and R. Kursinski (2005a). The Evolution of Titan's Mid-Latitude Clouds. *Science*, **310**, pp. 474–477. doi:10.1126/science.1117702.
- Griffith, C. A., P. Penteado, T. K. Greathouse, H. G. Roe, and R. V. Yelle (2005b). Observations of Titan's Mesosphere. *ApJ*, **629**, pp. L57–L60. doi:10.1086/444533.
- Griffith, C. A., P. Penteado, P. Rannou, R. Brown, V. Boudon, and K. H. Baines (2006). Evidence for Ethane Clouds on Titan. In *Bulletin of the American Astronomical Society*, volume 38 of *Bulletin of the American Astronomical Society*, pp. 544–+.
- Hirtzig, M., A. Coustenis, O. Lai, E. Emsellem, A. Pecontal-Rousset, P. Rannou, A. Negrão, and B. Schmitt (2005). Near-infrared study of Titan's resolved disk in spectro-imaging with CFHT/OASIS. *Planet. Space Sci.*, **53**, pp. 535–556. doi:10.1016/j.pss.2004.08.006.
- Hutzell, W. T., C. P. McKay, O. B. Toon, and F. Hourdin (1996). Simulations of Titan's Brightness by a Two-Dimensional Haze Model. *Icarus*, **119**, pp. 112–129. doi:10.1006/icar.1996.0005.
- Karkoschka, E. (1998). Methane, Ammonia, and Temperature Measurements of the Jovian Planets and Titan from CCD-Spectrophotometry. *Icarus*, **133**, pp. 134–146. doi:10.1006/icar.1998.5913.
- Keller, H. U., B. Grieger, M. Küppers, S. E. Schröder, Y. V. Skorov, and M. G. Tomasko (2008). The properties of Titan's surface at the Huygens landing site from DISR observations. *Planet. Space Sci.*, **56**, pp. 728–752. doi:10.1016/j.pss.2007.11.020.
- Kim, S. J. and J. Caldwell (1982). The abundance of CH₃D in the atmosphere of Titan, derived from 8- to 14-micron thermal emission. *Icarus*, **52**, pp. 473–482. doi:10.1016/0019-1035(82)90007-0.

- Lacy, J. H., M. J. Richter, T. K. Greathouse, D. T. Jaffe, and Q. Zhu (2002). TEXES: A Sensitive High-Resolution Grating Spectrograph for the Mid-Infrared. *PASP*, **114**, pp. 153–168. doi:10.1086/338730.
- Lellouch, E., A. Coustenis, D. Gautier, F. Raulin, N. Dubouloz, and C. Frere (1989). Titan's atmosphere and hypothesized ocean - A reanalysis of the Voyager 1 radio-occultation and IRIS 7.7-micron data. *Icarus*, **79**, pp. 328–349. doi:10.1016/0019-1035(89)90081-X.
- Lellouch, E., A. Coustenis, J.-P. Maillard, K. Strong, N. Deme, C. Griffith, and B. Schmitt (1992). The spectrum of Titan in the 1.06 and 1.28 micron windows. In Kaldeich, B. (ed.) *Symposium on Titan*, volume 338 of *ESA Special Publication*, pp. 353–358.
- Lemmon, M. T., P. H. Smith, and R. D. Lorenz (2002). Methane Abundance on Titan, Measured by the Space Telescope Imaging Spectrograph. *Icarus*, **160**, pp. 375–385. doi:10.1006/icar.2002.6979.
- Lopes, R. M. C., K. L. Mitchell, E. R. Stofan, J. I. Lunine, R. Lorenz, F. Paganelli, R. L. Kirk, C. A. Wood, S. D. Wall, L. E. Robshaw, A. D. Fortes, C. D. Neish, J. Radebaugh, E. Reffet, S. J. Ostro, C. Elachi, M. D. Allison, Y. Anderson, R. Boehmer, G. Boubin, P. Callahan, P. Encrenaz, E. Flamini, G. Francescetti, Y. Gim, G. Hamilton, S. Hensley, M. A. Janssen, W. T. K. Johnson, K. Kelleher, D. O. Muhleman, G. Ori, R. Orosei, G. Picardi, F. Posa, L. E. Roth, R. Seu, S. Shaffer, L. A. Soderblom, B. Stiles, S. Vetrilla, R. D. West, L. Wye, and H. A. Zebker (2007). Cryovolcanic features on Titan's surface as revealed by the Cassini Titan Radar Mapper. *Icarus*, **186**, pp. 395–412. doi:10.1016/j.icarus.2006.09.006.
- Lorenz, R. D., M. T. Lemmon, P. H. Smith, and G. W. Lockwood (1999). Seasonal Change on Titan Observed with the Hubble Space Telescope WFPC-2. *Icarus*, **142**, pp. 391–401. doi:10.1006/icar.1999.6225.
- Lorenz, R. D., R. M. Lopes, F. Paganelli, J. I. Lunine, R. L. Kirk, K. L. Mitchell, L. A. Soderblom, E. R. Stofan, G. Ori, M. Myers, H. Miyamoto, J. Radebaugh, B. Stiles, S. D. Wall, and C. A. Wood (2008). Fluvial channels on Titan: Initial Cassini RADAR observations. *Planet. Space Sci.*, **56**, pp. 1132–1144.
- Lorenz, R. D., P. H. Smith, and M. T. Lemmon (2004). Seasonal change in Titan's haze 1992-2002 from Hubble Space Telescope observations. *Geophys. Res. Lett.*, **31**, pp. 10702–+. doi:10.1029/2004GL019864.
- Lorenz, R. D., P. H. Smith, M. T. Lemmon, E. Karkoschka, G. W. Lockwood, and J. Caldwell (1997). Titan's North-South Asymmetry from HST and Voyager Imaging: Comparison with Models and Ground-Based Photometry. *Icarus*, **127**, pp. 173–189. doi:10.1006/icar.1997.5687.

- Lorenz, R. D., E. F. Young, and M. T. Lemmon (2001). Titan's Smile and Collar: HST Observations of Seasonal Change 1994-2000. *Geophys. Res. Lett.*, **28**, pp. 4453–4456. doi:10.1029/2001GL013728.
- Lutz, B. L., C. de Bergh, and J. P. Maillard (1983). Monodeuterated methane in the outer solar system. I Spectroscopic analysis of the bands at 1.55 and 1.95 microns. *ApJ*, **273**, pp. 397–409. doi:10.1086/161378.
- McKay, C. P., A. Coustenis, R. E. Samuelson, M. T. Lemmon, R. D. Lorenz, M. Cabane, P. Rannou, and P. Drossart (2001). Physical properties of the organic aerosols and clouds on Titan. *Planet. Space Sci.*, **49**, pp. 79–99.
- McKay, C. P., J. B. Pollack, and R. Courtin (1991). The greenhouse and antigreenhouse effects on Titan. *Science*, **253**, pp. 1118–1121. doi:10.1126/science.11538492.
- McLean, I. S., E. E. Becklin, D. F. Figer, S. Larson, T. Liu, and J. Graham (1995). NIRSPEC: a near-infrared cross-dispersed echelle spectrograph for the Keck II telescope. In Fowler, A. M. (ed.) *Society of Photo-Optical Instrumentation Engineers (SPIE) Conference Series*, volume 2475 of *Society of Photo-Optical Instrumentation Engineers (SPIE) Conference Series*, pp. 350–358.
- Niemann, H. B., S. K. Atreya, S. J. Bauer, G. R. Carignan, J. E. Demick, R. L. Frost, D. Gautier, J. A. Haberman, D. N. Harpold, D. M. Hunten, G. Israel, J. I. Lunine, W. T. Kasprzak, T. C. Owen, M. Paulkovich, F. Raulin, E. Raaen, and S. H. Way (2005). The abundances of constituents of Titan's atmosphere from the GCMS instrument on the Huygens probe. *Nature*, **438**, pp. 779–784. doi:10.1038/nature04122.
- Orton, G. (1992). Ground-based observations of Titan's thermal spectrum. In Kaldeich, B. (ed.) *Symposium on Titan*, volume 338 of *ESA Special Publication*, pp. 81–85.
- Penteado, P. F., C. A. Griffith, T. K. Greathouse, and C. de Bergh (2005). Measurements of CH₃D and CH₄ in Titan from Infrared Spectroscopy. *ApJ*, **629**, pp. L53–L56. doi:10.1086/444353.
- Porco, C. C., E. Baker, J. Barbara, K. Beurle, A. Brahic, J. A. Burns, S. Charnoz, N. Cooper, D. D. Dawson, A. D. Del Genio, T. Denk, L. Dones, U. Dyudina, M. W. Evans, S. Fussner, B. Giese, K. Grazier, P. Helfenstein, A. P. Ingersoll, R. A. Jacobson, T. V. Johnson, A. McEwen, C. D. Murray, G. Neukum, W. M. Owen, J. Perry, T. Roatsch, J. Spitale, S. Squyres, P. Thomas, M. Tiscareno, E. P. Turtle, A. R. Vasavada, J. Veverka, R. Wagner, and R. West (2005). Imaging of Titan from the Cassini spacecraft. *Nature*, **434**, pp. 159–168. doi:10.1038/nature03436.
- Rannou, P., F. Hourdin, and C. P. McKay (2002). A wind origin for Titan's haze structure. *Nature*, **418**, pp. 853–856.

- Roe, H. G., A. H. Bouchez, C. A. Trujillo, E. L. Schaller, and M. E. Brown (2005a). Discovery of Temperate Latitude Clouds on Titan. *ApJ*, **618**, pp. L49–L52. doi:10.1086/427499.
- Roe, H. G., M. E. Brown, E. L. Schaller, A. H. Bouchez, and C. A. Trujillo (2005b). Geographic Control of Titan's Mid-Latitude Clouds. *Science*, **310**, pp. 477–479. doi:10.1126/science.1116760.
- Roe, H. G., I. de Pater, B. A. Macintosh, and C. P. McKay (2002). Titan's Clouds from Gemini and Keck Adaptive Optics Imaging. *ApJ*, **581**, pp. 1399–1406. doi:10.1086/344403.
- Rogowitz, B. and L. Treinish (1998). Data visualization: the end of the rainbow. *Spectrum, IEEE*, **35**(12), pp. 52–59. ISSN 0018-9235. doi:10.1109/6.736450.
- Rogowitz, B. E., L. A. Treinish, and S. Bryson (1996). How not to lie with visualization. *Comput. Phys.*, **10**(3), pp. 268–273. ISSN 0894-1866.
- Rothman, L. S., A. Barbe, D. C. Benner, L. R. Brown, C. Camy-Peyret, M. R. Carleer, K. Chance, C. Clerbaux, V. Dana, V. M. Devi, A. Fayt, J.-M. Flaud, R. R. Gamache, A. Goldman, D. Jacquemart, K. W. Jucks, W. J. Lafferty, J.-Y. Mandin, S. T. Massie, V. Nemtchinov, D. A. Newnham, A. Perrin, C. P. Rinsland, J. Schroeder, K. M. Smith, M. A. H. Smith, K. Tang, R. A. Toth, J. Vander Auwera, P. Varanasi, and K. Yoshino (2003). The HITRAN molecular spectroscopic database: edition of 2000 including updates through 2001. *Journal of Quantitative Spectroscopy and Radiative Transfer*, **82**, pp. 5–44. doi:10.1016/S0022-4073(03)00146-8.
- Samuelson, R. E. (1983). Radiative equilibrium model of Titan's atmosphere. *Icarus*, **53**, pp. 364–387. doi:10.1016/0019-1035(83)90156-2.
- Samuelson, R. E., N. R. Nath, and A. Borysow (1997). Gaseous abundances and methane supersaturation in Titan's troposphere. *Planet. Space Sci.*, **45**, pp. 959–980.
- Schaller, E. L., M. E. Brown, H. G. Roe, and A. H. Bouchez (2006a). A large cloud outburst at Titan's south pole. *Icarus*, **182**, pp. 224–229. doi:10.1016/j.icarus.2005.12.021.
- Schaller, E. L., M. E. Brown, H. G. Roe, A. H. Bouchez, and C. A. Trujillo (2006b). Dissipation of Titan's south polar clouds. *Icarus*, **184**, pp. 517–523. doi:10.1016/j.icarus.2006.05.025.
- Smith, B. A., L. Soderblom, R. F. Beebe, J. M. Boyce, G. Briggs, A. Bunker, S. A. Collins, C. Hansen, T. V. Johnson, J. L. Mitchell, R. J. Terrile, M. H. Carr, A. F. Cook, J. N. Cuzzi, J. B. Pollack, G. E. Danielson, A. P. Ingersoll, M. E. Davies, G. E. Hunt, H. Masursky, E. M. Shoemaker, D. Morrison, T. Owen, C. Sagan, J. Veverka, R. Strom,

- and V. E. Suomi (1981). Encounter with Saturn - Voyager 1 imaging science results. *Science*, **212**, pp. 163–191. doi:10.1126/science.212.4491.163.
- Soderblom, L. A., M. G. Tomasko, B. A. Archinal, T. L. Becker, M. W. Bushroe, D. A. Cook, L. R. Doose, D. M. Galuszka, T. M. Hare, E. Howington-Kraus, E. Karkoschka, R. L. Kirk, J. I. Lunine, E. A. McFarlane, B. L. Redding, B. Rizk, M. R. Rosiek, C. See, and P. H. Smith (2007). Topography and geomorphology of the Huygens landing site on Titan. *Planet. Space Sci.*, **55**, pp. 2015–2024. doi:10.1016/j.pss.2007.04.015.
- Sotin, C., R. Jaumann, B. J. Buratti, R. H. Brown, R. N. Clark, L. A. Soderblom, K. H. Baines, G. Bellucci, J.-P. Bibring, F. Capaccioni, P. Cerroni, M. Combes, A. Coradini, D. P. Cruikshank, P. Drossart, V. Formisano, Y. Langevin, D. L. Matson, T. B. McCord, R. M. Nelson, P. D. Nicholson, B. Sicardy, S. Lemouelic, S. Rodriguez, K. Stephan, and C. K. Scholz (2005). Release of volatiles from a possible cryovolcano from near-infrared imaging of Titan. *Nature*, **435**, pp. 786–789. doi:10.1038/nature03596.
- Sromovsky, L. A., V. E. Suomi, J. B. Pollack, R. J. Krauss, S. S. Limaye, T. Owen, H. E. Revercomb, and C. Sagan (1981). Implications of Titan's north-south brightness asymmetry. *Nature*, **292**, pp. 698–702. doi:10.1038/292698a0.
- Stamnes, K. and P. Conklin (1984). A new multi-layer discrete ordinate approach to radiative transfer in vertically inhomogeneous atmospheres. *Journal of Quantitative Spectroscopy and Radiative Transfer*, **31**, pp. 273–282. doi:10.1016/0022-4073(84)90031-1.
- Stamnes, K. and H. Dale (1981). A new look at the discrete ordinate method for radiative transfer calculations in anisotropically scattering atmospheres. II. Intensity computations. *Journal of Atmospheric Sciences*, **38**, pp. 2696–2706. doi:10.1175/1520-0469(1981)038.
- Stamnes, K. and R. A. Swanson (1981). A new look at the distance ordinate method for radiative transfer calculations in anisotropically scattering atmospheres. *Journal of Atmospheric Sciences*, **38**, pp. 387–399. doi:10.1175/1520-0469(1981)038.
- Stamnes, K., S.-C. Tsay, K. Jayaweera, and W. Wiscombe (1988). Numerically stable algorithm for discrete-ordinate-method radiative transfer in multiple scattering and emitting layered media. *Appl. Opt.*, **27**, pp. 2502–2509.
- Stofan, E. R., C. Elachi, J. I. Lunine, R. D. Lorenz, B. Stiles, K. L. Mitchell, S. Ostro, L. Soderblom, C. Wood, H. Zebker, S. Wall, M. Janssen, R. Kirk, R. Lopes, F. Paganelli, J. Radebaugh, L. Wye, Y. Anderson, M. Allison, R. Boehmer, P. Callahan, P. Encrenaz, E. Flamini, G. Francescetti, Y. Gim, G. Hamilton, S. Hensley, W. T. K. Johnson, K. Kelleher, D. Muhleman, P. Paillou, G. Picardi, F. Posa, L. Roth, R. Seu, S. Shaffer, S. Vetrella, and R. West (2007). The lakes of Titan. *Nature*, **445**, pp. 61–64. doi:10.1038/nature05438.

- Thomas, E. and K. Stamnes (1999). *Radiative Transfer in the Atmosphere and Ocean*. Atmospheric and Space Science. Cambridge University Press, 1 edition. ISBN 0 521 40124 0.
- Tobie, G., J. I. Lunine, and C. Sotin (2006). Episodic outgassing as the origin of atmospheric methane on Titan. *Nature*, **440**, pp. 61–64. doi:10.1038/nature04497.
- Tokano, T., C. P. McKay, F. M. Neubauer, S. K. Atreya, F. Ferri, M. Fulchignoni, and H. B. Niemann (2006). Methane drizzle on Titan. *Nature*, **442**, pp. 432–435. doi:10.1038/nature04948.
- Tokano, T., F. M. Neubauer, M. Laube, and C. P. McKay (1999). Seasonal variation of Titans atmospheric structures simulated by a general circulation model. *Planet. Space Sci.*, **47**, pp. 493–520.
- Tomasko, M. G., B. Archinal, T. Becker, B. Bézard, M. Bushroee, M. Combes, D. Cook, A. Coustenis, C. de Bergh, L. E. Dafoe, L. Doose, S. Douté, A. Eibl, S. Engel, F. Gliem, B. Grieger, K. Holso, E. Howington-Kraus, E. Karkoschka, H. U. Keller, R. Kirk, R. Kramm, M. Küppers, P. Lanagan, E. Lellouch, M. Lemmon, J. Lunine, E. McFarlane, J. Moores, G. M. Prout, B. Rizk, M. Rosiek, P. Rueffer, S. E. Schröder, B. Schmitt, C. See, P. Smith, L. Soderblom, N. Thomas, and R. West (2005). Rain, winds and haze during the Huygens probe's descent to Titan's surface. *Nature*, **438**, pp. 765–778. doi:10.1038/nature04126.
- Tomasko, M. G., B. Bézard, L. Doose, S. Engel, and E. Karkoschka (2008a). Measurements of methane absorption by the descent imager/spectral radiometer (DISR) during its descent through Titan's atmosphere. *Planet. Space Sci.*, **56**, pp. 624–647. doi:10.1016/j.pss.2007.10.009.
- Tomasko, M. G., B. Bézard, L. Doose, S. Engel, E. Karkoschka, and S. Vinatier (2008b). Heat balance in Titan's atmosphere. *Planet. Space Sci.*, **56**, pp. 648–659. doi:10.1016/j.pss.2007.10.012.
- Tomasko, M. G., D. Buchhauser, M. Bushroee, L. E. Dafoe, L. R. Doose, A. Eibl, C. Fellows, E. M. Farlane, G. M. Prout, M. J. Pringle, B. Rizk, C. See, P. H. Smith, and K. Tsetsenekos (2002). The Descent Imager/Spectral Radiometer (DISR) Experiment on the Huygens Entry Probe of Titan. *Space Science Reviews*, **104**, pp. 469–551. doi:10.1023/A:1023632422098.
- Tomasko, M. G., L. Doose, S. Engel, L. E. Dafoe, R. West, M. Lemmon, E. Karkoschka, and C. See (2008c). A model of Titan's aerosols based on measurements made inside the atmosphere. *Planet. Space Sci.*, **56**, pp. 669–707. doi:10.1016/j.pss.2007.11.019.

- Tomasko, M. G. and P. H. Smith (1982). Photometry and polarimetry of Titan - Pioneer 11 observations and their implications for aerosol properties. *Icarus*, **51**, pp. 65–95. doi:10.1016/0019-1035(82)90030-6.
- Trafton, L. (1975). The morphology of Titan's methane bands. I - Comparison with a reflecting layer model. *ApJ*, **195**, pp. 805–814. doi:10.1086/153385.
- West, R. A., M. E. Brown, S. V. Salinas, A. H. Bouchez, and H. G. Roe (2005). No oceans on Titan from the absence of a near-infrared specular reflection. *Nature*, **436**, pp. 670–672. doi:10.1038/nature03824.
- Yelle, R. V., D. F. Strobell, E. Lellouch, and D. Gautier (1997). The Yelle Titan Atmosphere Engineering Models. In Wilson, A. (ed.) *Huygens: Science, Payload and Mission*, volume 1177 of *ESA Special Publication*, pp. 243–+.
- Yung, Y. L., M. Allen, and J. P. Pinto (1984). Photochemistry of the atmosphere of Titan - Comparison between model and observations. *ApJS*, **55**, pp. 465–506. doi:10.1086/190963.
- Zarnecki, J. C., M. R. Leese, B. Hathi, A. J. Ball, A. Hagermann, M. C. Towner, R. D. Lorenz, J. A. M. McDonnell, S. F. Green, M. R. Patel, T. J. Ringrose, P. D. Rosenberg, K. R. Atkinson, M. D. Paton, M. Banaszekiewicz, B. C. Clark, F. Ferri, M. Fulchignoni, N. A. L. Ghafoor, G. Kargl, H. Svedhem, J. Delderfield, M. Grande, D. J. Parker, P. G. Challenor, and J. E. Geake (2005). A soft solid surface on Titan as revealed by the Huygens Surface Science Package. *Nature*, **438**, pp. 792–795. doi:10.1038/nature04211.